DIFFUSION CONSTRICTION OF IONS USING VARYING FIELDS FOR ENHANCED SEPARATION, TRANSMISSION AND SIZE RANGE IN ION MOBILITY SYSTEMS

by
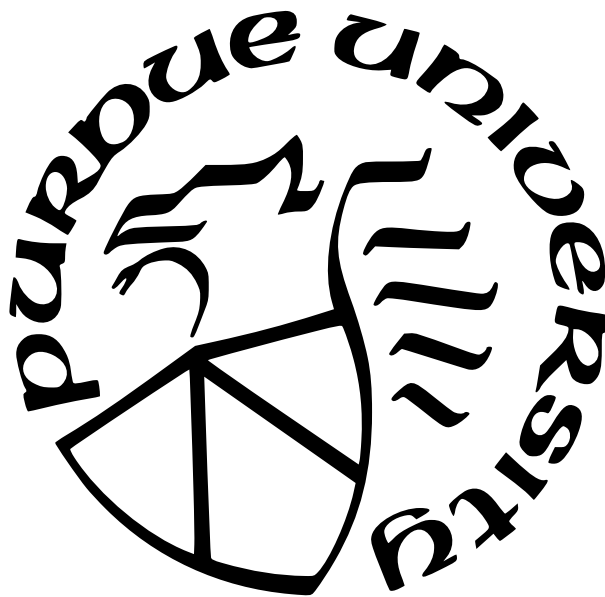
Xi Chen

A Dissertation

Submitted to the Faculty of Purdue University

In Partial Fulfillment of the Requirements for the degree of

Doctor of Philosophy

School of Mechanical Engineering

West Lafayette, Indiana

May 2022

THE PURDUE UNIVERSITY GRADUATE SCHOOL
STATEMENT OF COMMITTEE APPROVAL

Dr. Carlos Larriba-Andaluz, Co-Chair

Department of Mechanical and Energy Engineering

Dr. Liang Pan, Co-Chair

School of Mechanical Engineering

Dr. Julia Laskin

Department of Chemistry

Dr. Andres Tovar

Department of Mechanical and Energy Engineering

Approved by:

Dr. Nicole L. Key

This paper is dedicated to my academic advisor, Professor Carlos Larriba-Andaluz. He brought me into the academia and help me to be a qualified PhD.

ACKNOWLEDGMENTS

First, I would like to express my sincere gratitude to Prof. Carlos Larriba-Andaluz, my advisor in the research area and a life mentor. Not only supported me during my Ph.D. program academically and financially, he helped me to develop a strong character, gave me the courage to face difficulties and the ability to solve the problems met in research area, which is the rare treasure in my life. I can not say anything, but thank you, Professor, for the guidance, encouragement, and insight recommendations.

I want to say thank you to my parents, thanks for their understanding, patience, and encouragement for fulfilling my dreams, without their support, I can not complete my PhD degree.

I would like to thank my committee members, Prof. Liang Pan, Prof. Julia Laskin, and Prof. Andres Tovar for taking the time with me to fulfill all the requirements of the doctoral program. Especially Prof. Julia Laskin, she offered me the chance to have a deep understanding of the Ion Funnel system and improved my skills in Solidworks and SIMION software which will be very helpful for my future research.

I want to thank my lab-mates in Prof. Carlos Larriba's group: Mohsen Latif, Viraj Gandhi, Leyan Hua, Minal Nahin, Joseph Derrick, Vaibhav Shrivastav and my friend Rou Chen, they were there for me when I needed it most.

TABLE OF CONTENTS

LIST OF FIGURES

LIST OF SYMBOLS

K Ion mobility

q Charge of the ion

N Gas number density

m The mass of the buffer gases

M The mass of the ion

k_b Boltzmann's constant

T Temperature

Ω Ion's collision cross section

E Electrical field

v_d Drift velocity

L Length of the drift tube

t Time

n Population of ions

V_{drift} Drift Velocity

V_{gas} Gas Velocity

K_0 Reduced Mobility

P Pressure

e   Charge of an electron

ρ_{gas} Density of the drift gas

m_{red} Reduced mass of drift gas

Λ Separation ration

A Slope of the linear electric field

z Position in the axial direction

$\overrightarrow{v}_{zion}$ Ion velocity

$\overrightarrow{E}_z$ Electric field in axial direction

$\overrightarrow{E}_r$ Electric field in radial direction

$\overrightarrow{u}_r$ Unit vector in the radial direction

r Distance in the radial direction

r_0	Radius of the tube
β	Scan rate parameter
E_e	Electric field in the plateau
n_z	Population of ions in axial direction
n_r	Population of ions in radial direction
σ_z	Standard deviation in axial direction
σ_r	Standard deviation in radial direction
v_{max}	Maximum velocity in the parabolic profile
Φ_0	RF potential
w	RF driven frequency
θ_0	RF initial phase
U	DC potential applied
V	AC potential applied
Δz	Distance between two peak centers
R_p	Resolution of two peaks
D_L	Longitudinal diffusion
t_{pulse}	Pulse time
V_0	Initial voltage employed
t_{HVP}	High voltage pulse time
$PA_{s,m}$	Projected Area
ρ_{pol}	Density of the polymer
r_g	Radius of the gas
ξ	Accommodation coefficient

ABBREVIATIONS

DT	Drift Tube
DMA	Differential Mobility Analyzer
IDT	Inverted Drift Tube
VFDT	Varying Field Drift Tube
ESI	Electrospray Ionization
DTIMS	Drift Tube Ion Mobility Spectrometry
MS	Mass Spectrometry
IMS	Ion Mobility Spectrometry
IMMS	Ion Mobility Mass Spectrometry
RF	Radio Frequency
CCS	Collision Cross Section
SNR	Signal to Noise Ration
BNG	Bradbury-Nielson Gate
TG	Tyndall Gate
TWIMS	Travelling-Wave Ion Mobility Spectrometry
DC	Direct Current
API	Atmospheric Pressure Ionization
FAIMS	High Field Asymmetric Waveform Ion Mobility Spectrometer
SLIM	Structure for Lossless Ion Manipulation
PCB	Printed Circuit Boards
HVP-VFDT	High Voltage Pulse - Varying Field Drift Tube
TIMS	Trapped Ion Mobility Spectrometers
OMS	Overtone Mobility Spectrometers
DMS	Differential Mobility Spectrometers
ROMIAC	Radial Opposed Migration of Ion and Aerosol Classifier
FIMS	Fast Integrated Mobility Spectrometers
DDA	Diffusion Differential Analyzer
OSA	Oversampling Selective Accumulation

CFD	Computational Fluid Dynamics
FWHM	Full width at half-maximum
CPC	Condensation Particle Counter
SMPS	Scanning Mobility Particle Size
TBA	Tetrabutylammonium bromide
TPA	Tetrapentylammonium bromide
TXA	Tetrahexylammonium bromide
THA	Tetraheptylammonium bromide
ATD	Arrival Time Distribution
FAPA	Flowing Atmospheric-Pressure Afterglow
FVP-VFDT	High Voltage Pulse - Varying Field Drift Tube
HFP	High Field Pulsing
LF	Linear Field
SDS	Statistical Diffusion Simulation
PEG	Polyethylene-glycol
PCL	Polycapro-lactone
PDMS	Polydimethylsiloxane
MD	Molecular Dynamics
IEM	Ion Evaporation Model
CRM	Charge Residue Model
CEM	Chain Ejection Model
TOF	Time of Flight

ABSTRACT

Drift tubes (DT) are prominent tools used in Ion Mobility Spectrometry (IMS) to separate ions in the gas phase due to their difference in mobility. While prominently used for small ions ($< 10nm$), their use for larger particles (up to 100nm) is limited and can only be attempted at atmospheric pressure due to diffusion. A system that specializes in high sensitivity larger particles (up to 1000nm) is the Differential Mobility Analyzer (DMA), but lacks in resolution (< 10 for particles 30-1000nm). The idea behind this work is to be able to design a new IMS system based on similar principles to the DT but that allows high resolution and sensitivity for a large range of sizes if possible. The primary idea revolves around the principle of non-constant linear fields to try and control the width of the ion packet as it travels through the system. The first attempt was an Inverted Drift Tube (IDT) which lacked sufficient sensitivity. This was followed by the development of the Varying Field Drift Tube (VFDT) which was the first of such systems to perform better than a regular DT, but only marginally. Finally, the last version of the system included a secondary pulse and labeled High Voltage Pulse - Varying Field Drift Tube (HVP-VFDT), which solved some of the issues of the VFDT and was able to achieve resolving powers of 250, 3-5 times higher than regular DT.

In the IDT system, a gas flow is used to drive the packet of ions through the drift region while a linearly increasing electric field which is in the opposite direction of the flow is used to slow down the ions and separate them. In this regime, it is the largest ions that arrive at the detector first, hence the name Inverted Drift Tube. This technique would allow larger ions and particles to be detected. At the same time, the linear field can be shown to have diffusion constriction (auto-correction) properties, where the broad distributions may be narrowed in the axial direction. However, the gas flow is difficult to control well and the parabolic velocity profile of the gas flow in the tube is a unfavorable factor for the system.

To avoid the issue of the parabolic velocity but still take into account the VFDT takes the advantage of the diffusion auto-correction, the gas flow is suppressed and a linearly decreasing field is used to drive the ions. By solving the Nernst-Planck equation, we show that the VFDT has a spatial resolving power that is much higher than that of the regular DT. A DT was built and tested using a mixture of tetraalkylammonium salts. The transformation

from the raw variable arrival time distribution to collision cross section or mobility diameter is derived and the linear relationship makes it simple for calibration and transformation. A resolving power of over 90 is achieved experimentally although higher resolving powers were expected theory.

It turns out that the difference between theory and experiments had to do with the fact that in the VFDT, the spatial and time resolving powers are different.This is due to the low drift velocity at the end of the drift tube. To increase this velocity, a high voltage pulse is applied at a certain time depending on the ions of interest with a new system, HVP-VFDT. The system was tested numerically and experimentally where several parameters where tested resulting in a higher resolving powers when compared with DT and VFDT systems.The simulation results showed that the transmission efficiency and resolving power can be controlled by raising or lowering the field. Overall, the experimental setup tested reached resolving powers of 250 with moderate gate pulses. The HVP-VFDT system also shows that the distribution may be narrowed over the initial one, something impossible with a real drift tube and opens a myriad of possibilities, including resolving powers of several thousands under low pressure and RF fields.

The next step will be to couple the system to a Mass Spectrometer which is expected to be completed in the near future. To understand how a DT works with RF fields and low pressure, a collaboration was done with David Clemmer's lab and his 4 meter drift tube that can achieve resolutions of 150 in Helium at 4torr. Here, we tested a set of polymers and compared the results to those acquired in Nitrogen with a DMA. The shape and structure of the polymers in the gas phase was studied showing self-similar assemblies that corresponds to a globule with an appendix sticking out.

1. INTRODUCTION

1.1 Overview of the dissertation

The dissertation is divided into 7 Chapters. The first Chapter, Introduction, is devoted to a Literature Review of Ion Mobility Spectrometry, the description of a general IMS Drift Tube(DT) system, an overview of existing IMS systems, and the intellectual merit of the research objective, including past work on the subject by former student Minal Nahin [1].

Chapter 2 deals with the initial theoretical and simulation work that is used in Inverted Drift Tubes (IDT) and compares it to existing technology such as the Trapped Ion Mobility Spectrometer(TIMS), which uses similar principles. This is the first time that the solution to the Nernst-Planck equation is solved fully for a 2D axi-symmetric case with a linear field.The diffusion auto-correcting principle is fully described where ion constriction occurs in the axial direction but the distributions are squeezed in the radial direction. To control the radial effects, RF is a possibility but Mathieu's equation needs to be modified due to different stability criterions. There are some issues regarding the use of IDT at atmospheric pressure do to the difficulty of controlling the gas flow correctly. This work was published in Analytical Chemistry [2].

Chapter 3 redirects the focus to the auto-correction technology (patented), by describing a system with a decreasing linear field, and that is termed Varying Field Drift Tube (VFDT). The system's resolving power is obtained theoretically and the system is tested experimentally and compared to a regular drift tube. While the VFDT rigorously outperforms the DT theoretically, it seems that only a modest increase in resolving power is observed experimentally. This chapter was published in Aerosol Science [3].

Chapter 4 focuses on figuring the reason for the "lower than expected" performance of the VFDT. The difference seems to stem from the fact that the theory was predicting the "spatial" resolving power of the VFDT system while, experimentally, the instrument used was only able to provide us with the "temporal" resolving power. While on a regular DT these two resolving powers are the same, they are different in a VFDT due to the low drift velocity at the end of the drift region. One possible way to take advantage of the high resolving power is to create a High Voltage secondary Pulse at an appropriate time to increase the

drift velocity of the ions prior to getting to arriving at the detector. This technique was very succesful, bringing the resolving powers in line with what was expected theoretically. Experiments show that the system resolving power can reach over 250 in resolution using 7kV voltage and 21cm in length, with a modest gate pulse of $390\mu s$. An interesting outcome of this technique is that it is possible to end up with an axial distribution width that is narrower than the initial one, making the system unique and opening the possibility of incredibly high resolving powers at low pressures where RF may be used to contain the ions radially. Meanwhile, the electric field in the radial direction introduced by the pulsing voltage constricts the ions to the center, so as to increase the transmission efficiency. This opens up the new steps to future work regarding coupling these systems to a Mass Spectrometer and using RF. This chapter has been published in Analytical Chemistry [3].

Chapter 5 is a chapter devoted to understanding the difference between low pressure and atmospheric pressure systems as well as getting initial insight into how to work with RF technology in a drift tube system. The work revolves around the study of gas phase polymer structures and how they assemble. It can be shown that regardless of pressure and/or gas, the long polymer chains try to wrap themselves up into globules. This is counteracted by the charges present. An equilibrium structure is reached where there exist a globule with an extended appendix sticking out. The size of the globule vs. the appendix depends on the length of the ion and the number of charges, where the extremes show the absence of either the globule (fully stretched) or the appendix (globular ion). This shows that self-similar families of ions are formed and it is shown using Ion Mobility Spectrometry. This work has been published and the figure of experimental results was selected as the cover of the Journal of the American Society for Mass Spectrometry [4].

Chapter 6 is a summary and conclusions of the results contained in the dissertation and Chapter 7 is the Future Work revolving around the use of the ion constriction technique.

1.2 Literature review of Ion Mobility Spectrometry

Ion Mobility Spectrometry (IMS), formerly regarded as Plasma Chromatography [5], is a prominent technique used for separating and tracing gas-phase analytes. In IMS, the sep-

aration mechanism is based on the particles individual velocity which depends on the mass, charge and collision cross section. Ions are accelerated under the influence of a uniform electric field and hampered by the collisions with the gas molecules which slow the ions. The ions will reach a constant velocity when the drag force is in equilibrium with the electrical force which changes for ions of differing structural properties. This drift velocity is related through the field employed to the transport property known as mobility. After the separation, the analytes are detected and differentiated by their arrival time through a downstream detector [6]. Not only used as a stand-alone analyzer, there's an increasing interest in coupling the IMS with Mass Spectrometry (MS) systems which adds a new dimension of separation. The IMS is widely used as an analytical instrument for detection of a wide range of compounds including illicit drugs, chemical and biological warfare agents and explosives. Besides, IMS features several advantages, such as fast response time on the order of milliseconds or seconds, simplicity, easy to use, and excellent detection limit; which has made it a perfect choice for border customs narcotic and explosives detection and is greatly applied in military for chemical and biological welfare.

The ion mobility was first measured and characterized by Ernest Rutherford at 1899 [7]. In the following three decades, the study interest of ion mobility was increased including the theoretical and experimental study of the effect of pressure, temperature, attractive forces and collisions with the buffer gas [8]. The modern IMS theory was introduced during 1948-1970, and large amount of foundation studies in ion mobility were conducted by Mason & Schamp [9] and McDaniel [10].

1.3 Sections of an Ion mobility spectrometer

In general, the ion mobility spectrometer consists of three basic units including an ionization source, a drift tube and an ion detector. There are several ionization sources that may be coupled with the IMS to produce gas phase analyte ions. These include but are not limited to Electrospray Ionization (ESI), Radioactive sources, Corona Discharge, Desorption Electrospray Ionization (DESI) and Matrix Assisted Laser Desorption Ionization (MALDI); some of which are described below. Once the analyte of is ionized, ions are accelerated gen-

erally using an electric field and are separated according to their different mobility. When the ions reach to the detector their current is measured. Given that the current is very low, it is amplified by an amplifier, which ranges from a current amplifier to a Microchannel Plate Detector (MCP) if connected to a Mass Spectrometer. Given that this dissertation is mostly concerned about improving a particular IMS system, the Drift Tube (DT), the description will focus on such systems while other IMS devices will be briefly explained.

1.3.1 Ionization source

Ionization methods are utilized to convert the neutral sample molecules into ions and guide them through an interface into the IMS or MS systems. There are three very commonly used ionization sources coupled with DT of interest here: Electrospray Ionization [11], Radioactive Sources Ionization [12] and Corona Discharge Ionization [13], [14].

Electrospray Ionization

Electrospray ionization (ESI) is widely used in IMS instrumentation. In ESI, a pressure system (pressurized gas or step needle motors) is used to push a liquid sample that contains the analyte dissolved to the tip of a capillary where a meniscus is formed. The solution normally contains a buffer charge (either the analyte itself (as a salt) or a free charge (Hydrogen, Sodium), and hence a high electric potential may be applied to drive the charges from the liquid phase meniscus into the gas phase. The surface tension of the solvent reacts against this and an equilibrium structure, referred to as a Taylor Cone is created at the capillary tip. The end of the Taylor Cone is usually followed by a small jet (cone-jet formation) which eventually breaks up by either varicose instabilities or by Rayleigh-limited criterions. This jet creates small charged droplets that contain the analyte of interest. The solve in these droplets evaporate leaving only the sample molecules to be analyzed. is applied to the sample liquid through a needle, creating electric charges in the solution. As showed in Figure 1.1, when the coulomb repulsive force in the droplets is greater than the surface tension force, the droplet explodes into a series of smaller size droplets, ideally in single molecular ions [15].
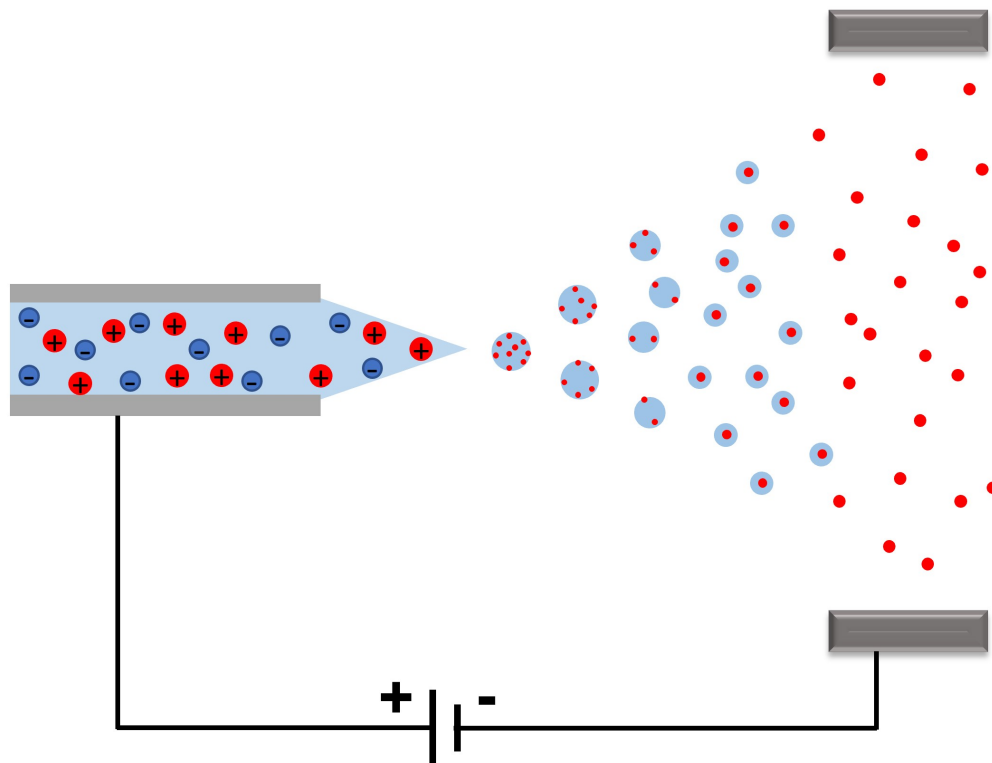
Figure 1.1. A schematic illustration of Electrospray Ionization method. A high electric potential is employed between the sample liquid and the electrode ring, creating a stable Taylor Cone. When the columbic force is greater than surface tension, the electrospray happens.

Electrospray is a soft ionization method where the intention is to avoid fragmentation of the ion in the process, which makes it possible to study the original structures of the molecules. This technique granted John Bennett Fenn the Nobel Prize in Chemistry in 2002 (shared with Koichi Tanaka that proposed the Soft Laser Desorption (SLD) which is the basis of the MALDI technique). The advantages of the ESI are: 1. It offers a simple way to ionize non-volatile solutions and applicable for almost any polar sample if it is soluble; 2. make it possible to analyze large size molecules (on the order of kDa or mDa) with multiple charges; 3. effectively combined with other MS systems for complex solutions. Because of these characteristics, the ESI-MS has been widely used to test explosives [16], chemical warfare detection [17], and biological mixtures [18]. At the same time, there are some disadvantages for ESI technology, for example, external high voltage power supply is required.

Radioactive sources

^{63}Ni is commonly used as a radioactive source for ionization [19], which emits electrons with an average energy of $19keV$, but other radioactive sources such as ^{85}Kr or ^{210}Po are also used. The radioactive sources are usually placed in the ionization region of a drift tube, where the electrons collide with the sample particles and ionize them through charge transfer reactions. Only charged sample particles of the chosen polarity are transported into the drift region through the electric field, the neutral particles and other polarity are removed out of the tube by the counter flow and the walls. It can be used to charge non - polar substances such as Polyaromatic Hydrocarbons (PAH) which is normally very complicated to do with ESI. The advantage of the radioactive sources is the stability, no need of external power supplier and easy maintenance, while the main disadvantage is the safety issue. Radioactive sources create singly charged particles almost exclusively, although a very small portion may become doubly charged, making it a technique that does not allow large ions like proteins to be observed by MS due to their large Thomsons value (molecular weight over charge). They are however commonly employed for aerosol particle DMAs that can detect particles up to $1\mu m$.

Corona discharge

In a corona ionization, an external high voltage is applied between a solid sharpened needle tip and a plate, which generates a high electric field and ionizes the surrounding buffer gas particles, as showed in Figure 1.2. The neutral sample particles flow in a perpendicular direction to the needle and react with these charged gas particles to get ionized. The ion current obtained from the corona discharge is about one order of magnitude higher than that of the ^{63}Ni source charge, which increases the sensitivity of the system and results in a higher signal to noise ratio (SNR). The Corona discharge can be used to increase or reduce the charge of a system (similar to radioactive sources) and can be used to charge non-polar substances. The advantage of the corona discharge is that it is simple to build, operate and maintain with a high signal intensity as well. While the main disadvantage is that an external high voltage power supplier is required. It is once again not used extensively in MS for biological samples due to the low charge of a single ion.
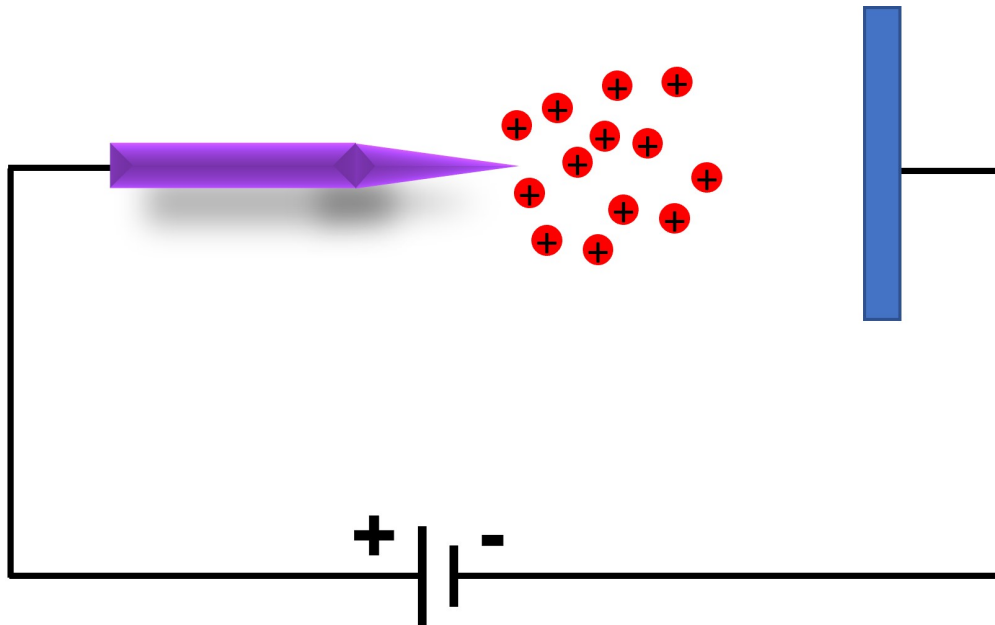
Figure 1.2. A schematic illustration of Corona discharge method. A high voltage is applied between a needle tip and a plate, generating a high electric field and ionize the surrounding buffer gas particles. The sample particles collide with the charged gas particles to be ionized.

1.3.2 Drift tube (DT)

Arguably, the most used IMS system is the DT. The main portion of the DT consists of a series of stainless-steel electrodes that are separated by insulator rings. The electrodes are connected to each other through a series of resistors (magnitude on the order of $M\Omega$), and a high voltage is applied on the first electrode to produce a near-constant electric field inside the tube. The voltage can be tuned based on the size of the ions to be separated and the required resolution to separate them. Typically, high electric fields are commonly employed $(300 - 700V/cm)$.

The drift tube is usually divided into two parts: an ionization region and a drift region, with an ion gate used to separate these two regions, as showed in Figure 1.3. The sample particles are introduced into the ionization region first, where the ionization source mentioned above is commonly placed to ionize the sample particles. The electric field in this region is used to guide the ions to the drift regions while neutral particles or oppositely charged particles will be lost. The gate is used to stop the ions from entering the drift region. At some
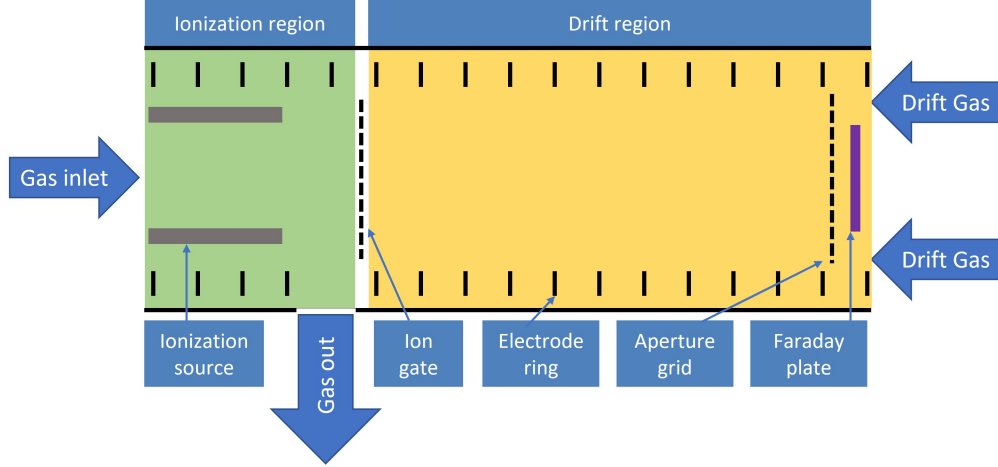
Figure 1.3. A sketch of drift tube, which consist of an ionization region, a drift region and an ion gate.

point the gate is opened and only a controlled packet of ions is let into the drift region. Once inside, the ions get separated depending on their individual mobilities. The drift region is the core component of an IMS instrument, an intermediate region such as an electrodynamics ion funnel [20] is used between the ionization region and the drift region to focus the ions, in particular at low pressure although high pressure focusing has also been attempted.

Regarding the gate, there are mainly two kinds of ion gate system used in the IMS, the Bradbury-Nielsen Gate (BNG) [21] and the Tyndall Gate (TG) [22]. The BNG gate is comb type gate where opposite voltages are applied to consecutive wires when the ions need to be deflected, while the voltages become the same when ions need to be let through. The Tyndall (or Tyndall-Powell) uses two identical wire grids (sometimes three) where one of gates has a high voltage when the ions need to be stopped and a lower voltage when the ions are allowed to go through. The ion gate usually opens $30 - 300\mu s$ per time period to trigger the entrance of a controlled ion swarm into the drift region.

1.3.3 Ion Detector

The most common detector for the standalone IMS system is an operational amplifier inside a Faraday cage. It consist of a Faraday plate and an aperture grid which is placed just a short distance in front of the plate. The function of the aperture grid is to shield the

detector from the inductive effects caused by the ion clusters [23] and gate triggers. The Faraday plate is connected with a current to voltage amplifier, so when the ions impact on the plate, the charge from the ion swarm will be converted to voltage and the intensity amplified. As a result, a series peaks as a function of arriving time will be plotted on the screen, each peak corresponding to an individual mobility of an ion. The problem with the OPA is that in order to increase signal intensity electronically, the noise signal is also increased so a limit in the amplification signal as well as a Limit of Detection (LoD) are always present in the system and cannot be avoided. The area of the arriving peaks can be related to the concentration of the component, and the arrival time could be converted into the corresponding ion mobility diameter or collision cross section (CCS) Ω [24], [25].

1.4 Most Notable IMS Instrumentation and their working principles

1.4.1 Drift Tube Ion Mobility Spectrometer (DTIMS)

Drift tube ion mobility Spectrometer (DTIMS) [26], [27] is one of the most traditional IMS instruments. In DTIMS, the charged particles were driven through a homogeneous electric field in the presence of neutral gas molecules. Figure 1.4 shows the experimental setup of the DTIMS, where a series of stacked-ring electrodes were separated by insulators. The electrodes are connected through constant resistors and a voltage is applied on the first electrode creating a uniform electric field along the axial direction of the tube. The samples (in the gas phase) are transported into the ionization region through a carrier gas while a counter flow is applied to remove the neutral particles out of the drift region. Only ionized constituents have access to the drift region, which is separated from the ionization region through an ion gate. The open time interval of the gate ranges from 30 to 300 microsecond, permitting a packet of ions into the drift region. In this region, the ions are accelerated by the electric field while slowed by the collisions with the drift gas. When these two forces reach to an equilibrium, the ions move at a constant velocity, called drift velocity V_{drift}, which is proportional to the electric field through a transport property known as mobility:

$$V_{drift} = KE \tag{1.1}$$

28

Here K represents the ion mobility of the particles and E represents electric field. To make it easy to describe the mobility of the ions, the reduced mobility K_0 is commonly used to represent the mobility of an ion, which is measured at standard temperature $273K$ and standard pressure $760mm(Hg)$. The mobility at a given temperature and pressure is:

$$K = K_0(P/760)(273.15/T) \tag{1.2}$$

The mobility of an ion is related to many other factors, like the size, shape, mass, charge, etc. In the free molecular regime, it could be defined as Mason-Scamp equation:

$$K = 3q\mathrm{e}/(4\rho_{gas}\Omega)\sqrt{\pi m_{red}/8\kappa T} \tag{1.3}$$

Here, m_{red} is the reduced mass of drift gas, κ is the Boltzmann constant, T is the temperature in kelvin, q is the charge of the ion, ρ_{gas} is the mass density of the gas, and Ω is the collision cross section (CCS) of the ion.

(a)　　　　　　　　　　　　　　　　　(b)
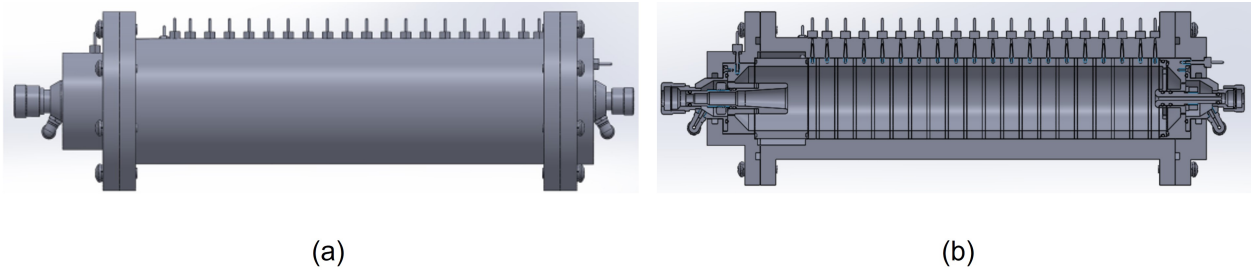
Figure 1.4. (a)Drift Tube Ion Mobility Spectrometer. (b)Section view of the Drift Tube.

Not only used as a stand-alone instrument, DTIMS has also been applied to multidimensional IMS instruments. David Clemmer's group has developed IMS^2-MS and IMS^3-MS approach [28], [29], where up to 3 drift tubes, connected by Ion Activation gates. This leads to the possibility of fragmenting the ions and checking the mobility of such fragments. Each of the drift tube is 90 cm long, and an ion funnel is also placed in between each segment to radially focus the ions and transmit them into the next drift region. Further IMS^n devices, such as IMS^5 has applied circular geometry for the drift tube to reduce the size of the instrument [29].

1.4.2 Travelling-Wave Ion Mobility Spectrometry (TWIMS)

Traveling-Wave IMS (TWIMS) [30]–[32] has a configuration that is similar to DTIMS, but they have quite different working principles. TWIMS always works in a low pressure environment, where a square potential wave propagates through the system, propelling the ions to the detector. A pulsed DC voltage is applied here to adjacent electrode rings, and after a fixed time, the voltage is stepped to the next pair of electrodes, creating a travelling wave with a constant velocity to push the ions in the axial direction. The electric field as a result is more of a sinusoidal wave and the propagation of the ions occurs in a ocean wave like pattern. Simultaneously to this DC potential, a radio frequency (RF) voltage is superimposed to constrain the ions to the center of the tube, which results in high transmission efficiency. By adjusting the voltage of the electrodes and the speed of the traveling wave, the ions are separated based on their individual mobility. Similar as the DTIMS, high mobility ions move faster than their low mobility counterparts. The T-Wave patterns are now ubiquitously used in systems with drift lengths in the order of meters or even kilometers due to the ability to constrain the ions in the system. This leads to very high resolving power systems.
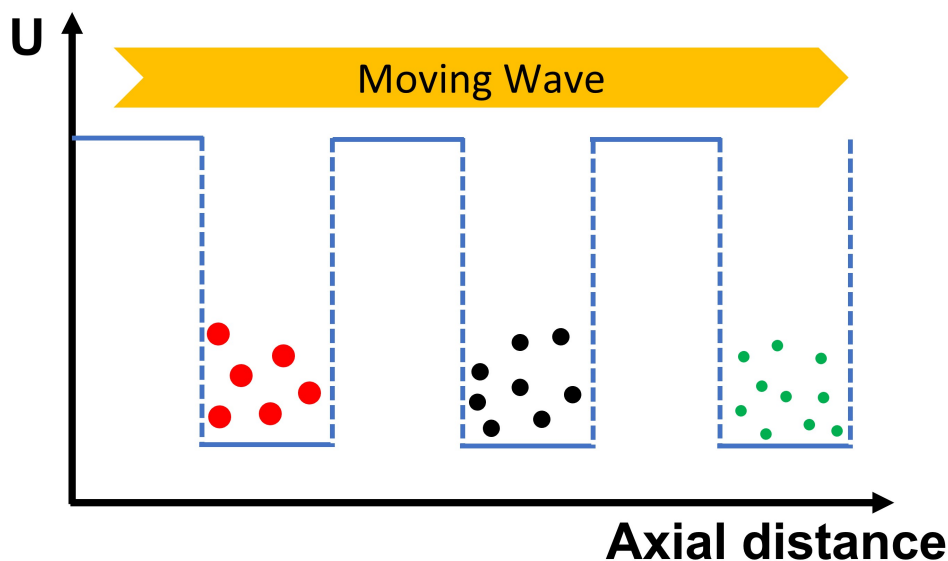
Figure 1.5. Voltage applied in the Traveling-Wave Ion Mobility Spectrometer.

1.4.3 Differential Mobility Analyzer (DMA)

Differential Mobility Analyser (DMA) [33] is another type of IMS instrument that is ubiquitous in the field of aerosol particles but it is rarely used for analytical chemistry purposes. A DMA consists of a sheathed gas laminar flow between two electrodes that have a difference in potential. One of the electrodes has an inlet slit where the ions enter the sheathed region while the other electrode has an exit slit that is a given distance downstream from the inlet slit. The ions that penetrate are pushed by flow downstream and are pushed by the voltage difference to the exit slit. The ions create fan-like shape trajectories depending on their ion mobility so that only a small differential of the fan (a small range of mobilities) makes it to the exit hole and thus to the detector. This is the reason for the use of the differential term as only a small range of mobilities will continue while all other mobilities are lost. One can change the potential difference to allow a different set of mobilities to reach the detector. In fact the system is normally ramped from a low voltage to a high voltage to get all mobilities. The biggest advantage of the DMAs is that they are capable of detecting singly charged particles up to one micron in size. They also have very high transmission but suffer in general from low resolution except for particular systems.

There are three main types of DMA instruments: Radial DMAs, Cylindrical DMAs[33] and Planar DMAs [34], [35]. The former ones, radial and cylindrical are well used for the detection and analysis of sub-micrometer aerosol particles, while the latter are usually applied to couple the an atmospheric pressure DMA with mass spectrometry through an atmospheric pressure interface (API) [34]. The depiction of a planar DMA is shown in Figure 1.6. In a parallel plate DMA such as this one, it is easy to see that for the ion with the mobility that reaches the detector, the time that the ion takes to cross the distance δ between the two parallel plates (δ/ZE) must be the same than the convective flow time that it takes to cover the horizontal distance L between the two plates with a gas velocity U (L/U). Hence the mobility may be calculated from:

$$\frac{\delta}{ZE} = \frac{L}{U}$$
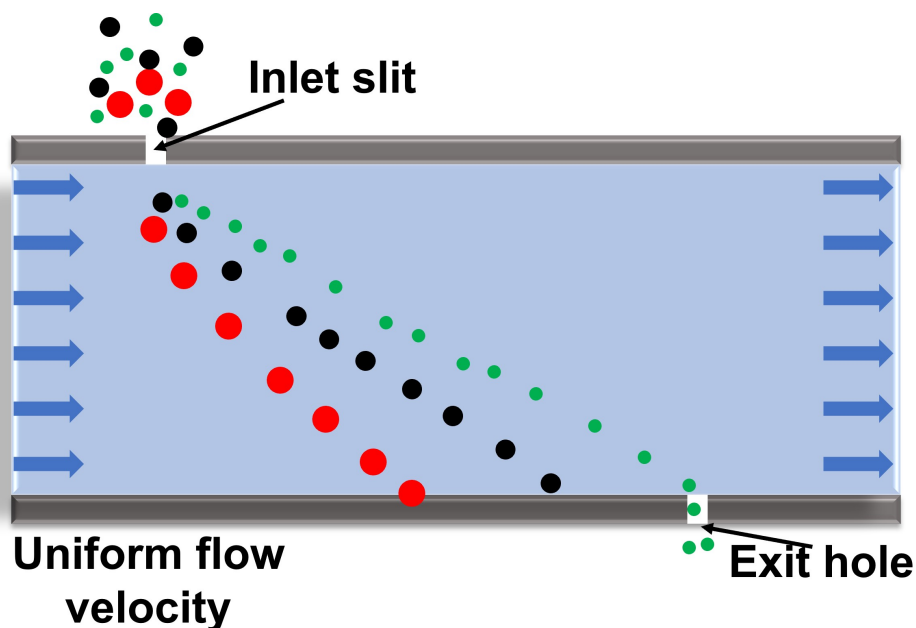
Figure 1.6. Depiction of a planar Differential Mobility Analyzer. The ions, together with the carrier gas, enter into the DMA through a slit inlet fixed on one of the electrode, while an outlet slit on the other electrode. A sheath flow is applied between the two parallel electrodes, which is perpendicular to the direction of the electric field. The ions move under the influence of the combination of the electrical force and the gas flow, and only a given mobility can pass the outlet slit at a time. So the ions travel through different paths inside the DMA and get separated spatially.

1.4.4 Field Asymmetric Waveform Ion Mobility Spectrometer (FAIMS)

Also known a Differential Mobility Spectrometer (DMS, not to be confused with DMA), FAIMS system is one of the few sysetms that directly employ high asymmetric fields to separate the ions [36], [37]. The field can reach over $7500V/cm$ with field over concentration ratios of 30-300 Townsends (Td) which is used to separate the ions in a differential fashion.

Figure 1.7a shows the electric field as function of time and Figure 1.7b shows the ions trajectory inside the FAIMS. A flow between two plates pushes the ions axially. Meanwhile, the asymmetric waveform produces alternating high and low electric field, the high field is applied for one unit of time, followed by an opposite polarity low field component applied by twice that time unit, generally known as the compensation voltage. Given that ions have different response to high and low mobility, most of the ions tend to deviate from the center
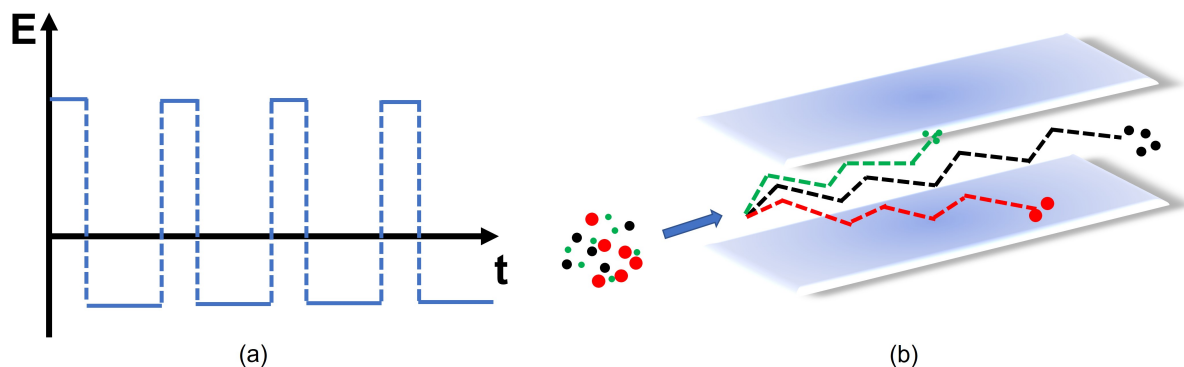
Figure 1.7. (a)Electric field in a FAIMS system, a high electric field is applied for one time unit, followed by an opposite polarity of low field with double time unit. (b)Ion trajectories in the FAIM, only selected mobility can travel through and all the rest got lost eventually on the electrodes.

to one of the plates and get lost. Only a certain mobility is able to make it through the system and into the detector, making the system differential in nature. As such DMS and FAIMS devices work as a filter and only ions of interest can pass through, thus particular ions in the mixture can be uniquely and continuously selected with a proper compensation voltage generating a clear spectrum. The carrier gas can be seeded with different vapors that can momentarily attach to the ions and create a higher separation and can be used with mixtures of gases to enhance the separation. A secondary advantage is that FAIMS can be used to detect positive and negative ions simultaneously [38], [39]. The use of combined high and low electric field as well as the use of vapors makes it so that it is difficult to predict the mobility of the ions that make it through.

1.4.5 Structures for Lossless Ion Manipulation (SLIM)

The Structures for Lossless Ion Manipulations (SLIM) is the most recent IMS system. It has important advantages of high resolution, lossless ion mobility separation, and flexible, low-cost manufacturing. It can be used to separate all sorts of isomers with very minor differences in structures even when complex samples are present. The lossless effects can be also used to quantify the concentration of the analytes, thus achieving extremely high resolution and sensitivity.
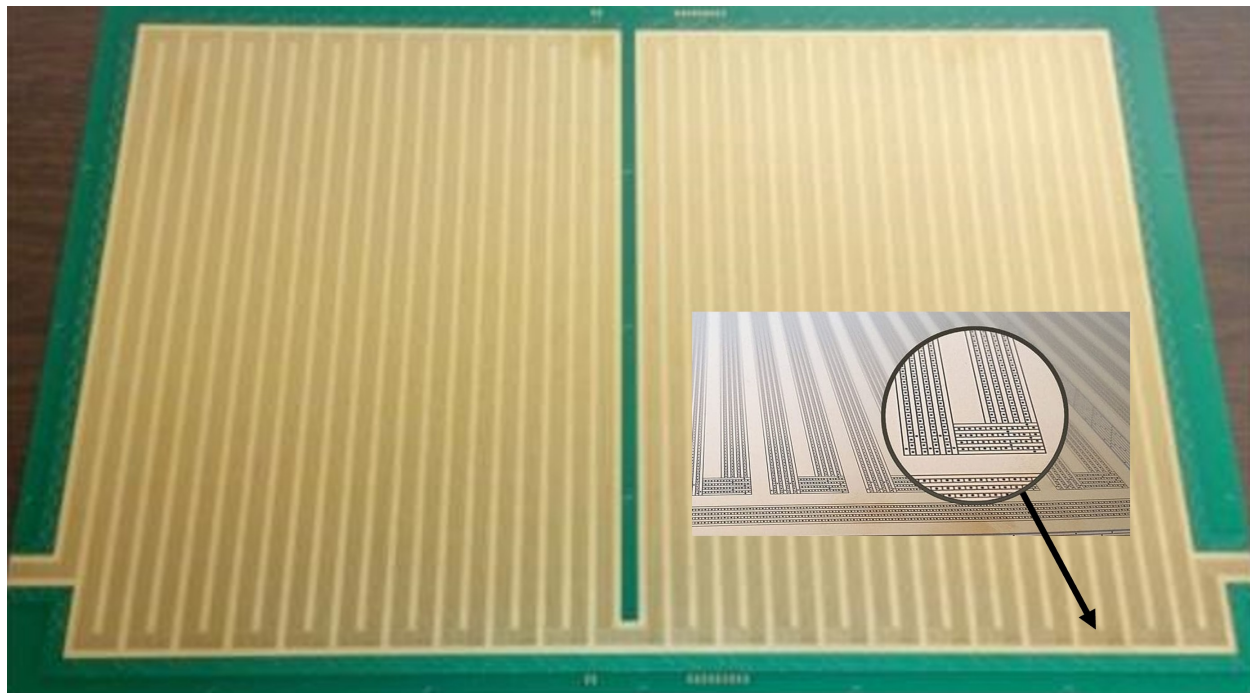
Figure 1.8. Structures for Lossless Ion Manipulation (SLIM), the electrode arrays have been printed on two parallel mirror-image printed circuit boards.

Figure 1.8 depicts one of the printed circuit boards (PCB) that make up for the ion path. SLIM systems have channel like electrode arrays on two planar mirror-image conventionally printed circuit boards, the ions are kept in this paths by a combination of RF and DC voltages. A traveling wave voltage is normally applied on the electrode arrays as the electrical force used to separate and rapidly transport the ions in the pathway. The radio frequency potential with opposite polarities on the adjacent electrodes is used to confine the ions in the center and avoid ion loss. The compact design of SLIM permits a very long serpentine-like traveling paths (the length could be $30m$ on a $30 * 30cm$ board [40], [41]) and ions can turn around the corners by controlling the electric field. The long drift path can be modify to provide multiple passes, increasing the overall length to several hundreds of meters provides high ion mobility separations. Based on the robust separation capability, SLIM could even be used to distinguish structurally identical compounds such as isotopomers through the difference in their moment of inertia [42].

1.5   Research Overview and Objectives and Preliminary Results

Most of the IMS instrumentation described above has the same common shortcoming: ion diffusion. It refers to the "random" movement of ions in the gas phase in spite of the presence of the field. This effect will unquestionably result in a lower transmission and resolution. A second issue that pertains to most of these instruments, is the low size range of ions (even multiply charged) that may be detected. It is very rare for these instruments to detect particles larger than 15nm. The only exception to this rule is the DMA. However, the DMA suffers from very low resolving powers at large sizes (once again due to diffusion).

Regarding diffusion, it is normally divided into two parts: radial diffusion and axial diffusion, each with a different visible effect. The radial diffusion effect disperses the ions in the radial direction where ions may get lost to the electrodes, lowering the transmission efficiency and sensitivity of the instrument. A Radial Frequency (RF) [43] technology can be used for low pressure systems to constrict the diffusion in the radial directions, but has only been theoretically attempted for atmospheric pressure systems due of the requirements of higher voltage and frequency. On the other hand, axial diffusion constriction has not been applied consistently in literature.

Based on these problems, the main objective of our work is to develop new technologies to constrain the ion diffusion in the axial direction for an atmospheric pressure IMS system for separation and analysis of not only ions but aerosol particles, with the intention of improving sensitivity, resolving power as well as the range of the IMS system simultaneously if possible.

The working principle that is employed to obtain this results is the use of a varying field which is used throughout the dissertation in different ways to produce the desired effects above. Our hypothesis is therefore that a varying field may be used to constrain the ions (either radially or axially depending on the whether the electric field raises or lowers) most notably to the point where the final packet of ions may be narrower than the initial one. This allows for higher resolving power and sensitivity (since the initial gate time may be increased substantially). At the same time reversing the electric field may be used to allow the largest particles to arrive at the detector first, increasing the size range that can be obtained.

Initial preliminary work on the IDT was performed by the former student Minal Nahin and it serves as a proper introduction to the concept. This work was published in Nature Scientific Reports[1] and is summarized below.

1.5.1 Modeling of an Inverted Drift Tube for Improved Mobility Analysis of Aerosol Particles

This section is only an introduction to the dissertation and may be skipped as it is preliminary work performed by a different student from Dr. Larriba-Andaluz's lab and is taken verbatim from ref. [1].

1.5.2 Introduction to the IDT to overcome existing problems

Charged gas phase nanoparticles can be subject to drift and separation by means of electric fields. The charge divided by the friction coefficient of the nanoparticle under such fields is defined as electrical mobility and its accurate reckoning is key to the determination of particle size distribution functions. In Aerosol Science, and when dealing with globular particles, a particle's electrical mobility is linked to its diameter, d_p, through the well-known equation [44], [45]:

$$Z = \frac{qeC_C(K_n, \lambda, d_p)}{3\pi\mu d_p} \tag{1.4}$$

where qe is the net charge on the particle, μ is the dynamic viscosity and λ is the mean free path. C_c is the Cunningham's correction factor and is a function of the Knudsen number. Most often, mobility based size distribution functions are measured with differential mobility analyzers (DMA) [46] coupled to Condensation Nucleus Counters CNCs [47], and operated in series as a scanning mobility particle sizer (SMPS) [48], [49]. While the SMPS combination has been incredibly successful, there are several shortcomings to its use which could be improved upon employing different techniques. Because the residence time - length divided by sheath velocity- of transmitted particles in a DMA is fixed and independent of particle size, diffusional broadening leads to degradation of instrument resolution for sub 20 nm particles [50], [51]. For particles larger than 20nm, the resolution, defined as $Z/\Delta Z$, is fixed and with values of approximately < 10 for most operating commercial devices. This

results in adequate resolution but sometimes insufficient - a 90nm monodisperse distribution is barely distinguishable from a 100nm one assuming a resolution of 6. Similarly, SMPSs typically require several minutes to complete voltage scans [48], [49], and even in faster scanning instruments, particles of different sizes are sampled at different times. This limits information that can be obtained when aerosols are varying rapidly, such as can occur during sampling with an aircraft. Further, DMAs require the use of high sheath flow rates, and as such, require modest to high flowrate pumps which must remain stable during operation. This, along with the need of a scanning high voltage source, leads to increase costs in DMA operation. For mobility spectrometers at atmospheric pressure that deal with nanoparticles between 1-120 nm, there is therefore the need to 1) increase resolution by correcting diffusion broadening of nanoparticles in the drift cell, 2) increase the maximum fixed resolution or make the resolution directly proportional to particle size (or inverse mobility) and 3) obtain complete unsteady profiles of particles on rapidly varying aerosols. Problems 2 and 3 have been resolved somewhat by the use of Drift Tube Ion Mobility Spectrometers (DT-IMS) [52]. In such systems, particles of all mobilities are sampled as a packet at a specific time and are guided by a constant electric field to the detector providing separation that depends on the length and electric field [53]. Particles are however still affected by diffusion broadening and, for a fixed electric field and length, yield fixed resolutions independent of size. To achieve high resolution (> 100), the instrument length must be on the order of meters or make use of fairly high electric fields [54], [55], precluding its use as a portable instrument to measure 20-100 nm particles. The need to improve the Ion Mobility systems is quite apparent as multiple improvement designs are becoming available in the last years such as the ROMIAC, the UMN DTIMS or the FIMS [56]–[60] at room pressure or the SLIM or Trapped Ion Mobility (TIMS) instruments [61], [62] at low pressures.

Here a new atmospheric pressure instrument is proposed that is based on the DT-IMS, but which uses two varying controllable opposite forces to correct for diffusion broadening while having its resolution be dependent on mobility, and which increases with the size of the particle. The instrument has been termed Inverse Drift Tube (IDT) due to the electric field being opposed to the migration of the nanoparticles. The concept of using opposing forces is not new as was used by John Zeleny [63] in his experiments dating back as far

as 1898. It is also the same principle that is used in the more recent TIMS spectrometer. However, the merit of the TIMS lies in the use of RF to confine the ions at low pressures [64]. This RF confinement is not possible at atmospheric pressures and thus TIMS is not usable at pressures where the IDT is intended. It also precludes its portability. Therefore, other means of collecting the nanoparticles must be employed in the IDT where the ions cannot be trapped. The text is divided into the characterization of the IDT, followed by a theoretical explanation of the system and its resolution, and ending with 1D and 3D simulations of nanoparticles. In particular, 3D simulations are performed using SIMION, where flow and electric fields are fully determined, and where stochastic diffusion simulations are employed to calculate accurate distributions of nanoparticles.

1.5.3 Shortcomings of previous drift instruments

The main concept of the proposed device is to increase the resolution of the existing instruments for a broad range of sizes ($1nm - 120nm$ in diameter) while maintaining sensitivity (comparable to 20cm drift tubes). The ideal non-diffusional transfer function of a DMA is a well-known function of the ratios of the flow rates. In terms of resolution: [65]:

$$R_D MA = \frac{Q_{sh} + Q_{\mathrm{e}}}{Q_a + Q_s} \tag{1.5}$$

where Q_{sh} is the incoming sheath flow rate, Q_{e} is the excess output flow rate, Q_a is the aerosol inlet flow rate and Q_s is the aerosol outlet flow rate. The resolution is rarely higher than 10 -although theoretically it could reach up to 100 for large sheath to aerosol flow ratios- and remains fixed for all mobilities. Although not appearing in eq . (1.5) the DMA resolution is strongly affected by the diffusion broadening effect. The diffusional variance is in inverse proportion to the voltage $\sigma^2_{diff} \propto 4kT/qV$ [66] which will greatly affect higher mobility particles since the voltage needed to filter them through the DMA is smaller yielding lower values of resolution for highly mobile particles. Given that DT-IMS separation occurs in time -by allowing the ions to travel a given length-, its resolution, $x/\Delta x$, is given by [53]:

$$R_{DT-IMS} = \frac{x}{\Delta x} = \frac{t v_{drift}}{(16 D_L t ln2)^{1/2}} = \frac{qEL}{(16kT ln2)^{1/2}}, \tag{1.6}$$

where q is the charge, E is the electric field, L is the tube length, D_L is the longitudinal diffusion coefficient and T is the temperature. As is evident, the resolution increases with the electric field and the length as the 1/2 power. It is also however important to note that the broadening of the peak Δx is always affected by $D_L t$ which increases with time. Many instances can be found in literature that attempt to increase resolution by increasing the length of the drift tube [67]–[69]. This however comes at the cost of sensitivity losses or appearance of artifacts. The DT-IMS has resolutions that are normally close to 100 for 2 meter instruments but they suffer from diffusion broadening and are not mobility dependent. Large electric fields could be used to obtain higher resolutions and smaller instruments is requirement. However, for portable instruments ($\sim 10cm$) and particles of fairly low mobilities ($K > 1e^{-8}m^2/Vs$), the required electric fields (40kV/m) to have resolutions > 100 would yield acquisition times of 250s that most likely would lead to the loss of the nanoparticles prior to reaching a detector.

Accordingly, there is a need to overcome, stop or delay the diffusion broadening effect that affects both DMAs and Drift Tubes while having a resolution that scales with inverse mobility. A plausible idea is to try and mimic the advancing of the ion through a drift tube without the need to cover any length by providing a second force that restricts the advancing of the ions while maintaining mobility separation hence gaining the drift tube advantage of length dependent resolution without the need of long tubes. In the IDT, one can make use of the electric field as an opposing mechanism to the advancement of the ions through the cell. This still allows for separation in time but where the mobility separation is no longer only subject to a direct square root dependence of the length and field.

1.5.4 Methods and Experimental Setup

Concept is shown in Figure 1.9. The instrument consists of a 120mm long tube and 48mm diameter making the system compact when compared to regular Drift Tubes. At room pressure, packages of ions of multiple mobilities, inserted at the entrance of the tube at time t_0 using a pulsed Bradbury-Nielsen gate, are pushed by a gas flowing with a velocity v_{gas} downstream. A series of electrodes are equally spaced inside the drift tube and are
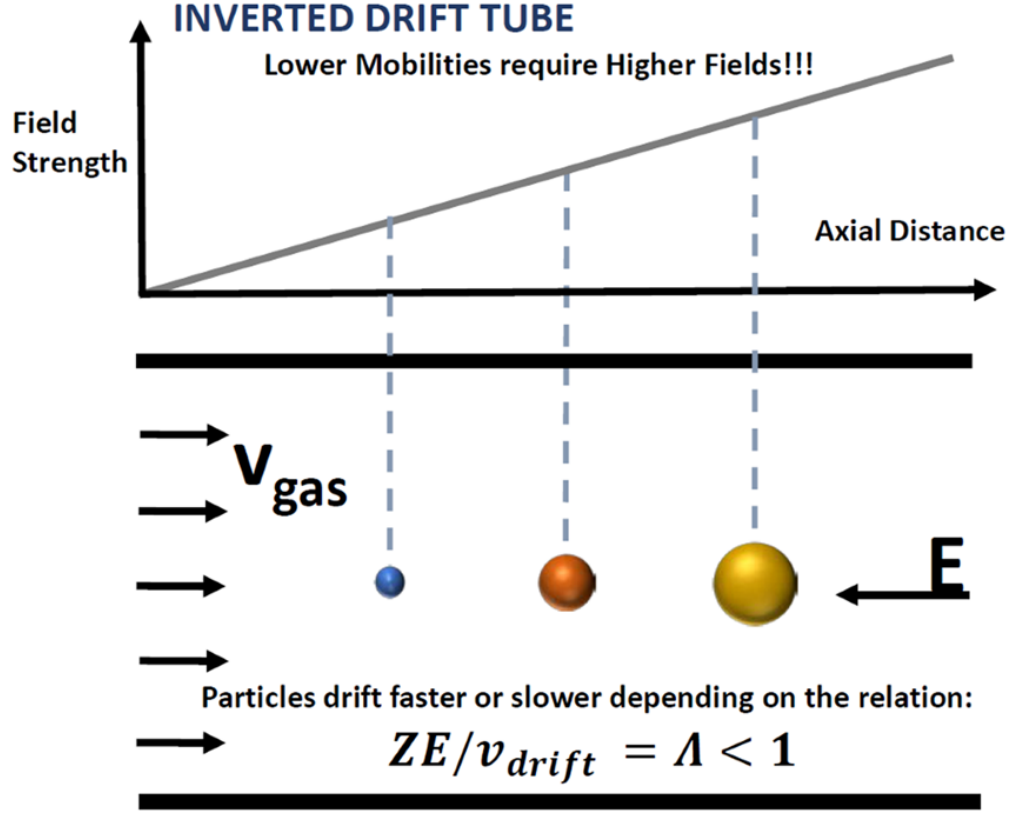
Figure 1.9. Sketch of the Inverted Drift Tube System. Note the gas flow in the direction of the moving ions and the linearly increasing electric field in the opposite direction.

connected through resistors into a power supply. The electrodes are used to create a linearly increasing electric field which opposes the gas flow of the ions slowing their movement relative to $v_{gas}(\sim 0.04m/s$ unless otherwise specified). This allows the ions to be separated depending on their mobility through the drift velocity $v_{drift} = KE$. Given that the field opposes the flow, the lowest mobility ions are the ones ahead in contrast to a regular DT-IMS hence the term "Inverted". As long as the ratio v_{drift}/v_{gas}, termed from here on separation ratio, Λ, is smaller than unity, the ions of a given mobility will traverse through the drift cell without being completely stopped. Eventually, these ions can be collected downstream of the drift tube through a detector. The closer $\Lambda = v_{drift}/v_{gas}$ is to 1, the longer time the ion remains in the drift cell and the higher the separation will be, while it is at the cost of the sensitivity due to the enhanced diffusion in the radial direction. However, if at some point inside the drift cell, the ratio $\Lambda = 1$ is reached, particles of such mobility would be stopped and pushed

towards the walls due to the residual radial electric field that arises from Laplace's equation where $\nabla^2 V = 0$. So, the separation ration, Λ, is a key factor for the separation capability of the instrument and the high mobility (small size) of ions might got lost during the separation the process. Due to the existing room pressure, confining the stopped ions using an RF is quite difficult and will not be pursued.

With a large range of ion sizes, the main idea is therefore to allow all mobilities of interest to traverse the drift cell while trying to keep the ratio Λ as close to 1 as possible without losing the ions. As Λ is mobility dependent, not all mobility ranges being analyzed simultaneously will have high separation ratios. With that in mind, two different mechanisms have been explored to separate ions using the IDT:

1)Intermittent Push Flow(IPF): When trying to separate a wide range of mobilities, a need to vary the opposing electrical field is necessary to acquire all mobilities at high resolutions. The method is depicted in Figure 2a where the highest possible field slope ($dE/dx = A$) for a given electrical supply is initially selected. Before the ion with the highest mobility hits a separation ratio of $\Lambda = 1$, the slope of the electric field is lowered and thus ensuring that $\Lambda = 1$ will never be reached. This drop in the slope can happen as many times as needed until all necessary ions are collected at the end of the drift tube. The resolution and separation of the peaks will depend on the range of mobilities.

2)Nearly-Stopping Potential Separation (NSP): When trying to separate ions of very close mobilities, an alternative possibility is to use an opposing "constant" electric field which is slightly below the necessary field to maintain the separation ratio slightly below 1 for all ions of interest hence maximizing the separation potential. This method is depicted in Figure 1.10.

Whether one mechanism or the other is used will depend on the range of mobilities and the resolution required. The advantage of these type of opposing-field instruments is their autocorrecting properties when used as Intermittent Push Flow separators. In the next section, a derivation of the transport distributions for ions in the IDT with linearly increasing fields is analytically established focusing on its auto-correcting properties and instrument resolution.
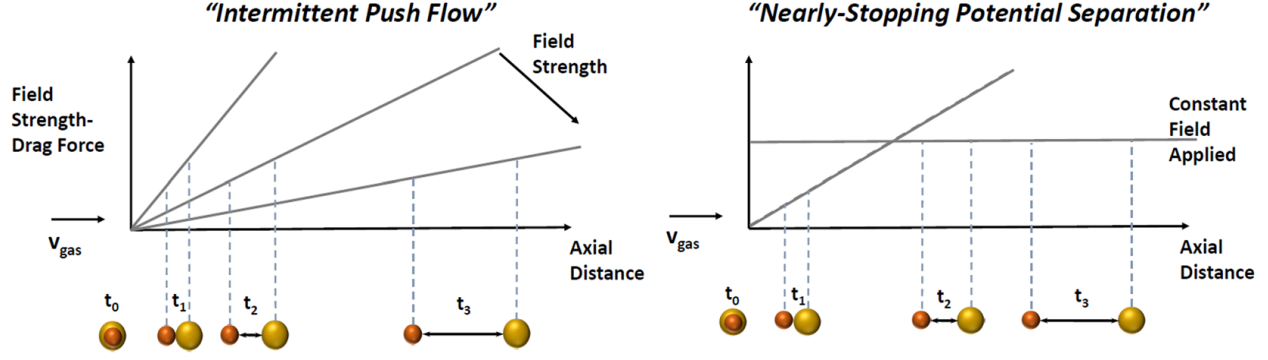
Figure 1.10. A) Intermittent Push Flow. Ions or charged particles are separated by subsequently lowering a linearly increasing field opposite to the flow. B) Nearly-Stopping Potential Separation. An opposite constant field with separation ratio below 1 is used to maximally separate two relatively close mobilities.

While different versions of instruments (such as Trapped Ion Mobility Spectrometers(TIMS),[70]) use electric fields opposite to the flow and have been applied in recent years, the implementation has always been at low pressure and for very high mobilities, which allows the particles to be captured using an RF field when $v_{drift}/v_{gas} = 1$, something that cannot be pursued at room pressure. After $\Lambda = 1$ has been reached in TIMS, the ions are then subsequently pushed by lowering the electric field to the critical value that pushes the particles through. Due to the difficulties of operating RF at room pressure, its implementation and the main principle of trapping the ions used by TIMS has not been pursued in this work.

1.5.5 Theoretical Results of the IDT. One Dimensional Transport of Species in the gas phase migrating through a linearly increasing opoosed electric field. Resolution of an IDT

To simplify the picture, one can assume that the IDT has a fixed increasingly linear electric field to study particles of only one mobility. Let a concentration of $n(r, z, t)$ ions of charge q drift through a tube where a gas flows at a velocity v_{gas} and where a linearly increasing electric field, $\vec{E} = Az\vec{k}$, is applied opposite to the flow (A is the slope of the field).

In a case where the concentration of ions $n(r, z, t)$ is low enough that space charge can be neglected, the balance equation for the species can be given by:

$$\frac{\partial n}{\partial t} - \nabla \bullet (\bar{\bar{D}}_L \bullet \nabla n - (\vec{v}_{gas} - K\vec{E})n) = 0, \tag{1.7}$$

with $\bar{\bar{D}}_L$ being the diffusion tensor and K the electrical mobility. If one considers the one-dimensional problem neglecting radial electric field and diffusion, eq. (1.7) can be written in Cartesian coordinates as:

$$\frac{\partial n}{\partial t} = \bar{\bar{D}}_L \frac{\partial^2 n}{\partial z^2} - (v_{gas} - KAz)\frac{\partial n}{\partial z} + KAn, \tag{1.8}$$

being the initial concentration at time t_0 at the beginning of the tube the surface density:

$$n(0, 0) = n_s \tag{1.9}$$

The Sturm-Liouville solution to the equation for the aforementioned initial concentration can be written as:

$$n(z, t) = \frac{n_s}{\sqrt{2\pi\sigma^2}} e^{-\frac{(z-\bar{x})^2}{2\sigma^2}} \tag{1.10}$$

$$\sigma^2 = \frac{2D_L}{v_{gas}}(\bar{x} - \frac{KA}{2v_{gas}}\bar{x}^2) = \frac{2D_L}{KA}(1 - e^{-2KAt}) = \frac{kT}{qA}(1 - e^{-2KAt}) \tag{1.11}$$

$$\bar{x} = \frac{v_{gas}}{KA} \tag{1.12}$$

There are several features that differentiate this equation from that of the regular drift tube. Most importantly the standard deviation as shown in equation (1.11) has a correction term $KA/(2v_{gas})\bar{x}^2$. This "auto-correction" term is quadratic with the mean position x of the distribution so that it increases with the traversing distance through the drift cell. While the conventional Drift Tube distribution broadens as a function of time, the Inverted Drift Tube distribution broadening is damped and eventually stopped. The contribution of $KA/(2v_{gas})\bar{x}^2$ increases with time (or distance) and, as the ion advances through the drift

43

cell, invariably leads to an asymptotic value of the standard deviation given by kT/qA and independent of t (see eq. 1.11). This asymptotic value will be reached when the separation ratio Λ becomes one. In such instance, the mean position of the distribution will be given by v_{gas}/KA and the ion will no longer advance in the axial direction. The resolution for the IDT can be calculated from eq. (1.10-1.12) as:

$$R = \frac{\bar{x}}{\Delta x} = \frac{\bar{x}}{2\sqrt{2ln(2)\frac{kT}{qA}(1 - e^{-2KAt})}} \tag{1.13}$$

If the drift cell has length L, the resolution at distance L can also be calculated as:

$$R_L = \frac{L}{\sqrt{16ln(2)\frac{KkT}{qv_{gas}}(L - \frac{KA}{2v_{gas}}L^2)}} = \frac{RT_{DT-IMS}}{\sqrt{\Lambda(1 - \frac{\Lambda L}{2z})}} \tag{1.14}$$
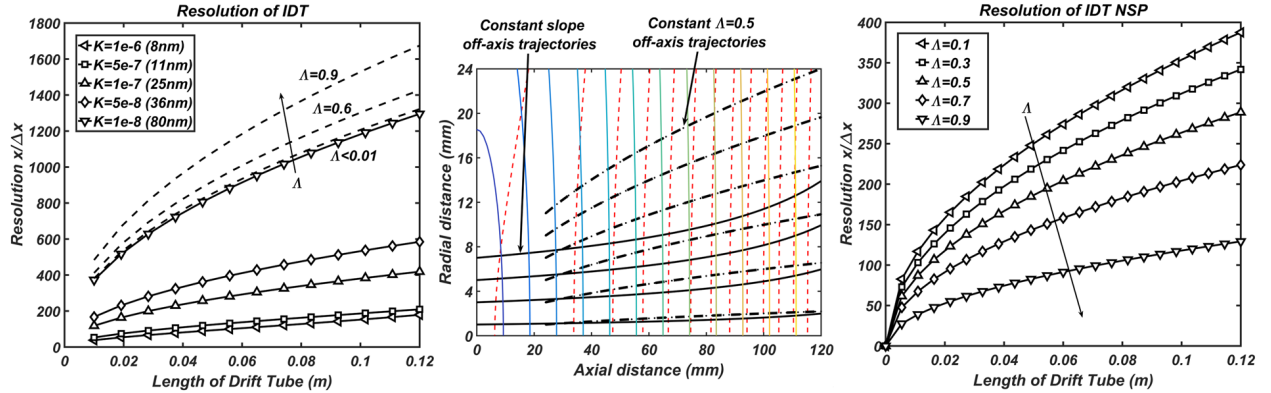
Figure 1.11. A) Mobility dependent IDT Resolution for $v_{gas} = 0.04m/s$ and $A = 3.2e^5V/m^2$ for Intermittent Push Flow(IPF). Dashed lines show theoretical maximum when keeping the separation ratio constant. B) Off axis trajectories due to the existing radial field in Intermittent Push Flow. Perpendicular lines to the axial direction are isofield lines (colormap) and isopotential lines (dashed red) for a constant A. Solid black lines correspond to off axis trajectories at different initial radial conditions using Intermittent Push flow for constant slope A. Dotted black lines correspond to trajectories at a constant separation ratio Λ. C) IDT resolution using the Nearly-Stopping Potential (NSP) method (eq. 1.15).

Figure 1.11 shows the resolution as a function of length and different mobilities for a fixed slope A and v_{gas} (solid lines). Note that unlike the resolution of the Drift Tube depicted in eq. (1.6), the resolution of the IDT has a positive dependence on the mobility. The

resolution of the instrument is very high in terms of eq. (1.14) for very modest lengths, but, given the large difference in mobilities appearing in Figure 1.11a (8-80nm), the separation ratio is very small for the smallest mobilities. In fact, to avoid losing ions of any type, the separation ratio Λ is well below 1 for most of the length of the drift tube (it is only close to one for the 8 nm particles when it reaches 12cm and it is 0.01 for the 80 nm particle at 12 cm). To improve the resolution and separation ratio, one must resort to the tactics used in the previous section, i.e., use of IPF and/or NSP separation. For the intermittent push flow, there is a theoretical optimal resolution for which the separation ratio Λ is kept constant for a particular mobility. This requires continuous change of the field slope A to guarantee that at any given position of the ion Λ *constant*. Figure 1.11b shows the theoretical resolution maximum (dashed lines) for 80 nm particles as a function of the different constant values of the separation ratio. The third expression in eq. (1.14) is obtained by using eq. (1.6) and the definition of the separation ratio. Resolution as given in eq. (1.14) is not particularly useful for this type of instrument as opposed to the DMA or DT-IMS. The reason is that if the field slope was $A = 0$, i.e. no electric field, the residence time in the drift tube will be minimal and there will be no separation between any mobilities. However, the resolution would depend on the competition between diffusion and v_{gas} which could still be very high. The importance of eq. (1.14) relies on the fact that when the separation ratio Λ increases, the residence time inside the system increases, but the resolution also increases in contrast to what is expected with just diffusion.

Since the electric field is solenoidal when space charge is neglected, the radial electric field might be non-negligible off axis and one must wonder about its effect in the trajectories of the ions as the separation ratio is increased. Given $\nabla \bullet \vec{E} = 0$, one can calculate the radial field for constant axial field cross sections $\partial E_z / \partial z = -A$ and which is given by $E_r = Ar/2$. Figure 1.11b shows the trajectories of off-axis particles due to the effects of radial electric fields (no diffusion considered) for two particular cases: a) constant separation ratio $\Lambda = 0.5$ (dashed lines) and b) constant slope $A = 2.5e^5$ and ion mobility $K = 110^{-6} m^2/Vs$ (8nm) (solid lines). For case a) the initial condition is set at $z = 2.4cm$ as the slope A would be too high to maintain a constant separation ratio Λ for smaller values of z. Values that are off axis up to 1.1cm still reach the end of the tube. In case b), the separation ratio Λ increases

with the distance z progressively reducing the velocity of the moving ions ($v_m = v_{gas} - v_{drift}$) until the drift from the radial field becomes of the order of v_m at a given radial position. If this occurs, the ion will inevitably be lost. One must make note that the resolution might be space charge dependent when a high charge concentration is present. However, for small concentrations of large singly charged nanoparticles, this effect is expected to be negligible.

To avoid radial field effects, one can resort to NSP separation mode where the electric field is constant. For such a case, the resolution of a distribution of ions, R_{NSP}, of mobility K after passing through the cell is equivalent to that of a DT-IMS (eq. (1.6)) but where the field opposes movement:

$$R_{NSP}\frac{\bar{x}}{\Delta x} = \sqrt{\frac{qLv_m}{16kTln(2)K}} = \sqrt{\frac{qLv_{gas}(1-\Lambda)}{16kTln(2)K}} \tag{1.15}$$

Note how in this case, the separation ratio opposes resolution. The reasoning is quite clear, the larger the separation ratio, the longer the total residence time in the drift tube and the higher the chance ions have to diffuse before covering a distance L. Figure 1.11c shows the resolution for nearly stopping potentials for a given mobility $K = 110^{-7}m^2/Vs$ (25 nm) as a function of the separation ratio Λ. It is clear from eq. (1.12-1.15) that $R = \bar{x}/\Delta x$ is an ill-conditioned term to define ion separation for the IDT instrument since, as the separation ratio increases, mobility separation in time should be more likely opposite to what the resolution predicts. It is necessary to resort to a different criterion to establish whether ions of different mobilities can be separated and how well. Later on, chromatographic resolving power (R_p) will be introduced to account for mobility separation. While numerical simulations were attempted for the IDT in Chapter 2, no experimental results where obtained that were what theory expected. The reason had to do with the difficulty of controlling the gas flow rate to have a constant velocity at each cross section of the system and not developing into a parabolic profile.

2. ANALYSIS OF ION MOTION AND DIFFUSION CONFINEMENT IN INVERTED DRIFT TUBES AND TRAPPED ION MOBILITY SPECTROMETRY DEVICES

This section is from a published manuscript of the author of this dissertation from ref. [2]. Dr. Carlos Larriba-Andaluz (the corresponding author) has contributed to the theoretical calculation, methodology, validation, writing and editing the manuscript. Author Xi Chen has contributed to the computational fluid dynamics (CFD) simulation and ion trajectory simulation. Author Minal Nahin, Tianyang Wu and Dr. Nobuhiko Fukushima have contributed to the review of the manuscript.

2.1 Overview

Ion mobility spectrometry (IMS) involves a compendium of techniques with the purpose of segregating small charged entities − molecules or nanoparticles − by means of an electrical field in the presence of a buffer gas. IMS relies strongly on the ability of ions to quickly reach an equilibrium drift velocity v_{drift}, akin to a settling or terminal velocity. Moreover, under small ion velocities, the electrical /ion mobility is directly related to the product of the drift velocity and the electric field through a simple equation: $KE \approx v_d$. Ion mobility can then be related to ion size, charge, and gas properties through the use of either the Stokes-Millikan [71], [72] semi-empirical law or the more theoretical Mason−Schamp equation:[53]

$$K = \frac{3}{16}\frac{q}{N}(\frac{1}{m} + \frac{1}{M})^{1/2}\sqrt{\frac{2\pi}{k_bT}}\frac{1}{\Omega} \tag{2.1}$$

Here, N is the gas number density, T the temperature, q the ion's charge, k_b the Boltzmann's constant, m the mass of the gas, M the mass of the ion, and Ω the ion's collision cross section (CCS) [24]. Because of this physically simple and controllable relationship between electrical field and gas, IMS has been gaining momentum in both aerosol science and analytical chemistry fields, becoming one of the most prominent separation techniques. As such, a myriad of IMS systems are emerging. Among such systems, one can name the most conventional ones, drift tube (DTIMS) [73] and differential mobility analyzer (DMA)[46],

which have been available since the 1970s. Recently, many techniques and systems have appeared, including the Transversal Modulated Wave (T-Wave) [74], field asymmetric ion mobility spectrometry (FAIMS) [75], overtone mobility spectrometer (OMS) [69], differential mobility spectrometer (DMS) [76] , Radial Opposed Migration of Ion and Aerosol Classifier (ROMIAC) [77] , fast integrated mobility spectrometer (FIMS) [59], Structure for Loss-less Ion Manipulation (SLIM) [78], diffusion differential analyzer (DDA) [79], Trapped Ion Mobility (TIMS) [80], [81], and Inverted Drift Tube (IDT) [1].

Arguably, one of the most significant problems in IMS systemsis ion diffusion. The "random" movement of ions in the gas phase leads to lower resolution, transmission, and, ultimately, overall sensitivity. As such, it is of particular importance to constrain, regulate, or overcome diffusion to obtain optimal separation results. For the purpose of this study, and given that most IMS instruments have a well-defined axis of revolution, diffusion can be divided into (a) radial diffusion, which is perpendicular to the axis of revolution and causes a lowering of the overall transmission, and (b) axial diffusion, which occurs parallel to the axis of revolution and generally lowers the overall resolution. Radial diffusion has been partially counteracted at low gas pressures through the use of radio frequency (RF) confining voltages [43]. However, the high frequency and voltages required to contain ions at high pressures precludes the use of RF in atmospheric pressure devices. Trying to overcome axial diffusion, some systems resort to increasing the length of the characterization region, e.g., T-wave and DTIMS. It can be shown theoretically that, given the Einstein - Smoluchowski [82] relation under ideal conditions, two ions of different mobilities under a constant field will separate if given sufficient length (or time). The recent accomplishment separating isomers using SLIM systems is noteworthy [83].

However, it is the TIMS and IDT systems that are the main focus of this manuscript for their unique ability to constrain axial diffusion. The two systems have, in common, a separation region where a flow of gas with velocity $\overrightarrow{v}_{gas}$ carries the ion forward while a linearly increasing electric field of the type $\overrightarrow{E}_z = -Az\overrightarrow{k}$ opposes the movement of the ions a technique previously developed by Zeleny [63] in gases and also proven in liquid $-$ phase experiments [84]. Here, A is the slope of the field, z the position in the axial direction, and $\overrightarrow{k}$ the unit vector in that direction. The ion's movement in the axial direction is thus

characterized by the competition between gas and drift velocity so that the ion's velocity is given by $\vec{v}_{zion} = \vec{v}_{gas} - \vec{v}_{drift}$. In the TIMS instrument, ions can be stopped / trapped, $\vec{v}_{zion} = 0$ [85], and are prohibited from colliding with the electrodes through the use of RF fields. The portion of the tube dedicated to stopping the ions is known as the trapping (ramp or rising edge) region. Once trapped, the electric field is lowered, and the ions are " eluted " through a plateau region − constant electric field − and eventually transmitted to a mass spectrometer. While the trapping typically takes tens of ms, the elution happens within $< 1ms$. Therefore, diffusion confinement is the main working principle in TIMS. A schematic of the process is shown in Figure 1. The IDT, in contrast, works at atmospheric pressure and, as such, cannot make use of RF fields to constrain the ions radially. Under these circumstances, the ion must be kept in constant movement, $\vec{v}_{zion} \neq 0$, and a parameter labeled the separation ratio, $\Lambda = v_{drift}/v_{gas} \leq 1$, is used to specify the movement [1]. This parameter plays a key role in the ability of the IDT to resolve different ions.
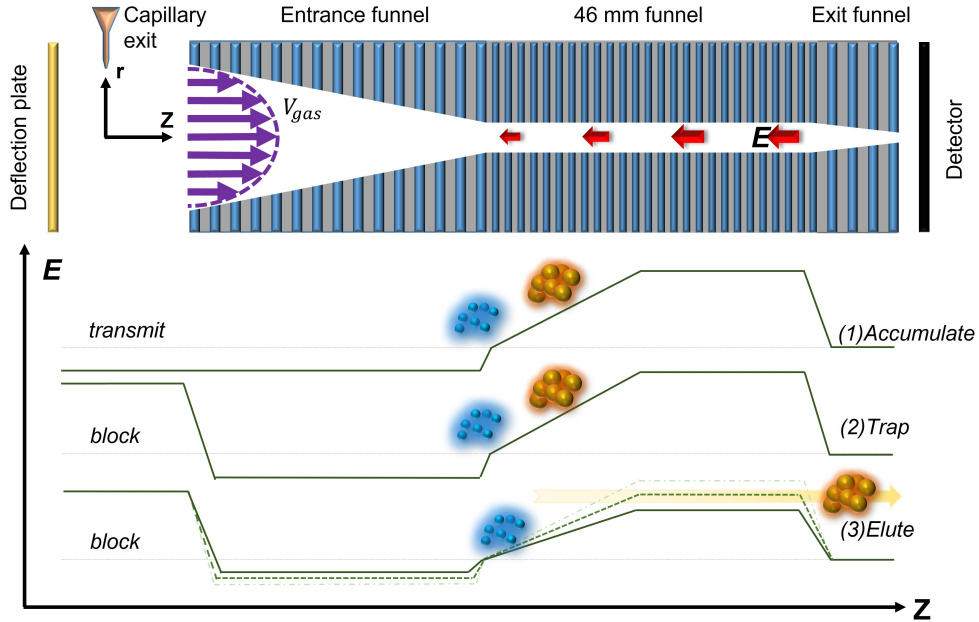
Figure 2.1. Sketch of TIMS setup

In either system, it is the combined effect of both velocities, drift and gas, that controls axial diffusion. However, the complexity of the electro-fluid-dynamic interaction makes its analytical interpretation and understanding quite difficult. Prior to this manuscript, there

has been a few attempts at solving the equations of motion partially. Michelmann, Silveira, and colleagues described ion motion, focusing on the equilibrium position at the end of the ramp, on the elution portion of the plateau, and on the gas flow characterization [64], [85]. They did, in fact, describe a confining electric potential so that "a deviation of the ions from the equilibrium position will therefore result in a net restoring force equal to the ions' charge multiplied by the difference in the electric field strength between the equilibrium position and the deviant position". Many of their results have been meticulously studied experimentally by Fernandez − Lima et al [62], [70], [86]. In particular, they have shown experimentally that the Oversampling Selective Accumulation method (OSA-TIMS) provides higher signal −to − noise ratio [70], [87]. Later on, Bleiholder did a comprehensive study of the trajectory of an ion (or a packet of ions) from a Langevin perspective using nonuniform electric fields in nonstationary gases [88]. The 1D Nernst − Planck balance equation for a distribution of ions of has been previously fully solved by our group showing the diffusion-correction properties of such instruments [1]. Of most significance is the fact that an initial broad distribution can be compressed axially as it travels through the system.

In this manuscript, the analytical solution of the 2D axisymmetrical Nernst − Planck equation is provided for the first time when a linearly increasing electric field opposes a gas flow that carries the ions. The 2D axi − symmetrical solution allows the effect of a residual radial electric field, which is due to the solenoidal aspect of the field, to be considered together with the axial diffusion constraint. The solution is studied for two different flows: constant $\overrightarrow{v}_{gas}$ and fully developed parabolic profile. The effect of the residual electric field has importance consequences for the stability of ions when using RF at low pressures. In fact, it precludes the possibility of using TIMS as an " RF-only " system for all ions. This is studied through a modified Mathieu's equation and its stability region [89]. Finally, effective resolutions of the TIMS instrument are provided. Given the appropriate stability conditions and electric fields, it is expected that mobility differences of $< 0.1\%$ (equivalent resolutions larger than 1000) could be resolved at low pressures with RF and a plateau region in tubes of modest distances.

2.2 Results and Discussion

2.2.1 Analysis of the Ion Motion in Flows Subject to Opposing Linearly Increasing Fields.

There have been multiple studies of the equations of ion motion prior to the study accomplished here. Among different studies, the most prevalent one is that of Moseley's dissertation, also studied by McDaniel [53], which involves the ion motion equation and instrument resolution of a conventional drift tube. Moseley shows that a general solution of the $Nernst - Planck$ equation for constant electric fields and no gas flow can be obtained in terms of a power series expansion. A slightly different approach for nonconstant electric fields will be followed in this manuscript.

Consider a population of ions $n(z, r, t)$ of a single species created at one end of a cylindrically symmetric drift space with gas of a uniform number density N. This population is subject to a constant flow velocity in the positive $z - $ direction $\overrightarrow{v}_{gas}$ while a linearly increasing electric field E opposes the movement.

Assuming that E/N is small, the Nernst Planck equation is given by

$$\frac{\partial n(z, r, t)}{\partial t} - \nabla \cdot (\overline{\overline{D}} \cdot \nabla n(z, r, t) - (\overrightarrow{v}_{gas} - K\overrightarrow{E})n(z, r, t)) = 0 \tag{2.2}$$

$$n(\pm \infty, \pm \infty, t) = 0 \tag{2.3}$$

$$n(z, r, 0) = f(z, r) \tag{2.4}$$

where $f(z, r)$ corresponds to a normal distribution or a point source. Here, $\overline{\overline{D}}$ is the isotropic diffusion tensor. Neglecting the existence of free charge leads to a second equation (equivalent to the Laplace equation for the potential):

$$\nabla \cdot \overrightarrow{E} = \frac{dE_z}{dz} + \frac{1}{r}\frac{drE_r}{dr} = 0 \tag{2.5}$$

51

Provided that the field in the axial direction is given by $\vec{E}_z = -Az\,\vec{k}$, with A constant, the solenoidal aspect of the field (solving eq 2.5) yields the solution to the radial counterpart:

$$\vec{E}_r = \frac{Ar}{2}\,\vec{u}_r \tag{2.6}$$

where $\vec{u}_r$ is a unit vector in the radial direction. Note that this radial component pushes the ions toward the walls. Therefore, it is expected that ions will have a tendency to steer more toward the walls than in regular drift tubes. This will have implications in non-constant-velocity profiles and RF containment, addressed below. TIMS literature uses the scan rate parameter β to describe the change in the slope of the electric field so that ions can be eluted. β can be related to the initial slope of the field A if the length of the ramp region L and the electric field in the plateau, E_e, are known:

$$\beta = \frac{AL - E_e}{t} \tag{2.7}$$

Equations 2.2 - 2.6 form a set of partial differential equations (PDE) for which the analytical solution is desired. It is important to note that, although a 2D axisymmetric solution is sought, an effect of angular diffusion exists. However, as long as the distribution is initially centered, the solution is invariant in the angular coordinate. Assuming no correlation between radial and axial directions, the balance population can be written as

$$n(z, r, t) = n_z(z, t) n_r(r, t) \tag{2.8}$$

Being careful to account for the physical effects, a unique solution can be obtained when the initial condition is either a point source or a radially centered Gaussian distribution:

$$n(z, r, t) = \frac{n_s}{(2\pi)^{3/2}\sqrt{\sigma_z^2 \sigma_r^2}} e^{-(z-\bar{z})^2/2\sigma_z^2} e^{-r^2/2\sigma_r^2} \tag{2.9}$$

with

$$\sigma_z^2 = \frac{2D_L}{v_{gas}}(\overline{z} - c_{z\sigma}\frac{KA}{2v_{gas}}\overrightarrow{z}^2) = \frac{D_L}{KA}(1 - c_{z\sigma}\mathrm{e}^{-2KAt}) = \frac{kT}{qA}(1 - c_{z\sigma}\mathrm{e}^{-2KAt}) \tag{2.10}$$

$$\sigma_r^2 = \frac{2D_r}{KA}(c_{r\sigma}\mathrm{e}^{KAt} - 1) \tag{2.11}$$

and

$$\overline{z} = \frac{v_{gas}}{KA}(1 - c_{zz}\mathrm{e}^{-KAt}) \tag{2.12}$$

Here, n_s is the total ion count and $c_z < 1$, $c_r > 1$, and $c_{zz} < 1$ are constants that are dependent on the initial condition. It can be easily proven that eq 2.9 is the solution to eqs $2.2 - 2.4$; this can be easily proven by inserting the solution into the equation. In Figures 2.2A and 2.2B, numerical solutions of eq 2.8 with random initial conditions are superimposed on the analytical solution, confirming the validity of the solution in radial and axial directions, respectively. In Figure 2.2B, the initial standard deviation in the axial direction is purposefully chosen to be wide. As the distribution evolves, the standard deviation is reduced, proving axial confinement. The full solution for the 2D axisymmetric problem is shown in Figure 2.3A at three different times. Given a point source as an initial condition, the distribution extends more radially than it does axially, creating an oblong shape. Although the radial coordinate is represented here in a $y - axis$, the distribution would evolve in a radial fashion. The solution for several mobility diameters (sphere-equivalent diameter for a given mobility) is shown in Figure 2.3B. The ability to separate ions at a constant slope value A and constant v_{gas} is quite remarkable, even with very large mobility differences, thanks to the diffusion confinement in the axial direction, as explored below.

2.2.2 Axial Diffusion Confinement

It was recently shown that axial diffusion can be regulated using two opposite controlled forces [1]. In fact, an asymptotic value for the standard deviation of a distribution of ions in the axial direction as time goes to infinity can be obtained using eq 2.10 as

$$\sigma^2_{z_{t\to\infty}} = \sigma^2_{z_{asym}} = \frac{D_L}{KA} = \frac{kT}{qA} \tag{2.13}$$

Note that eq 2.13 is fairly identical to that of the asymptotic study of Michelmann et al., confirming the validity of eq 2.9. To reach the asymptotic standard deviation, the mean value of the ion in the axial direction must also reach an asymptotic condition (from eq 2.12), given by

$$\overrightarrow{z}_{t\to\infty} = \overrightarrow{z}_{asym} = \frac{v_{gas}}{KA} \tag{2.14}$$

The asymptotic standard deviation (eq 2.13) is independent of diffusion or mobility, allowing this type of confinement to be used for large and small ions. It is also in inverse proportion to field slope A and the charge q. It can be extrapolated that the only limiting factor to get any desired separation, i.e., effective resolutions on the order of thousands, is the limitation in the maximum slope A that can be applied. A combination of four factors determine the maximum slope: 1) the gas electrical breakdown, 2) the gas flow velocity v_{gas}, 3) the total length of the drift chamber and 4) the mobility / mobilities K one is interested in separating. While the first factor is quite obvious, the other three have to do with the fact that not all mobilities necessarily reach asymptotic conditions for a given set of conditions.

Simultaneously, for any real separation to occur in the experiment, v_{gas} must be large enough so that the distance between the mean values of two particular mobilities $\overline{z}_1$ and $\overline{z}_2$ is greater than the full width at half maximum (fwhm) of either peak. This definition of separation best represents the instrument performance, as opposed to the more widely used resolution (see below). However, it is true that an asymptotic effective resolution can still be obtained from eqs 2.13 and 2.14.

It is important to note that the above asymptotic solution can be reached, regardless of the initial condition. This is a substantial advantage over other systems as unusually broad distributions can be sampled into the system and still be corrected axially if sufficient time is given. This effect, mostly unexplored, could be used to accumulate ions for long periods and subject to lower space charge.

2.2.3   Non-constant Velocity Profiles and Tail Forming

The previous Nernst Planck equation (eqs $2.2 - 2.4$) has been solved assuming that v_{gas} is a constant in the axial direction.

However, this is not accurate. Generally, in a constant section tube, a flow will eventually evolve into a parabolic profile. For a tube with a radius r_0, the flow velocity for a fully developed parabolic profile with maximum velocity v_{max} is

$$v_{gas} = v_{max}(1 - \frac{r^2}{r_0^2}) \tag{2.15}$$

Parabolic profiles have been shown to be accurate for TIMS geometries using computational fluid dynamics (CFD) [85]. Under such circumstances, eq 2.2 becomes coupled and the ion distribution solution becomes convoluted (eq 2.8 is not valid). An approximation to the analytical solution, however, can be explored and compared to a numerical solution, obtained using SIMION 8.1. Figure 2.4A shows the result when packets of ions of up to six different mobilities are stopped inside the tube for a constant slope A, atmospheric pressure, and no RF. The simulation was specifically adapted to represent an ideal situation of a tube with linearly increasing field. Ions start centered, migrate through the tube, and are eventually stopped at the asymptotic mean value (eq 2.14). At this point, they drift-diffuse radially. In contrast to the perpendicular migration perceived with constant gas flow, ions are now pulled back, trying to match gas and drift velocity. As the ions are pulled farther away from the center, the radial electric field becomes more prominent than either drift or gas velocity and ions are pushed toward the electrodes. It is encouraging to observe the little axial diffusion present, even though multiple ions were used to form the trajectories of each curve.

An approximation to an analytical solution can be obtained when the variation of the velocity is assumed to be small ($dv_{gas}/dr \approx 0$). Under such circumstances, the mean of the distribution is given by

$$\overline{z} = \frac{v_{max}(1 - r^2/r_0^2)}{KA}(1 - c_{zz}\mathrm{e}^{-KAt}) \tag{2.16}$$

The analytical approximation states that, as an ion diffuses radially, it has enough time to accommodate to the change in the velocity of the gas by reducing its drift velocity. This, however, would not be physically true as far away from the center and toward the electrodes: the radial drift, because of the residual radial electric field would be too large for the ion to equilibrate axial drift and gas velocity. Indeed, when comparing the mean values of the analytical approximation to the SIMION solution, as shown in Figure 2.4B, they agree remarkably well close to the center but deviate farther away from the center. This is more prominent for higher mobility ions, because diffusion occurs more quickly.

The full analytical solution should be of the type

$$\overline{z} = \frac{v_{max}(1 - 2r^2/r_0^2\mathrm{e}^{-r^2/r_0^2})}{KA}(1 - c_{zz}\mathrm{e}^{-KAt}) \tag{2.17}$$

The results from eq 2.17 are shown in Figure 4C. Note that eq 2.17 is an asymptotic solution. No attempt to find the full analytical solution is made in the present manuscript.

The importance of the parabolic velocity profile should not be underestimated, especially at atmospheric pressure, because it could seriously impair the resolution of the instrument if left unchecked. If ions are allowed to migrate through the ramp ($\Lambda < 1$) and collected by a detector, long tails might appear, because of the half-moon-shaped distributions created. Figure 2.5 shows a comparison between parabolic and constant velocity profiles when ions are collected a distance L from the particle insertion point. Figure 2.5A shows the effect of the tails when multiple mobilities are present. While the tail might not be significant for a single mobility ion, it can become a large problem when multiple mobilities are present. In contrast, Figure 2.5B shows the ions under constant gas velocity and where all ions can be easily differentiated. Although the repercussions of the tail will be of paramount importance when no RF is present, they may also become important with RF and high-mobility ions.

Aside from RF, there are ways to avoid or attenuate the problem. One possibility is to insert the ions centered in the tube. Since the radial electric field is proportional to r, it is extremely weak in the center and the radial migration of the ions can be hampered. Another way is to taper the tube so that a plug flow is formed, leading to a more constant velocity in the center. A last resort is to collect the ions only at the center with the corresponding signal loss.

2.2.4 Radial Losses and RF Confinement at Low Pressures

A relevant issue appearing when using a linearly increasing electric field in the axial direction is the appearance of a residual electric field to comply with the divergence (eqs 5 and 6). This radial field pushes the ions outward augmenting the effect of regular radial diffusion. This becomes quite problematic, especially at high pressures, where RF cannot be used. At such pressures, the only possibility to avoid large diffusion losses is to have the ions as centered as possible initially while keeping them in the tube for the shortest possible time. This requires the separation ratio Λ to be small, hampering the overall resolution that the IDT instrument can achieve.

At low pressures, RF can and should be used to contain the ions. However, the existence of the residual field (eq 6) complicates the use of RF as an all-ion guide. To study the effect of this field on the stability of the ions, an ideal RF potential for four hyperbolic rods may be superimposed on the axial potential:

$$\Phi = \frac{\Phi_0}{2r_0^2}(x^2 - y^2), \Phi_0 = U + V\cos\left(wt + \theta_0\right) \tag{2.18}$$

Here, w is the RF driving frequency, θ_0 the initial phase, and U the DC potential applied, and V the AC potentials applied. Generally, for RF guide-only mode, U should be equal to 0. With $U = 0$, and considering the effect of drag, the radial equations of motion $(\overrightarrow{F} = q\overrightarrow{E} - \overrightarrow{F}_{drag} = M\overrightarrow{a})$ in Cartesian coordinates are

$$M\frac{d^2x}{dt^2} - \frac{qx}{r_0^2}[\frac{A}{2} + V\cos\left(wt + \theta_0\right)] + \frac{q}{K}\frac{dx}{dt} = 0 \tag{2.19}$$

$$M\frac{d^2y}{dt^2} - \frac{qy}{r_0^2}[\frac{A}{2} - V\cos{(wt + \theta_0)}] + \frac{q}{K}\frac{dy}{dt} = 0 \tag{2.20}$$

Here, the third term of the two equations corresponds to the drag force, which is proportional to the velocity field of the ions' movement in x and y directions, and is given, e.g., in eq 2.19, in terms of ion mobility as $\frac{q}{K}\frac{dx}{dt}$. The electric field (second term) is a composition of the field provided by Φ and that provided by eq 2.6. Because of the residual radial electric field, the equations of motion carry a DC-equivalent potential that can not be avoided in such condition, as if U had been chosen to be $-A/2$. $A/2$, unlike U, cannot be chosen to be 0 and will play a very important role in the stability of the ions' movement. Note that this DC potential is also different from the one applied in quadrupoles [90], because it has the same sign on both eqs 2.19 and 2.20. With a change of variables, eqs 2.19 and 2.20 become the Mathieu equations:

$$\frac{d^2u}{d\xi^2} - [a_u \pm 2q_u\cos{(2\xi)}]u + \frac{2q}{wmK}\frac{du}{d\xi} = 0 \tag{2.21}$$

$$\xi = \frac{wt}{2} \tag{2.22}$$

$$a_u = \frac{2qA}{w_2 r_0^2 m} \tag{2.23}$$

$$q_u = \frac{2qV}{w_2 r_0^2 m}, \tag{2.24}$$

where u represents either x or y direction. Figure 2.6A shows the stability domain for eqs 2.21 when the drag force is considered negligible (e.g., vacuum conditions). Drag force at low pressures has been shown to have little influence on stability due to the low collision frequency between the ions and the buffer gas particles (e.g. N_2 or He), which slightly enlarging the stability region for the ions [91], [92]. Because of the requirement of always having an equivalent nonzero DC potential, not all masses are stable at all frequencies, and care must be taken to not lose ions in the process.

The motion of ions on stable trajectories is shown in Figures 2.6B and 2.6C for different initial conditions of position and velocity of the ions. When drag is not considered, the trajectories are confined to a region that is strongly dependent on the initial conditions and phase. Figure 2.6B shows trajectories with initial velocities parallel to one of the axes for θ_0 at 0° and 180°. Figure 2.6C shows initial velocities at 45°. When drag is considered, stable trajectories tend toward the center, as shown in Figures 2.6B and 2.6C. Random walk diffusion is not considered and could potentially affect the ion stability.

2.2.5 Effective Resolutions Using RF Confinements

Asymptotic Resolution of the Ramp Region

In a previous manuscript [1], it was described how resolution, in its common definition used for drift tube ion mobility, $\overline{z}/\Delta z$, was an ill-conditioned parameter for IDT. As an example, one can look at the case of an IDT with no field present where ions of different mobilities would reach the detector simultaneously. Despite the very high resolution, in terms of $\overline{z}/\Delta z$, there would be no separation. A better alternative is to use the resolving power employed in chromatography for two peaks, given by the ratio of the distance between two peak centers, $\Delta\overline{z}$, and the average full width at half $-$ maximum, $\overline{fwhm}$, minus 1:

$$R_p = \frac{\Delta\overline{z}}{FWHM} - 1 \tag{2.25}$$

From its definition, one should expect two peaks to be resolved if $R_p > 0$. R_p can be used to obtain effective resolutions. For instance, for the TIMS instrument, an effective asymptotic resolution for the ramp (trapped) region can be obtained when the separation ratio Λ reaches 1:

$$R_{\Lambda \to 1} = \frac{\overline{z}_{asym}}{FWHM_{asym}} \tag{2.26}$$

59

Here, for a resolution of 100, the instrument will be able to resolve two mobilities that differ by 1%. Given eqs 2.13 and 2.14, and assuming that, for two very close mobilities, $\overline{FWHM}_{asym} \approx 2\sqrt{2\ln{(2)}\sigma^2_{zasym}}$, the asymptotic resolution for a ramp of length L yields:

$$R_{\Lambda \to 1} = \sqrt{\frac{v^2_{gas}}{8\ln{(2)}KAD}} = \sqrt{\frac{qv_{gas}L}{8\ln{(2)}k_bTK}} = \sqrt{\frac{qAL^2}{8\ln{(2)}k_bT}} = \sqrt{\frac{qLE_{\overline{z}=L}}{8\ln{(2)}k_bT}} \qquad (2.27)$$

It is assumed that the separation ratio λ reaches one at the end of the ramp so that $\overline{z}_{asym} = L$, given that $E_{\overline{z}=L}$, the corresponding electric field $E_{\overline{z}=L} = AL$. Despite the similarity of eqs 2.27 to the DTIMS resolution, there are marked differences between the two. The most important one is that the electric field is not constant like in a DTIMS. Therefore, the field required to reach $\Lambda = 1$ at the end of the tube will be dependent on the mobility and the velocity of the gas. Moreover, given the quadratic nature of the voltage employed, one must be careful to avoid breakdown scenarios. In order to explore these dependencies, it is better to use the second expression for the resolution, which has a direct dependence on K, v_{gas}, L (eqs 2.27). Figure 2.7A shows the dependence of the resolution on reduced mobility, K_0, for a $L = 50cm$ ramp with different gas velocities, v_{gas}, ranging from 50 m/s to 200 m/s at two different pressures and a temperature of 300 K. Resolution shows an inverse square-root dependence with mobility and a marked increase at higher pressures. At a commonly used gas flow of 150 m/s [85], resolutions of ~ 200 can be reached for reduced mobilities of $K_0 = 0.5cm^2/(Vs)$ $(CCS \approx 210A^2)$. However, the voltage required to trap this mobility would be $\sim 4.0kV$ at 0.5 m $(V = v_{gas}L/2K)$. For different reduced mobilities $K_0 = 0.3 - 1.1cm^2/(Vs)$, the change in resolution with gas velocity for $L = 50cm$ and pressure of 2.5 Torr is given in Figure 2.7B. The resolution of the ramp region has been somewhat ignored in previous theoretical assessments of the TIMS instrument, because of the difficulty in solving eqs $2.2 - 2.4$. As shown here, it could be of strong consequence if treated correctly and especially if coupled with the plateau region of the TIMS described below.

Resolution in the Plateau Region

To take advantage of the ramp separation and asymptotic resolution, a way to elute the ions must be included to collect them in a detector or be transferred to a mass spectrometer. The most reasonable way to elute the ions is to reduce the slope A of the electric field a sufficient amount so that ions drift outside of the trapping region. Once lowered, the ions start moving through the plateau region. This plateau region follows a separation procedure similar to that of the drift tube but where the velocity of the gas carries the ion forward while the position-independent electric field, E_e, opposes the flow. Using the definition of resolving power, one can calculate the effective resolution for a plateau of length L_2:

$$R_{plateau} = \sqrt{\frac{qL_2\Lambda_p E_e}{(1 - \Lambda_p)16\ln 2 k_b T}} = \sqrt{\frac{qL_{2,eff}E_e}{16\ln 2 k_b T}} \tag{2.28}$$

Here, the separation ratio in the plateau, $\Lambda_p = KE_e/v_{gas}$, must be < 1 to allow ions to move through the plateau with velocity $\overrightarrow{v}_{ion} = \overrightarrow{v}_{gas}(1-\Lambda_p)$. The closer Λ_p is to 1, the higher the resolution. One can introduce an effective length, $L_{2,eff} = L_2\Lambda_p/(1 - \Lambda_p)$, to compare the plateau region to a DTIMS. One can drastically increase the effective length to boost the resolution, e.g., by ~ 10 -fold at $\Lambda_p = 0.99$. However, the increase in resolution comes at a cost. Since the elution is time-based and there is no diffusion control in the plateau, peaks will have a tendency to broaden as they become separated, greatly decreasing the peak maximums. A compromise must then be made between maximum peak intensity and resolution. Equation 2.28 differs from the resolution previously derived for the TIMS [64]. Aside from other simplifications, the previous resolution assumed that the eluting electric field changes over time at a given rate. Resolution in eq 2.28 can consider changes in the electric field by assuming that the separation ratio changes with time, $\Lambda_p = \Lambda_p(t)$. In fact, for linear changes in the slope of the field, an average value of the separation ratio $\overline{\Lambda}_p$ can be used as a substitute in eq 2.28. Λ_p can then be related to the scan rate β by

$$\overline{\Lambda}_p = 1 - \sqrt{\frac{L_2 K \beta}{2v_{gas}^2}} \tag{2.29}$$

Combined Resolution for TIMS

The overall resolution is a complicated convolution of both regions, ramp and plateau, and is given by

$$R_{total} = \frac{(L_{2,eff} + L)\sqrt{E_e q}}{8 \ln 2 k_b T (L\overline{\Lambda}_p + 2L_{2,eff})} \tag{2.30}$$

When $L_{2,eff} \gg L$, i.e., the effective plateau length is much larger than the length of the ramp region, eq 2.30 reduces to previous reported resolutions except for a factor of $\overline{\Lambda}_p$, perhaps because of different simplifications [64]. Figure 2.7C shows the combined resolution for a plateau length of $L_2 = 50cm$, as a function of the change in $\overline{\Lambda}_p$ from 0.7 to 0.99 for different reduced mobilities K_0. While resolutions are extremely high for very high plateau separation ratios, it will involve losing maximum peak intensity, and care must be taken. It is easy to observe that the length of the plateau L_2 is not as important as the separation ratio ($\overline{\Lambda}_p$) used. In principle, one could have a very small physical length and still achieve high separation if a large separation ratio $\overline{\Lambda}_p$ would be employed. In fact, this can be observed when one tries to obtain the resolution of the TIMS instrument with only 46 mm in length. Figure 2.7D shows such resolution as a function of the scan rate, β, using eq 2.29 and assuming that the scan rate is linear with time, as is the case in TIMS. The slower the scan rate, the higher the resolution (higher average separation ratios). The proportionality $R_{total} \approx \beta^{-0.25}$ in Figure 2.7D is not exact as derived from the equations. Under all scenarios presented, it is considered that the ions inside the ramp have reached its asymptotic condition. This might not be the case if the scan rate is too fast.

The resolutions obtained here should be considered an upper bound, since they neglect the effects of parabolic velocity profiles. However, $R \approx 400$ have already been obtained experimentally in TIMS revealing the instrument possibilities [93]. The greatest benefit of these systems, not possible in a DTIMS, is that, regardless of the initial width of the package of ions, well-defined asymptotic distributions are guaranteed at the beginning of the plateau region, thanks to the confinement in the ramp.
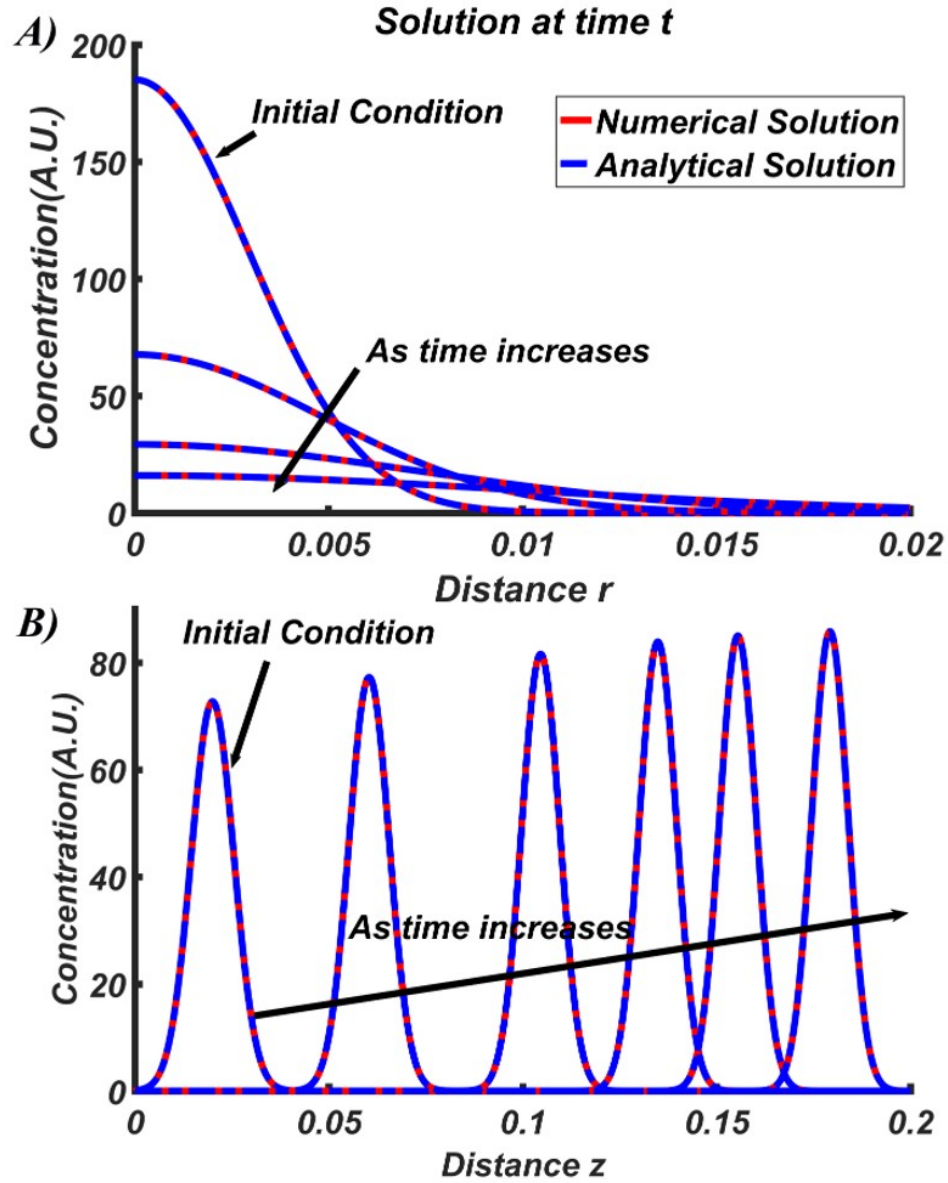
Figure 2.2. Comparison of numerical and analytical solutions (from eqs 2.9 − 2.11)) for (A) the radial direction and (B) the axial direction. If a broad distribution is chosen initially in the axial direction, it is not only constrained but narrows as time passes.
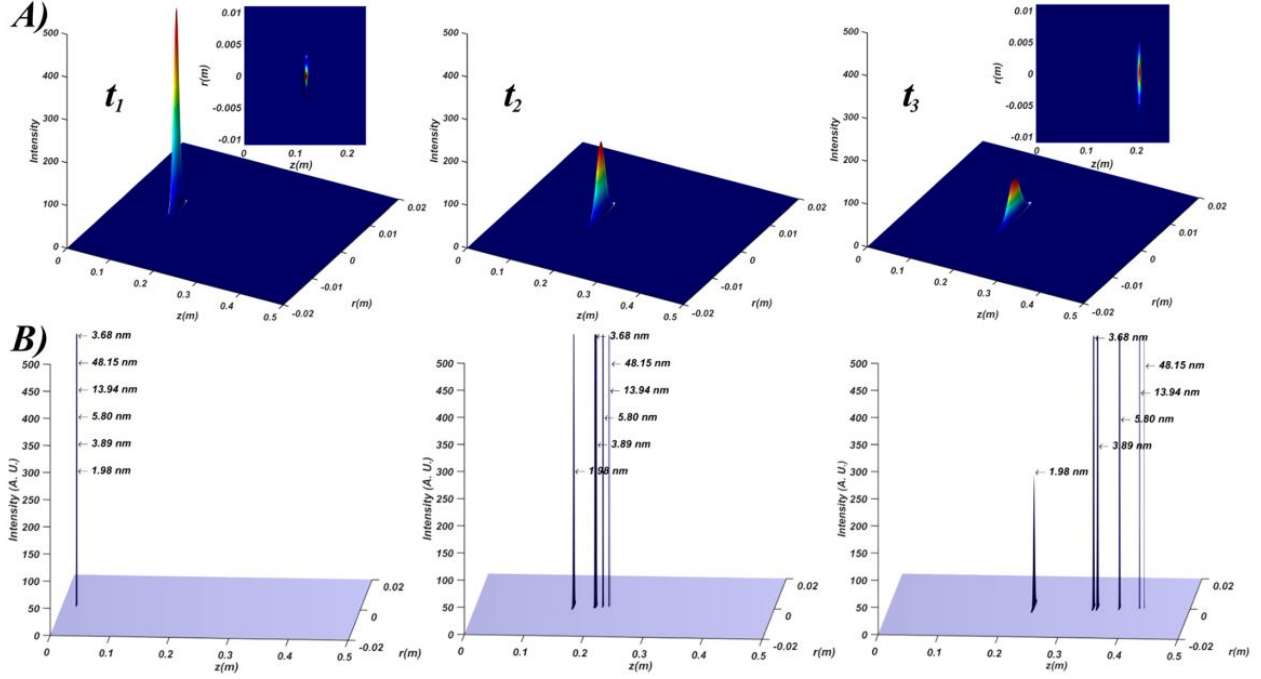
Figure 2.3. (A) Evolution of a three-dimensional mobility distribution as it progresses through the ramp region of the instrument at three different instants in time (no RF). As the distribution progresses, ions freely migrate radially but are contained in the axial direction (see insets). The axial distribution width has been purposefully enhanced by a factor of 10. (B) Evolution of packets of ions of different mobilities (singly charged spheres of given diameters) as they are being separated in the ramp region. More mobile ions diffuse more radially. However, they are all contained axially.
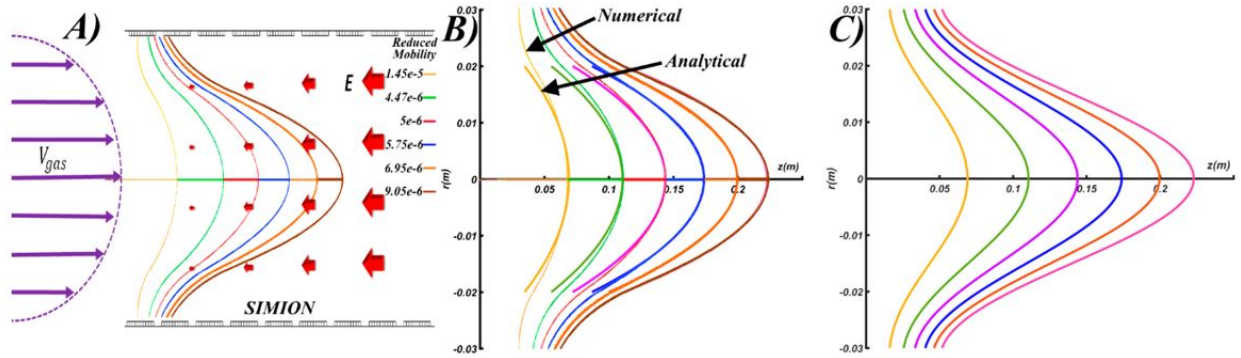
Figure 2.4. (A) SIMION 8.1 trajectory results of packages of singly charged spherical ions of six different mobilities being axially trapped in a tube with a parabolic velocity profile and no RF. Ions start centered, migrate through the tube, and stop when $\Lambda = 1$. At that point, they drift $-$ diffuse radially. (B) Superposition of analytical approximation eq 2.16 when $(dv_{gas})/dr \approx 0$ and SIMION 8.1 trajectories. (C) Analytical approximation using eq 2.17.

64
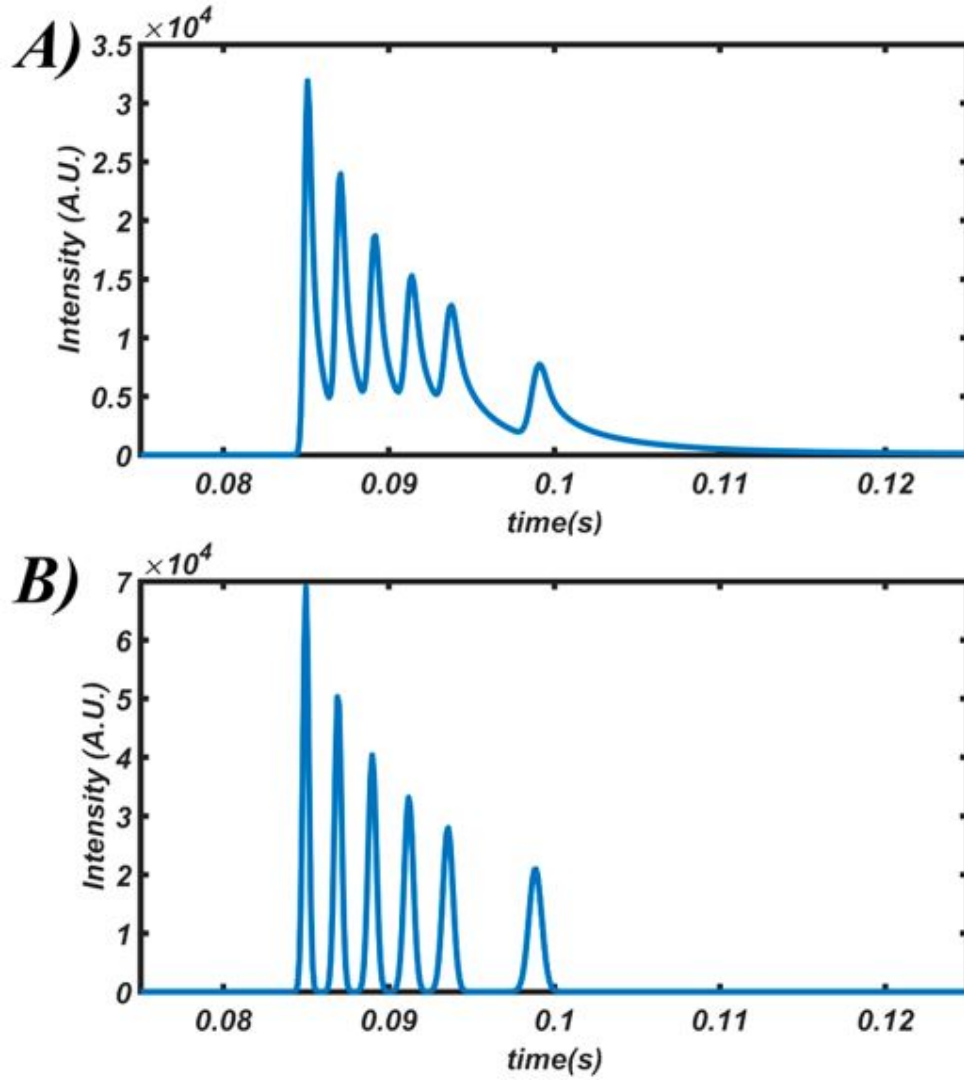
Figure 2.5. Intensity as a function of time for ions collected a distance L downstream in an IDT with no RF for (A) a parabolic velocity profile and (B) a constant velocity profile. Note the effect of the tails created in panel (A).
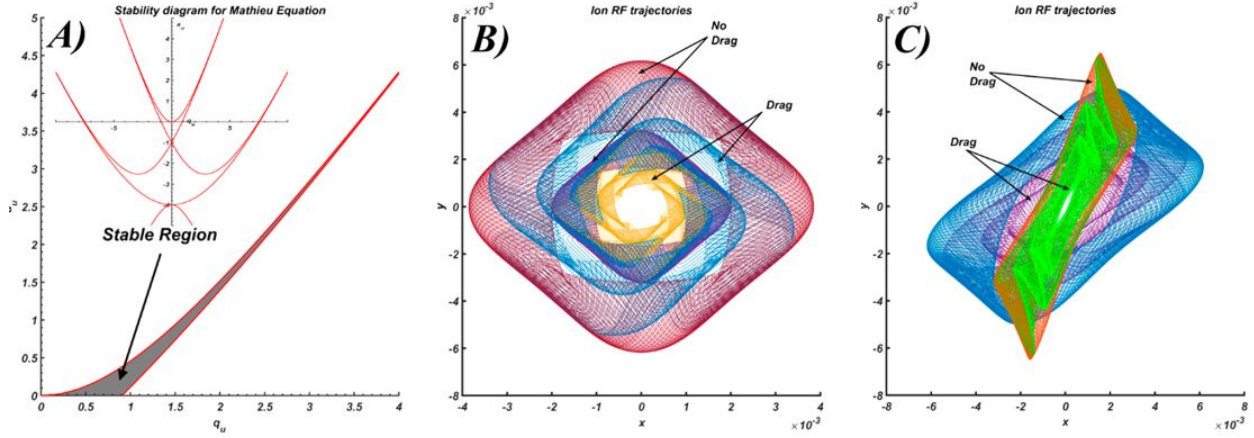
Figure 2.6. (A) Stability region of eq 20. For a positive A, the stable region is shown in gray while an enlarged stability domain is shown in the inset. (B) RF confinement ion trajectories with and without drag for initial velocities parallel to one of the axes and non-centered initial positions. (C) RF confinement ion trajectories with and without drag for initial velocities at 45°.
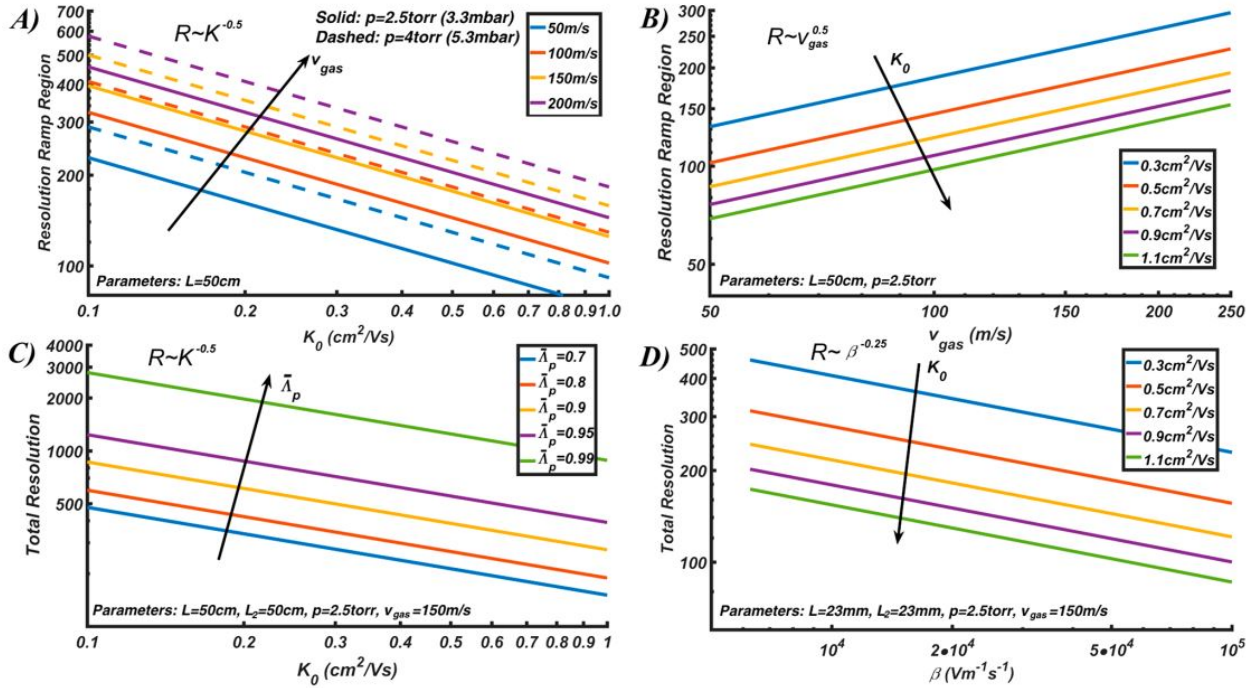
Figure 2.7. Asymptotic resolutions of the ramp and plateau regions. (A) Ramp resolution $R_{\Lambda \to 1}$ as a function of reduced mobility K_0 for different gas velocities. (B) $R_{\Lambda \to 1}$ as a function of v_{gas} for different reduced mobilities K_0. (C) R_{total}, as a function of reduced mobility K_0, for different average separation ratios $\overline{\Lambda}_p$. (D) R_{total}, as a function of the scan rate β for different reduced mobilities.

66

3. HIGH RESOLUTION VARYING FIELD DRIFT TUBE ION MOBILITY SPECTROMETER WITH DIFFUSION AUTOCORRECTION

This section is from a published manuscript of the author of this dissertation from ref. [94]. Author Xi Chen has contributed to the methodology, design of the experiment, data analysis and writing of the original draft. Author Dr. Carlos Larriba-Andaluz (the corresponding author) has contributed to the theoretical calculation, review and edition of the manuscript. Author Viraj Gandhi, Joshua Coots, Yinghui Fan, Liang Xu and Dr. Nobuhiko Fukushima have contributed to the review of the manuscript.

3.1 Overview

Drift Tubes (DT) have been used prominently to classify ions in the gas phase and its simplicity has made it the Ion Mobility Spectrometer (IMS) of choice for analytical chemists [95]. This is in juxtaposition to its very limited or negligible use in aerosol science, where the Differential Mobility Analyzer has been the tool of choice even for ions as small as a few nanometers [46]. There are obvious reasons for both choices, but there are some inherent advantages to each system that should not be ignored by the other field. The DMA coupled to a Condensation Particle Counter (CPC) [96], in what has been known to date as a scanning mobility particle sizer (SMPS) [48], has very high transmission and measurement range although many commercially available systems have low resolution [51], are relatively slow and suffer from diffusion problems for small nanometer sizes [65]. On the other hand, the DT has relatively higher resolution, it is generally faster than a regular scanning DMA but has lower transmission (due to its duty cycle), and its measurement range is, in general, limited to a few nanometers [28], [54].

It is noteworthy to mention that some of the points addressed in the previous paragraph are generalizations. There exist high resolution DMA systems which can reach resolutions in excess of 100 [34], [97] and there are plenty of studies on improving the transmission and reducing diffusion losses for small ions in DMAs [98], [99]. Another issue that requires

clarifcation is that pertaining to the characterization speed of the instruments. While a scanning DMA may take several minutes to collect the spectra, one can potentially have response times in a DMA of tens to hundreds of microseconds (the residence time in the DMA). In contrast, not all DTs have poor transmission, there are some that use a Hadamard transform with convoluted pulsing times which increase overall transmission to 50% [100], [101].

In all, given the capability of DT systems, their use should be naturally extended to the study of aerosols. In fact, there are plenty of examples of atmospheric pressure drift tubes with high resolution to study small ions [102]–[105]. Despite this, it has not been until very recently that there has been a major push to bring the technology into the aerosol field [57], [106], [107]. The reasons behind its lack of use might have been the necessity for a fast response CPC, the limited size range, or the inability to bring a flow of charged particles into a high voltage DT system. Whatever the reason, new technology is now becoming available to overcome these deficiencies and thus the DT should eventually become a useful tool for sub 100 nm aerosol particles.

The operational principle of a DT system is quite simple. A constant field generated by a series of cylindrical electrodes is used to propagate a swarm of ions of different mobilities into a detector where an arrival time distribution is recorded. In order to correctly quantify this time, the ions are pulsed into the system through a gate at known intervals. In this way, the resolution of an initial point source distribution is given by [53]:

$$R_{DT-IMS} = \frac{\overline{x}}{\Delta x} = \frac{tv_{drift}}{(16D_L t \ln 2)^{1/2}} = (\frac{qEL}{16k_b t \ln 2})^{1/2} \tag{3.1}$$

where q is the charge, E is the electric field, L is the tube length, k_b is the Boltzmann constant and D_L is the longitudinal diffusion and T is the temperature. It seems evident that the resolution is proportional to the square root of the electric field and the length of the tube. Equation (3.1), however, is sometimes misleading as the initial ion package width is impossible to be infinitesimal [55], and the resolution should be related to the initial distribution. Actually, the initial package width greatly impacts resolution and leads to a maximum possible theoretical resolution which does not occur at the highest field.

This initial package diffuses as it travels through the system, worsening resolution-due to longitudinal diffusion-as well as transmission-due to transversal diffusion. The larger the initial distribution, the wider of the final ion distribution. It suffices to say that controlling or correcting diffusion would increase the resolution and transmission of the system.

Attempts at diffusion correction have been done previously. In particular, transversal diffusion has been corrected at low pressures by using radio frequency (RF) technology, but the high voltage and frequency needed precludes its use at atmospheric pressure. RF technology can be observed in extremely long drift tubes, either in portions of the system where a funnel centers the ions [51], or throughout the whole path length such as in Structures for Lossless Ion Manipulation (SLIM) [108], [109]. Studies aimed at correcting longitudinal diffusion are more scarce. In such systems, a non-constant field in the axial direction is used to constrict axial diffusion. The concept of using a varying field is not new. It was first attempted by Zeleny [63] in the 19th century and later on used mostly conceptually for multiple geometries and different pressures. The principle is based on the solenoidal principle of an unperturbed electric field ($\nabla \cdot E = 0$) that suggests a variation of a field can be used to compress the ions in a particular dimension while stretching them in another. At low pressures, a commercially available system that makes use of this principle is the Trapped Ion Mobility Spectrometer (TIMS) which, as the name suggests, traps the ions thanks to varying fields and the use of RF to subsequently release them [62]. At atmospheric pressure, there are a few systems that have taken advantage of nonlinear fields. Interestingly, one of its first appearances was to improve DMA resolution through the reduction of diffusive broadening in what was labeled a Drift Differential Mobility Analyzer [110]. Ion compression was also observed when studying the three zones of Bradbury-Nielsen type gates where "the enlarged depletion zone, the reduced dispersion zone, and the electrically enhanced compression zone consistently help to produce narrower peaks" [111]. This non-uniform field idea was later explored by the same authors to increase the sensitivity of Ion Mobility Spectrometers [112]. The principle of the IDT [1], [2] has been recently explored where a gas flow pushes the ions forward while a linearly increasing electric field is used as a means to separate them. Since no RF can be used, the IDT suffers from loss of signal due to an enhanced radial dilation of the ion distribution and the difficulty of aligning the centers of symmetry of field and gas.

In this manuscript, the knowledge gained with the IDT is put to the test to develop a new type of Drift Tube that uses a varying electric field and benefits from diffusion correction. In the Varying Field Drift Tube (VFDT), a linearly decreasing electric field is employed to propagate the ions forward which allows for diffusion constriction to occur axially. An experimental prototype is used to show that resolutions of 90 or more are achievable for singly charged small ions (1-3 nm), but where there is no particular limitation to achieve high resolution for larger particles as well. The theoretical expression for the resolution is inferred from the Nernst-Planck ion balance equation revealing that the asymptotic resolution of the VFDT is higher than that of the DT even for an infinitesimal source. It is also shown that when starting with an initially broad distribution in the axial direction, a narrower distribution can be collected at the end of the tube making this system unique. The drawback is that the distribution is constricted axially at the expense of enlarging it radially [1], [2]. The effect of enhanced radial diffusion can be shown theoretically to be negligible as long as the distribution is kept in the center of the tube. The transformation from arrival time distribution to mobility depends on the slope of the electric field but it is a simple linear transformation for all mobilities. Finally, the transformation from mobility to diameter of Collision Cross Section (CCS) can be done using Stokes-Millikan's or Mason-Schamp's equation and a comparison to models using Molecular Dynamics is performed.

3.2 Experimental setup and methods

3.2.1 VFDT construction

The construction is loosely based on the existing conventional Drift Tube from Kanomax (Osaka, Japan) and a brief description of the modifications will be provided here [57]. As depicted in Fig. 3.1, the VFDT consists of a 3 cm ionization region and a $\sim$ 18 cm drift region, which are separated by three layers of metallic grids (red color dotted lines) $2 - 3$ mm apart. The second grid serves as the gating electrode which is connected to a Behlke pulser (HTS 21-03-GSM, Germany) providing an asymmetric high voltage square wave by means of a Siglent wave generator (Model SDG 2042 X, OH, USA). The asymmetric square wave allows the selection of both the pulsing time and the maximum drift time allowed.

The other two grids are connected to different high voltages ($10kV$ and $8kV$ in Fig. 3.1) to provide a field for the ions to travel through the gate and to serve as a shield to avoid any interference of the pulse with the drift field and/or detector. When the pulser provides a voltage of a few hundred volts below the voltage of the third mesh (e.g. $\sim 7.5kV$), the ions are not permitted into the drift region. Raising it a few hundred volts over the third mesh (e.g.$8.5 \sim 9kV$) provides a positive field for the ions to pass the gate. This field is then used to establish the pulse time for a particular mobility by subtracting the residence time between the second and third grid from the pulse time of the wave generator. For $1 - 3$ nm ions, this residence time is theoretically less than $100\mu s$. However, from experimental observation, the effective residence time seems to be closer to $400\mu s - 600\mu s$ (no ions can be observed below a given pulse time) so $400\mu s$ was chosen as the residence time. While this method might lead to overestimating the pulse time due to hectic ions, it seems the most reasonable choice without a more thorough study of the gate. Within the drift region, a combination of two electric fields, a linearly decreasing field followed by a constant field, was generated using a series of resistors as shown in an inset of Fig. 3.1. The first portion corresponds to a linearly decreasing electric field while the second portion provides a constant electric field that is used to push the ions into the detector. A shielded Faraday cage was used as the ion detector connected to a Keithley electrometer (Model 428-PROG, FL, USA) with a 1e10 amplification and a $300\mu s$ filter to reduce the noise coming from the pulser. While an ionization region exists where a radioactive source can be placed to charge airborne particles, for the experiments shown in this work, an electrospray system was installed in the front of the system. The voltage applied was around $2kV$ higher than the first electrode and a floating HV power supply was used to deliver the voltage (EMCO HV, Now Spellman, E121). The inner diameter of both ionization region and drift region is 40 mm. The system was open to atmospheric pressure and operated at room temperature conditions (around $20°C$). A flow may be used when necessary to provide further control on the ions flowing to the detector and to maximize the signal.
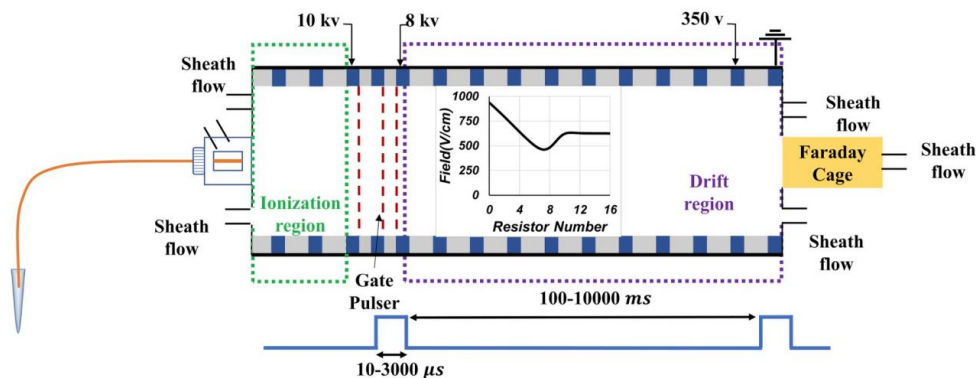
Figure 3.1. Experimental sketch of the Varying Field Drift Tube with an Electrospray source. An inset with the electric field used experimentally is provided

3.2.2 Chemicals and reagents

Four tetraalkylammonium bromides salts were purchased from Sigma-Aldrich (St. Louis, MO), including tetrabutylammonium bromide (TBA), tetrapentylammonium bromide (TPA), tetrahexylammonium bromide (TXA) and tetraheptylammonium bromide (THA). These salts were dissolved into a concentration of $15mM$, $15mM$, $7mM$ and $7mM$ respectively, in a solution of 50%/50% of methanol/water. The solution was placed inside a pressurized polypropylene vial and pushed through a silica capillary (ID: $40\mu m$, OD: $360\mu m$, Polymicro Technologies) to the tip where a Taylor Cone was created and the solution electrosprayed.

3.2.3 Experimental methods

To study the effect of the varying field on the ions, a series of experiments were performed. An initial series of experiments were run using different pulse times to study the arrival time of the ions and whether or not the arrival time correlated linearly with mobility. To study the effect of the pulsing time and voltage on the resolution, two experiments were performed; the first consisting of a variation of the initial pulse time keeping the voltage fixed while the second one corresponding to a variation of the voltage with fixed pulse. Finally, to verify whether or not diffusion autocorrection was occurring in the system, a test comparing a constant field DT and the VFDT was performed.

3.3   Results and discussion

3.3.1   Insight into pulsing time and its importance for characterizing larger aerosol particles

When a pulsing voltage is used to gate the ions into the drift region, the width of the pulse t_{pulse} strongly affects the signal and resolution of the distribution of ions. An example of such scenario can be made apparent by means of the models illustrated in Fig. 3.2. The width of the pulse establishes in a sense the width of the initial distribution that is inserted into the drift region. The larger the width of the pulse, the larger the amount of ions inside the system and therefore the larger signal gain. However, this initial breadth negatively affects the resolution. In Fig. 3.2, the 2D axisymmetric Nernst-Planck solution for a conventional drift tube has been used to describe the drift of two packets of ions of different mobilities. The figure is taken at an instant inside the drift tube. On the left figure, the smaller t_{pulse} allows the ions to be fully separated at the cost of having much smaller signal. On the right, an initially larger t_{pulse} makes the separation barely visible for the same drift tube characteristics. However, there is a clear increase in signal intensity. As an example, the expected resolution for a 1.2 nm particle in a 9 kV, 20 cm drift tube would be 29 for a 1 ms pulse and 60 for a 0.5 ms.

The issue does not end there. Ions that during the pulse time do not cover the physical distance between the gated mesh and the mesh downstream will be lost. This is, in particular, problematic for larger ions and nanoparticles with very small mobilities as their drift velocity is small. For this purpose, a very large pulse time is needed in order to get signal through the gate. This increase in pulse time worsens the resolution of all ions that are more mobile making the DT very inconvenient for larger aerosol particles. Under such circumstances, it might be more reasonable to divide the collection of the spectra into two or more regions with different pulsing times.

It would be a great advantage if one could conveniently use a higher signal while still being able to separate the ions at high resolution. The purpose of this manuscript is to show that it is indeed possible by taking advantage of diffusion autocorrection to obtain high resolutions even when large pulse times are used at the pulsed gate.
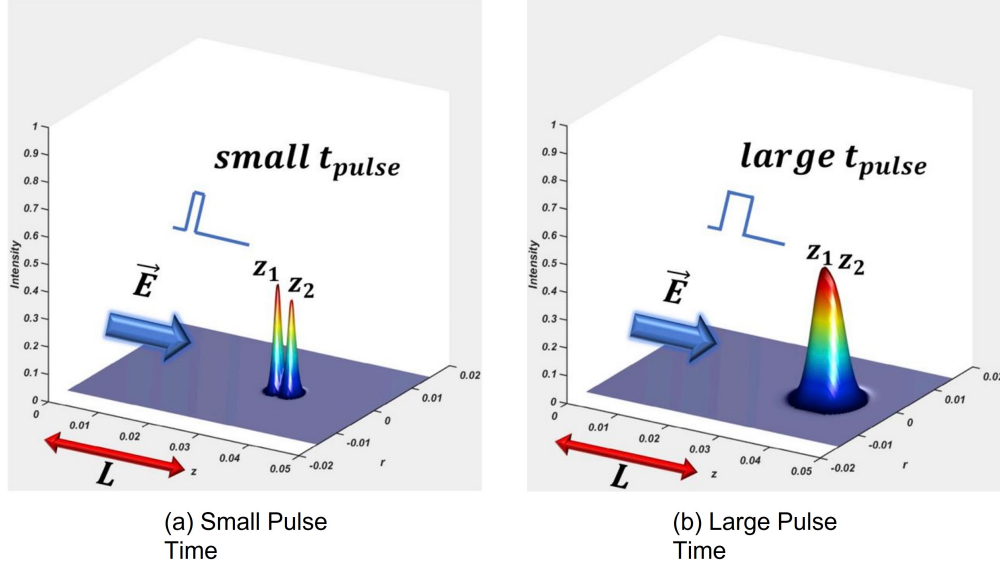
Figure 3.2. Resolution and signal intensity for two t_{pulse} for two ion distributions of different mobilities migrating through a Drift Tube as simulated using the Nernst-Planck equation for constant field. While the small pulse allows the two ions to be resolved, the larger pulse allows more signal.

3.3.2 Theoretical interpretation of the Varying Field Drift Tube and comparison to regular drift tubes

In order to first understand the reasoning behind diffusion autocorrection, it is necessary to interpret the problem theoretically. Consider a population of ions $n(z, r, t)$ of a single species created at one end of a cylindrically symmetric drift space with uniform gas of number density N. This population is subject to a linearly decreasing electric field $E = A(L_E - z)$ in the axial direction. A is the slope of the electric field while L_E is the distance at which the field becomes zero, which can be larger than the total characterization distance inside the drift tube. For an ion of mobility Z, assuming E/N is small, the Nernst-Planck equation is given by:

$$\frac{\partial n(z, r, t)}{\partial t} - \nabla \cdot (\overline{\overline{D}} \cdot \nabla n(z, r, t) - Z\vec{E}n(z, r, t)) = 0 \tag{3.2}$$

$$n(\pm\infty, \pm\infty, t) = 0 \tag{3.3}$$

$$n(z, r, 0) = f(z, r) \tag{3.4}$$

where $f(z, r)$ corresponds to the initial concentration regardless of whether it is a normal distribution or a point source. In eq. (3.2), $\overline{\overline{D}}$ is the isotropic diffusion tensor which is assumed constant. The initial condition for a total count n_s is:

$$n(z, r, 0) = f(z, r) = \frac{n_s}{(2\pi)^{\frac{3}{2}}\sqrt{\sigma_{z0}^2 \sigma_{r0}^2}} e^{-\frac{(z-\overline{z0})^2}{2\sigma_{z0}^2}} e^{-\frac{r^2}{2\sigma_{r0}^2}} \tag{3.5}$$

$$\sigma_{z0}^2 = \frac{k_b T}{qA}(1 - c_{z\sigma}); \sigma_{r0}^2 = \frac{2D_r}{ZA}(c_{r\sigma} - 1) \tag{3.6}$$

$$\sigma_{z0}^2 = \frac{k_b T}{qA}(1 - c_{z\sigma}); \sigma_{r0}^2 = \frac{2D_r}{ZA}(c_{r\sigma} - 1) \tag{3.7}$$

$$\overline{z_0} = L_E(1 - c_{zz}) \tag{3.8}$$

Here, $c_{z\sigma} \leq 1$, $c_{r\sigma} \geq 1$ and $c_{zz} \leq 1$ are constant. Any mean value or standard deviation of a normal distribution can therefore be chosen as the initial condition. Choosing the value of the constants to be one will provide a point source distribution. Neglecting the existence of free charge leads to a second equation:

$$\nabla \cdot \overrightarrow{E} = 0 \tag{3.9}$$

Provided that the field is known in the axial direction as defined previously, the solenoidal aspect of the field yields the solution to the radial electric field, which could be wrote as:

$$\overrightarrow{E_r} = \frac{Ar}{2}\overrightarrow{U_r} \tag{3.10}$$

Assuming there is no correlation between radial and axial directions, the balance population can be written as $n(z,r,t) = n_z(z,t)n_r(r,t)$ and a unique solution can be obtained when the initial condition is either a point or a gaussian distribution:

$$n(z,r,t) = \frac{n_s}{(2\pi)^{\frac{3}{2}}\sqrt{\sigma_{z0}^2\sigma_{r0}^2}} e^{-\frac{(z-\overline{z0})^2}{2\sigma_{z0}^2}} e^{-\frac{r^2}{2\sigma_{r0}^2}} \tag{3.11}$$

with:

$$\sigma_z^2 = \frac{D_L}{ZA}(1 - c_{z\sigma}e^{-2ZAt}) = \frac{k_bT}{qA}(1 - c_{z\sigma}e^{-2ZAt}) \tag{3.12}$$

$$\sigma_r^2 = \frac{2D_r}{ZA}(c_{z\sigma}e^{ZAt} - 1) \tag{3.13}$$

$$\overline{z} = L_E(1 - c_{zz}e^{-ZAt}) \tag{3.14}$$

There are a couple of notable features of the VFDT that need to be mentioned at this point. The first one is that eq. (3.12) shows that the standard deviation in the axial direction asymptotes to the value of $\sigma_z^2 = k_bT/qA$ as time goes to infinity, providing a diffusion restriction in the axial direction. This differs from the regular drift tube where the standard deviation goes to infinity as time goes to infinity. It is true nonetheless that $\overline{z} = LE$ is not an experimentally feasible result so the detector is naturally placed at a distance $L < L_E$.

The resolution, R, of a varying feld region at a position $L < L_E$ for an infinitesimally small initial distribution, is given by the ratio of the average position of the ions divided by the average full width at half maximum, $\overline{FWHM} = \sqrt{8\ln(2)\sigma_z^2}$, of the peak distribution in the axial direction:

$$R_{VFDT} = \frac{\overline{z}}{\overline{FWHM}} = \sqrt{\frac{qLAL}{8\ln(2)k_bT}}\frac{1 - e^{-ZAt}}{\sqrt{1 - e^{-2ZAt}}} = \frac{L}{L_E}\sqrt{\frac{qL_EE_{max}}{8\ln(2)k_bT}}\frac{1 - e^{-ZAt}}{\sqrt{1 - e^{-2ZAt}}} \tag{3.15}$$

where $E_{max} = AL_E$. As t goes to infinity and $L \sim L_E$, the resolution will be:

$$R_{VFDT,t\to\infty} = \sqrt{\frac{qL_E E_{max}}{8\ln(2)k_b T}} \tag{3.16}$$

which is $\sqrt{2} \sim 1.414$ larger than the regular drift tube resolution for $L = L_E$ and constant electric field E_{max}. For a non-infinitesimal initial distribution, the resolution would become:

$$R_{VFDT} = \frac{\overline{z}}{FWHM} = \sqrt{\frac{qL_E E_{max}}{8\ln(2)k_b T}} \frac{(L/L_E)^2}{\sqrt{1 - c_{z\sigma}(1 - 2L/L_E + (L/L_E)^2)}} \tag{3.17}$$

Note in eq. (3.17) that as $L \sim L_E$, the term multiplied by the constant $c_{z\sigma}$ goes to zero. This implies that the VFDT eventually corrects any initial distribution width. This result deviates from the usual DT resolution which will only increase over any initial distribution. As a matter of fact, the resolution for a regular DT with initial standard deviation σ_{z0}, field E_{max} (or voltage $V_0 = E_{max}L$) is given by [55]:

$$R_{DT} = \frac{L}{\sqrt{\frac{16\ln 2 k_b T L}{qE_{max}} + 8\ln 2\sigma_{z0}^2}} = \frac{1}{\sqrt{\frac{16k_b T \ln 2}{qV_0} + \frac{t_{pulse}^2}{t^2}}} \tag{3.18}$$

As can be interpreted from eq. (3.18), the width of the initial distribution has a very strong effect on total resolution. The larger the initial width, the poorer the resolution and there is no possibility to correct it for a DT. Comparison between resolution of DT and VFDT for different L/L_E ratios, pulsing times and different fields are provided in Fig. 3.3. As shown in Fig. 3.3 (a), for an infinitesimally small distribution, $7kV$ ($14kV$ for DT corresponding to the same E_{max}) and a fixed length L_E of 18 cm, the DT performs better than the VFDT until $L/L_E > 1/4(\sqrt{17} - 1) \approx 0.7808$ where the VFDT starts performing better. This is nonetheless an ideal case. When for example an initial pulse of $600\mu s$ is considered, also shown in Fig. 3.3 (a), the VFDT markedly outperforms the DT for any $L > 0.5L_E$. This is the case for any pulse time used as can be seen in Fig. 3.3 (b) for a fixed ratio $L/L_E = 0.9$. Although as present, the effect of the initial width of the distribution is much smaller in the VFDT. It is also interesting to note that due to the pulse time, the highest initial voltage or field does not necessarily guarantee the highest resolution. In fact, lower voltage increases

the arrival time and reduces the overall effect of the pulse time increasing resolution. To explore this in more detail, one can plot the resolution as a function of the electric field as presented in Fig. 3.3 (c) for different pulsing times and $L/L_E = 0.9$. For all the cases explored except the point source, the resolution peaks at a maximum (which can be easily inferred from the equations) that depends on the voltage employed and the pulse time. It is evident though that the VFDT outperforms the DT for all voltages and pulses considered.

3.3.3 Experimental validation of the varying field system

To avoid leaving the ions inside the drift region for too long leading to unwanted diffusion, our experimental setup is made up of two regions, an initial VFDT region that corrects the initial pulse, followed by a DT region similarly to what is observed in the example inset of Fig. 3.1. This will result in a lower resolution than theoretically predicted for the VFDT but will allow larger particles to be collected faster and with a higher overall signal.
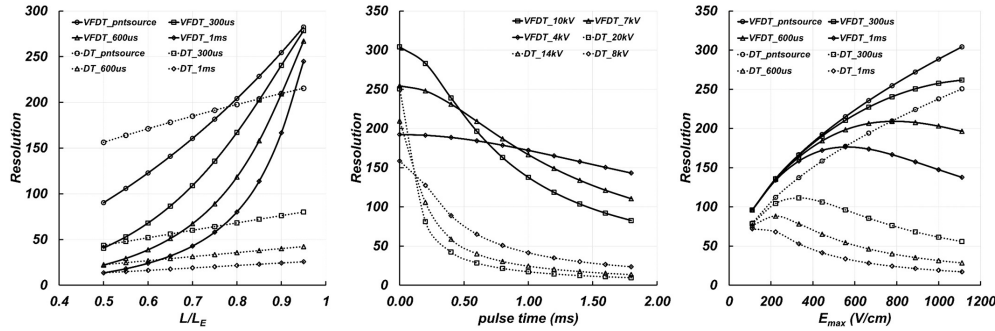
Figure 3.3. A) Resolution as function of the ratio L/L_E for a fixed L_E and $7kV$ for VFDT (solid) and $14kV$ DT (dashed) and different pulses. B) Resolution as a function of pulse time for different voltages (to match initial E_{max}, the initial voltage is twice that of the VFDT) for VFDT (solid) and DT (dashed) for $L/L_E = 0.9$. C)Resolution as a function of E_{max} for $L/L_E = 0.9$ and different pulsing times for VFDT (solid) and DT (dashed).

The intensity as a function of the raw arrival time distribution of an electrosprayed mixture of tetraalkylammonium salts is shown in Fig. 3.4. In order to recreate this figure, two different pulsing times were used for a voltage of $7kV$. To obtain the first 80 ms of the plot, a pulse time of 0.9 ms was employed while a pulse of 2.6 ms was used to obtain the

signal after 80 ms. The reason behind this choice is based on the fact that a higher resolution is obtained for the first pulse while a larger pulse can be used to obtain higher signal in the second set of ions without qualitative loss of information. A set of easily distinguishable peaks is produced by the mixture of salts. The first four peaks in the figure, labeled as C_x^+, correspond to the monomer peaks formed of a single cation and ordered by size. The peaks that follow, dimers, trimers and multimers, are formed by mixtures of neutral pairs and a cation. The difficulty resides in the fact that since the salts were mixed in the sample prior to electrospraying, the neutral pairs and cations may originate from different salts which convolutes the elucidation of the system. Careful study reveals the origin of the peaks as labeled in the form $[C_x Br]C_y^+$, where x and y may correspond to the same or different salts. An ion mobility-mass spectrometry study confirmed that this is indeed the correct assignment of the peaks. For 0.9 ms at $7kV$, the resolution achieved for the dimer peaks is around 80, which is significantly higher than the predicted resolution of a DT while about 1.7 times below the theoretical value predicted for the VFDT.
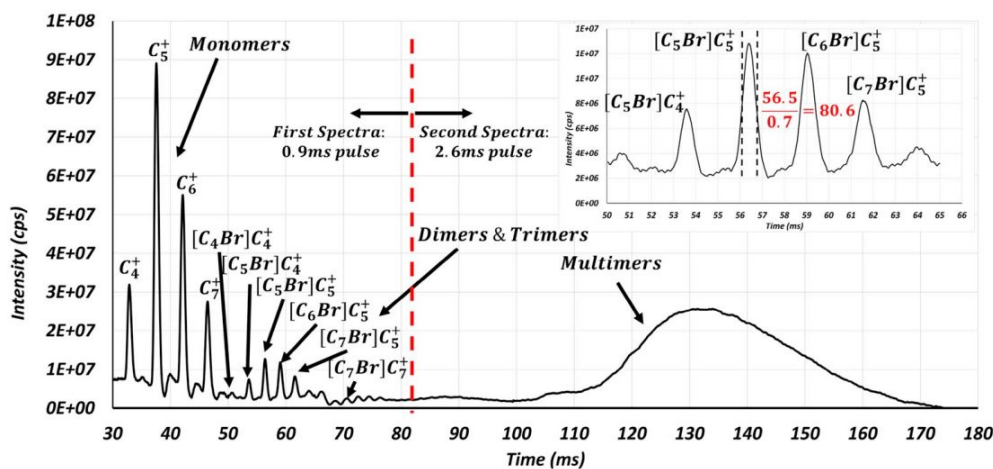
Figure 3.4. Intensity as a function of arrival time distribution for a mixture of four tetraalkylammonium salts. The monomer and dimer peaks are labeled using the nomenclature $[C_x Br]_n C_y^+$ where C_i corresponds to the alkyl chain length. To recreate this spectra, two different pulses were used, 0.9 ms for the first 80 ms and 2.6 ms for the rest. This allows larger ions to be collected without losing resolution.

A transformation of drift time to diameter is necessary for a careful study of the analyties in the system. The transformation can be easily calculated if the parameters chosen for the electric field are known. It turns out that the relation between drift time and mobility is quite similar to that of the voltage-mobility in a DMA which allows for a very simple transformation. For the initial voltage used in this experiment:

$$Z = \frac{L^2}{tV_0}(0.5 - \frac{\ln(1/3)}{2})$$

(3.19)

where V_0 is the initial voltage employed. As the transformation is linear, one can use any calibrant to do the transformation in a much simpler way (similarly to what is done for a DMA). For example, one can use the reference of THA^+ which appears at $t_{ref} = 46.51ms$ with a mobility of $Z_{ref} = 0.972cm^2/Vs$ such that:

$$Z = \frac{Z_{ref} * t_{ref}}{t}$$

(3.20)

Eq. (3.20) readily yields the mobility of every point in our system. In order to calculate the Collision Cross Section (CCS) Ω and mobility diameter of the ions, the Mason-Schamp equation is used [53]:

$$Z = \frac{3}{16}\frac{q}{\rho_{gas}}(1 + \frac{m_{gas}}{M_w})^{1/2}\sqrt{\frac{2\pi m_{gas}}{k_bT}}\frac{1}{\Omega}$$

(3.21)

where ρ_{gas} is the density of the gas ($1.225kg/m^3$), M_w is the molecular weight of the ion and m_{gas} is the molecular mass of the gas (28.96 Da for air). The mobility diameter can then be obtained by assuming that the CCS corresponds to a spherical ion. To facilitate the transformation, the term $(1 + \frac{m_{gas}}{M_w})^{1/2}$ in eq. (3.21) has been absorbed into Ω (making it $\Omega_r = \Omega(1 + \frac{m_{gas}}{M_w})^{-1/2}$). In such case, then the Stokes-Millikan equation agrees with eq. (3.21) as long as $\Omega_r = \frac{1.36\pi}{4}(d_z)^2$. It is then quite simple to calculate the mobility diameter of the ions once the mobility is known (assuming the ions are singly charged). Fig. 3.5 provides the corresponding diameter of the ions present.

To show that the transformation is indeed linear and therefore accurate when the correct reference is used, a possibility is to compare experimentally and numerically inferred mobil-
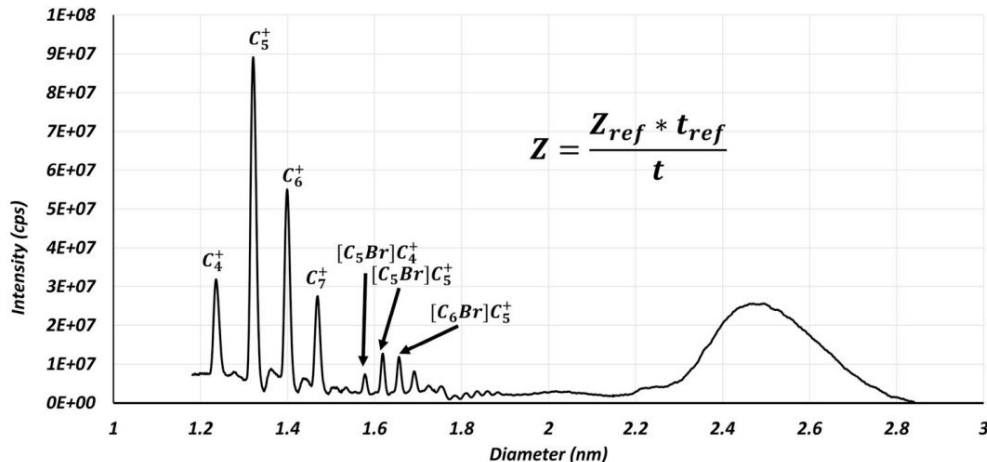
Figure 3.5. Transformation of arrival time distribution into mobility diameter for the Data in Fig. 3.4.

ity diameter ratios of two candidate structures. The two structures chosen were tetrabutyl (TBA) and tetraheptylammonium (THA) salts with an experimental mobility diameter ratio of $1.47/1.236 = 1.189$. These salts are very flexible due to the long alkyl branches and one single structure is insufficient to correctly calculate CCS that are comparable to the experimental one. For such reason salts were then modeled, minimized and Molecular Dynamics were run for 100 ps 7 and 17 different times for the TBA and THA respectively (Chem 3D v. 18.0) yielding differing structures each trial. The numerical CCS, and hence the mobility diameter, were calculated using the software IMoS v.1.10 averaging over all CCS obtained for each salt [24], [25]. As proven in a different manuscript, the structures produced by MD are oversized and must be reduced to get accurate CCS. For a 91% diffuse, 9% elastic accommodation with ion-induced dipole calculation, a reduction of 30% seems to yield the most accurate CCS values. The ratios when no reduction is present, for a 19% reduction and for a 30% reduction are 1.212, 1.19, 1.182 respectively which are acceptable values when compared to the experimental counterpart.

In order to test the capability of the instrument and the theoretically inferred resolution, a set of experiments were also completed testing signal intensity and resolution as a function of pulsing time and voltage. Fig. 3.6 shows the effect of the reduction of the pulse time on the dimer peaks for a fixed voltage of $7kV$. As the pulse time is reduced, the signal decreases
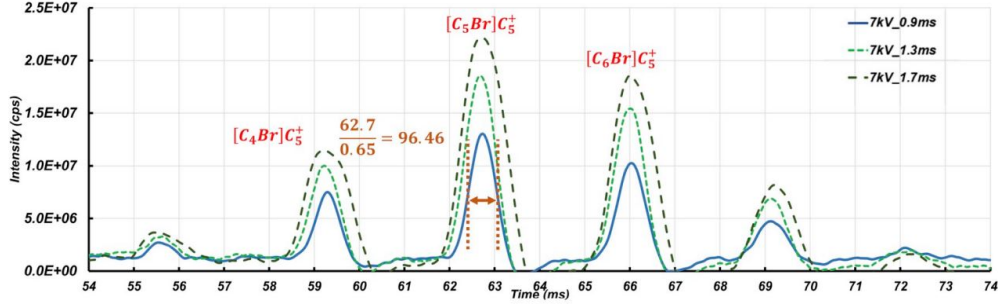
Figure 3.6. Intensity as a function of arrival time distribution for a set of dimers obtained at the same initial voltage and varying the pulsing time. As the pulsing time is decreased, the signal lower but the resolution increases.

and the resolution increases. For a pulse of 0.9 ms, the resolution acquired was 96. If the width at half maximum of the peak is measured for a 0.9 ms pulse, it is around 0.7 ms, which is smaller than the initial width of the peak which seems to suggest that the autocorrection effect is present. Note that for a regular DT, the width of the peak could never be smaller than the initial peak width. The pulsing time can be reduced even further and resolutions of 120 have been achieved but not shown as the loss in signal outweighs the improvement in resolution. For this particular experiment, a pulse below $200\mu s$ would lead to a complete loss of signal so clearly an improvement of the gates or centering of the initial ion package has to be pursued before a smaller pulse is used and the highest achievable resolution tested.
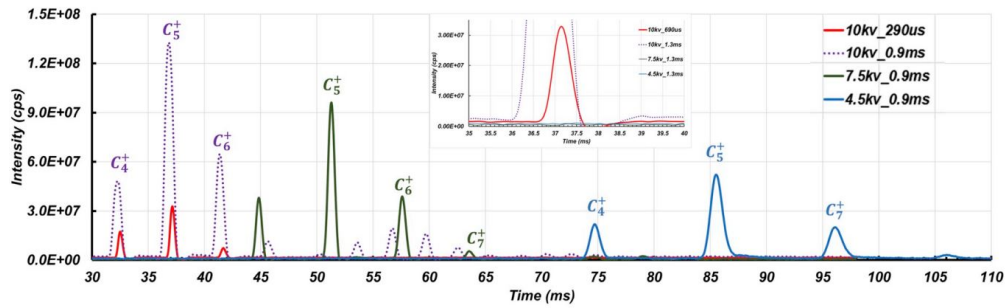
Figure 3.7. Intensity as a function of arrival time distribution for a set of monomers for the same pulsing time but different initial voltages. The lowest resolution happens to be that of the highest voltage. A reduction of the pulsing time increases the resolution for the largest voltage as expected.

Fig. 3.7 studies the resolution and intensity as a function of voltage for a pulse time of 0.9 ms. Similar overall intensity is observed for all voltage. Although the highest count is observed for the highest voltage, peaks widen as the voltage decreases. Despite this, the resolutions calculated for the tetrahexylammonium salt monomer are 57.1, 84.1 and 80.125 for $10kV$, $7.5kV$ and $4.5kV$ respectively. The fact that the highest resolution does not occur for the highest voltage (as would be expected from a source point distribution in a DT) is already very forth-telling that our theoretical studies are sound. Looking at Fig. 3.3 (B), it nonetheless seems to suggest that the highest resolution should have appeared for $7kV$, followed closely by $4.5kV$ and the finally for $10kV$ which is exactly the case experimentally. While theoretical results seem to agree with what is experimentally observed in this case, it is true that 2 dimensional effects weigh more than theoretically expected for the longer residence times as can be observed by the tail forming at $4.5kV$. It is also true that the effective experimental pulse times are perhaps different than the ones we inferred directly from the wave generator. It is clear, however, that there is a maximum in the resolution that depends on the voltage and pulsing times used. To show that the results are indeed qualitatively correct, we reduced the pulse time to $290\mu s$ for $10kV$ and the resolution increases to 83 in line with what is expected for a reduction of the pulse.

To fully study the effect of autocorrection on the VFDT, a reasonable experiment would be to compare a constant field DT and the VFDT with a similar overall arrival time using the same pulse time. The results are shown in Fig. 3.8, where the fields were adjusted so that the arrival times were as close as possible for two different pulse times, 900 and $600\mu s$. The two pulse times were calculated using the same exact field inside the three-grid region. The top of Fig. 3.8 first shows the arrival time distribution of several dimers using the $900\mu s$ pulse. The bottom follows with two plots focusing on the $[C_5Br]C_5^+$ peak and different pulses. To make the comparison a little bit clearer, the peaks were normalized in the figure and slightly shifted ($< 0.2ms$) so that the beginning of the $[C_5Br]C_5^+$ peaks was on top of each other. If the plots were not normalized, the constant field DT had approximately 10% more signal overall probably due to off centering of the initial ions. Given that the arrival drift velocity of the ions is approximately the same, albeit slightly higher for the DT, the fact that the peak width is narrower for the VFDT confirms that autocorrection must be
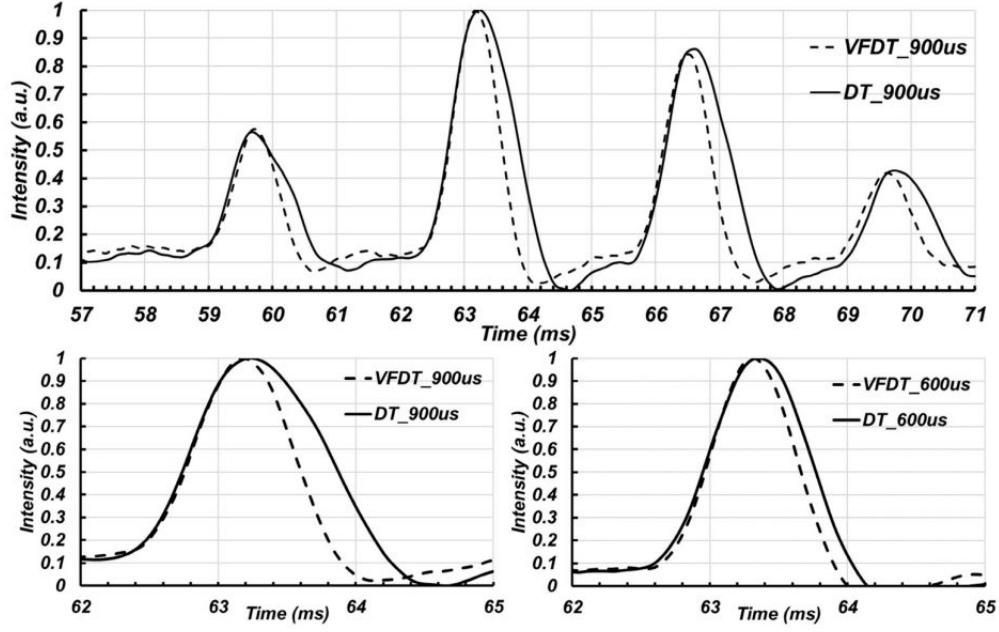
Figure 3.8. Normalized intensity as a function of arrival time distribution a set of dimer peaks for different pulsing times and two instruments; a constant field Drift Tube and the VFDT. Top) Set of dimer peaks for $900\mu s$. Bottom Left) Close-up of peak $[C_5Br]C_5^+$ taken from above. Bottom Right) Close-up of peak $[C_5Br]C_5^+$ taken for a pulse time of $600\mu s$.

present. A quick calculation suggests that in this particular case, an increase of $20-30\%$ in the resolution is present thanks to the incorporation of the varying field.

4. ENHANCING SEPARATION AND CONSTRICTION OF ION MOBILITY DISTRIBUTIONS IN DRIFT TUBES AT ATMOSPHERIC PRESSURE USING VARYING FIELDS

This section is from a published manuscript of the author of this dissertation from ref. [3]. Author Xi Chen has contributed to the methodology, design of the experiment, data analysis and writing of the original draft. Author Dr. Carlos Larriba-Andaluz (the corresponding author) has contributed to the theoretical calculation, review and edition of the manuscript. Author Mohsen Latif has contributed to the data analysis and review of the manuscript. Author Viraj Gandhi, Xuemeng Chen, Leyan Hua and Dr. Nobuhiko Fukushima have contributed to the review of the manuscript.

4.1 Overview

Ion mobility spectrometry (IMS) is an effective and well-established technology for the detection and identification of ions in the gas phase. In traditional IMS, particles are separated under the influence of a homogeneous electric field through a buffer gas environment according to their individual mobilities, which is related to the size, shape, charge, and the collision cross section (CCS) of the ions. The characteristics of IMS instruments, like fast response (in microsecond), excellent detection limit (at ppb levels), low cost and high sensitivity [113], made it widely applicable for analytical chemistry [95]. In recent decades, the increasing interest has led to thorough research that has been dedicated to combine IMS with mass spectrometry (MS) [114], [115]. IMS-MS is unique at providing a second dimension of separation, which is beneficial to characterize and identify the structure of isomers and improves the capability of the system to analyze and quantify the compounds in complicated mixtures.

The conventional Drift Tube systems have a simple working principle. A nearly uniform electric field is introduced by a series of stacked ring electrodes, and a swarm of ions in the drift region are propagated by the combination of electrical field and the drag force of the buffer gas yielding an equilibrium velocity, normally referred to as the drift velocity. The

distribution of the analyte ion is measured when the ions reach a detector and is given as an arrival time distribution (ATD). In recent decades, much work had been done by researchers to improve the implementation of the DTIMS instruments. To improve the simplicity and portability, a number of nontraditional materials have been investigated for its construction, including resistive glass [116]–[118], printed circuit boards [119] and 3D printed IMS [107]. Besides, inverse ion mobility spectrometry [120] and flowing atmospheric-pressure afterglow (FAPA) technology [121] were used to improve the transmission. Compared with congeneric products, for example, Differential Mobility Analyzer (DMA) [33], [34], the prominent features of simplicity, faster scanning and relatively higher resolution of a DT system, make it a practical consideration also in aerosol science [57], [106], [107]. The DT does suffer some deficiencies such as that of low transmission (due to the duty cycle) and limited measurement range to a few nanometers in diameter [28], [54].

With the development of IMS, there has been an increasing need to improve its resolution and sensitivity, a set of criteria used to evaluate the importance of drift versus diffusion of the ions in the separation process. In the axial direction, the resolution of the DTIMS can be defined in either length scale or time scale [53]:

$$R_{DT} = \frac{\overline{z}}{\Delta z} = \frac{t}{\Delta t_{FWHM}} = \frac{1}{\sqrt{\frac{t_{pulse}^2}{t^2} + \frac{16 k_b T \ln 2}{qEL}}} \tag{4.1}$$

where $\overline{z}$ is the length of the drift region, Δz is the width of ion distribution in the axial direction, t is the drift time to the detector and Δt_{FWHM} is the full width at half maximum of the temporal distribution, q is the charge, L is the length of the drift region, E is a constant electric field, k_b is the Boltzmann constant, T is the temperature. In the eq., t_{pulse} is the initial pulse time due to the time required to traverse the gate. Given eq. (4.1), there are a few possibilities that may increase the resolution of the system. One would be increasing the electric field or the length of the instrument. The first of such choices has the breakdown limitation, while the latter is somewhat restricted, in particular at atmospheric pressure due to losses through diffusion. Another option is to decrease the temperature but maintaining a low temperature system is costly. A final possibility is to decrease the pulse time, lowering the overall transmission.

A second alternative to increase resolution and sensitivity in the DTIMS is to modify the electric field present in the system. This can be done in the radial direction, to improve transmission and sensitivity, and in the axial direction, to increase resolution. In the radial direction, the constriction of ions has been exclusively done using radio frequency (RF) technology at low pressure, which confines the ions in a central region and increases the transmission of the system. This has been ubiquitously applied commercially in systems such as Lossless Ion Manipulation (SLIM) [108], [109], Trapped Ion Mobility Spectrometers (TIMS) [62], T-Wave, and partially or fully in long Drift Tube Ion Mobility Spectrometry (DTIMS) combined with ion funnels [28], [122]. RF technology cannot be implemented at atmospheric pressure due to the requirement of high electric field and frequency.

In the axial direction, there have been recent attempts at diffusion correction. Non constant fields may be used to correct diffusion in the axial direction, and there is almost no limitation on the working pressures. It has been widely used on TIMS systems (by trapping the ions) and in Drift Tube (DT) systems, such as the Inverted Drift Tube (IDT) [1], [2] and the Varying Field Drift Tube (VFDT) [94]. The VFDT is an atmospheric pressure instrument that employs a linearly decreasing electric field. The decreasing field constrains the ions in the axial direction by how the ion's mobility interacts with the field. For a distribution of ions that are at an equilibrium point, ions that diffuse upstream, will be pushed forward due to the increase in the field and ions that diffuse downstream, will be pushed backwards due to the decrease in the observed field. The VFDT can also correct the initial distribution, improving sensitivity for the same initial pulse. The VFDT has been shown to have theoretical spatial resolutions that are significantly higher than regular DTIMS under similar considerations. When the instrument was tried experimentally, its temporal resolution was only marginally higher than that of the DTIMS.

In this work, we show that the spatial resolution in the VFDT is different from its temporal counterpart due to the large disparity in drift velocities at the beginning and at the end of the drift tube which is seen to be the cause for loss in expected performance. In particular, the slow drift velocity at the end of the tube (due to the decreasing electric field) is detrimental. To increase this drift velocity and hence increase the resolution, a high voltage pulse is employed at a properly adjusted time to provide a high uniform electric field for

the second portion of the tube. The new system is termed HVP-VFDT. The HVP-VFDT benefits from the diffusion constriction as well as the high temporal resolution. We have tested this combination experimentally and numerically, showing experimental resolutions of over 240 on atmospheric pressure drift tubes of 18cm, an unprecedented accomplishment. We also show that the chromatographic resolving power is very high and can improve peak capacity over that of a regular drift tube.

4.2 Experimental Setup

4.2.1 HVP-VFDT Construction

The construction of the HVP-VFDT is mainly based on the conventional Drift Tube from Kanomax (Osaka, Japan) and its complete design is described elsewhere and will only be described briefly here [94]. As depicted in Figure 4.1(a), the drift region is separated from the ionization region by three metallic grids (red color dotted lines). The improvement in this work consists of two parts: an initial Linear Field (LF) Region (from 42 to 157 mm) and a High Field Pulsing (HFP) Region (from 157 to 255 mm). In the LF region, a series of resistors of different resistance were connected to the electrodes, and a HV power supply (EMCO HV, Now Spellman, E121) was applied to generate a linearly decreasing electric filed in the axial direction, where diffusion auto-correction helps constrict ions from diffusion in the axial direction and narrow the ion distributions. In the HFP region, the electrodes were connected by a series of resistors with the identical resistance, which would produce a nearly uniform electric field in the axial direction. The voltage in this region was controlled by a HV Behlke pulser (HTS 111-03-GSM, Germany), offering a high voltage square wave by means of a Siglent wave generator (Model SDG 2042 X, OH, USA), and the signal is synchronized with the pulser time at the gate. The high voltage is adjustable to pulse at a specific time t_{HVP}, when the ions of interest come inside the HFP region, as shown in Figure 4.1(b). Figure 4.1(c) shows the corresponding electric field inside both the LF and HFP regions before and after the pulse. When $t < t_{HVP}$ (purple solid line), the increase in the electric field followed by a sharp decrease is due to a large voltage difference between two close electrodes (e.g., change from $2.2kV$ to $1kV$) in the conjunction area of the two

88

regions. While this could be avoided, it is used to constrict the ions in the radial direction right before the large pulse, increasing sensitivity. Once the HVP occurs, $t > t_{HVP}$ (red dashed line), ions that have passed the axial position of the start HFP region will arrive at the detector, while those before will be lost. The radial electrical field introduced from the HVP will once again constrict the ions in the radial direction.

4.2.2 Chemicals and Reagents

Tetraalkylammonium bromide salts were purchased from Sigma (Sigma Aldrich, MO, USA) including tetrabutylammonium bromide (TBA, C_4), tetrapentylammonium bromide (TPA, C_5), tetrahexylammonium bromide (TXA, C_6) and tetraheptylammonium bromide (THA, C_7). These salts were mixed at $5mM$, $15mM$, $7mM$ and $7mM$ respectively in $50 : 50$ Methanol and H_2O solution. The analytes were pushed in to the ionization region through a silica capillary (ID: $40\mu m$, OD: $360\mu m$, Polymicro Technologies) and Electrospray Ionization (ESI) method was applied at the tip.

4.3 Results and Discussion

4.3.1 Theoretical discussion of the secondary pulse

In our previous work describing the VFDT, the Nernst-Planck equation was solved for the linear region [2], [94]. In it, we assumed that a linearly decreasing field $E = A(L_E - z)$ was present, where A is the slope of the field, $L_E > L$ is the distance at which the field would become zero, being L the length of the drift region. The full derivation of the ion distribution has been added to the supplementary information here as well. The result for the spatial resolution for the linear varying field portion of the system was given as:

$$R_{VFDT_z} = \frac{\overline{z}}{\Delta z} = \frac{L}{L_E}\sqrt{\frac{qL_E E_{max}}{8k_b T \ln 2}} \frac{1 - \mathrm{e}^{-KAt}}{\sqrt{1 - c_{z\sigma}\mathrm{e}^{-2KAt}}} \tag{4.2}$$

$$R_{VFDT_z} = \sqrt{\frac{qL_E E_{max}}{8k_b T \ln 2}} \frac{(L/L_E)^2}{\sqrt{1 - c_{z\sigma}(1 - 2L/L_E + (L/L_E)^2)}} \tag{4.3}$$

Here, q is the charge, $E_{max} = AL_E$ is the maximum electric field at the beginning of the linear field region. K is the mobility of the ion of interest, t is the arrival time, k_b is the Boltzmann constant, T is the temperature, and $-\infty < c_{z\sigma} \leq 1$ is a constant so that $\frac{(k_b T)}{qA}(1 - c_{z\sigma})$ is the square of the standard deviation of the initial distribution. The overall spatial resolution is significantly higher than that of a constant electric field drift tube and spatial resolutions higher than 200 under regular operation were expected theoretically [94]. The experimental results did show a slightly higher resolution than that of the regular Drift Tube but the results were not as high as expected.

The reason behind this difference stems from the fact that the spatial resolution in the VFDT is quite different from the time resolution observed experimentally. The change in eq.(4.2) and (4.3) from average position $\bar{z}$ to average arrival time t is given through the average drift velocity $\bar{v}_d$ as $\bar{z} = \bar{v}_d t$. On the other hand, the drift velocity at the end of the VFDT is much smaller than the average. So when transforming $\frac{\bar{z}}{\Delta z}$ into $\frac{t}{\Delta t}$, the conversion requires:

$$\frac{\bar{z}}{\Delta z} = \frac{\bar{v}_d t}{v_{df} \Delta t} \tag{4.4}$$

where v_{df} is the final drift velocity. This is not the case for a regular constant field DT where $\bar{v}_d$ and v_{df} are the same. As such, when changing from space resolution to time resolution, the difference in spatial resolution between DT and VFDT is reduced by the factor $\frac{\bar{v}_d}{v_{df}}$ when changed to temporal resolution, a factor which could be quite significant. Therefore, the resolution in time for the VFDT $R_{VFDT_t} = v_{df}/\bar{v}_d R_{VFDT_z}$. Figure 4.2 is used here to illustrate the idea.

To circumvent this problem, and take advantage of the spatial resolution, one must try to increase the final drift velocity of the ion. However, it has to be done so that the benefit of the autocorrection remains. One particular option is by means of a delayed high voltage pulse increasing the constant electric field in the last portion of the tube. This new method has the full advantage of the diffusion autocorrection of the VFDT but does not suffer from the loss of resolution when changing from spatial to time resolution, in particular if a final drift velocity is used that would be higher than the expected average.

4.3.2 Simulation results of the HFP-VFDT

Given the results from previous work and the theoretical discussion above, one can attempt to test the viability of the high voltage pulse [2], [94]. The SIMION software (version 8.1.1.32, Scientific Instrument Services, Ringoes, NJ) was used to simulate the ion distribution under the influence of the combination of the electric fields presented in Figure 4.1. The Drift Tube model dimensions constructed for the simulation are the same as those of the experimental set up and the tetraalkylammonium bromides salts, C_4^+ (black), C_5^+ (red), C_6^+ (blue) and C_7^+ (green) were mimicked as singly charged spherical ions with equivalent mobility to the experimental counterpart. In the simulation, a statistical diffusion simulation (SDS) collision model was implemented to simulate the interactions between the ions and the background gas molecules at the standard environment conditions ($1atm$, $293K$).

Figure 4.3(a) shows the simulation domain and results of ion distributions at the initial position t_0 as well as at four different instances in time. Initially, the ions with different mobilities are mixed inside a limited area after the 3rd grid, and they are accelerated by the linearly decreasing electric field inside the LF Region. Similar to the case of uniform electric field, higher mobility ions travel faster than their lower mobility counterparts separating the ions, as showed at time t_1. At time $t_2 < t_{HVP}$, the ions pass through the sharp field peak area of the system (middle of the purple curve in Figure 4.1(c)). The first portion accelerates the ion distributions causing the opposite effect of axial constriction and broadening the ion distributions. After the increase, the drop in field once again constricts the ions in the axial direction. In Figure 4.3(a), at t_2, C_4^+ (black) is already past the raise in the field, while C_5^+ (red) is in the rising portion and C_6^+ (blue) and C_7^+ (green) are starting the rising portion (see Figure 4.1(c) for approximate locations). The fast decrease of the field after the raise, narrows the ion's distributions substantially, and the ion distribution becomes axially narrower than the initial distribution (something that cannot be accomplished with a constant field drift tube). When $t > t_{HVP}$, a high electric field is generated inside the HFP region, increasing the total drift velocity of the ions. Time t_3 is right after t_{HVP}, where the distributions can be observed to be quite narrow. While the autocorrection effect is no longer present, the ions now have a drift velocity that is high enough that the temporal

distribution may be narrower than its spatial counterpart if the drift velocity of the HFP region is higher than the average velocity. The spatial distribution right before the arrival to the detector is given at t_4. A zoom in of the distributions for C_5^+ is provided in Figure 4.3(b), to exemplify the process.

To study the ion radial movement in the middle section, the effect of the field peak area and of the HFP, the electric fields in the radial direction are plotted in Figure 4.4. The voltage on the electrodes in the LF region are fixed ranging from $4.5kv$ to $2.2kv$ (from 42mm to 145mm). When $t < t_{HVP}$, a low voltage of $1kV$ is applied at the electrode where the pulsing will occur and that establishes the separation between the LF and the HFP region (157mm). The radial electric field after 135mm before pulsing is depicted in Figure 4.4 (a). It is almost zero in the center of the tube. In the region from $2.2kV$ to $1kV$, the sharp increase in the field in the axial direction, pulls the ions inward in the radial due to the solenoidal aspect of the field ($\nabla \cdot \overrightarrow{E} = 0$). This is followed by a decrease in the axial field which has the opposite effect and extends the ions outwards radially while having a constricting effect in the axial direction. The radial field agrees with what is observed in the SIMION simulation, at times t_2 and t_3.

When $t > t_{HVP}$, a high pulsing voltage of $7kV$ is applied to the electrode at the beginning of the HFP region (157mm) and a linear voltage drop affects the ions that have entered the HFP region. The radial electric field for this region is shown in Figure 4.4(b). Since the voltage prior to the $7kV$ electrode is smaller ($2.2kV$), the initial portion of the field region does not correspond to a constant electric field but an increasing axial field. As such, the radial field has a constricting effect on the ions in that region. However, the field becomes constant after the constriction and most of the ions are subject to negligible radial electric fields in the HFP region and a constant electrical field in the axial direction. The initial constricting effect in the radial direction may be used to our advantage if necessary to increase the sensitivity of the instrument.

4.3.3 Experimental results and discussion

To test the performance of the system with the VFDT-HFP region, a series of experiments have been conducted. When the ions of interest move into the HFP region, a high pulsing electric field is applied in after the linearly decreasing electric field to increase the drift velocity and narrow the arriving time distribution. The signal intensity and resolution were studied as a function of pulsing start time and voltage, which are the main factors that affect the final signal. The initial voltage at the pulsing electrode was also modified to check its effect on the total resolution. To fairly compare the different results below, the initial gate was opened for $390\mu s$ for all the experiments which should provide the similar initial distributions for all cases. Note that reducing the initial gate would allow us to improve the resolution of the instrument even further if necessary.

In principle, one would expect that a higher pulsing voltage would normally yield a higher resolution. However, the fact that the initial axial field is not flat after the pulse in the HVP region has played an important role in the overall resolution, and there is a balance between arrive time and time distribution of ions. This could be fixed by using a higher voltage pulse and applying a higher voltage at an electrode which is closer to the gate, but it was not pursued here due to voltage limitations of the pulser. To observe the effect of the pulse voltage on the resolution, Figure 4.5 shows the voltage changing from $3kV - 6kV$ and produced at $t_{HVP} = 55ms$ after the closing of the gate. The electrode used for pulsing (157mm) is kept at $0.7kV$ prior to the pulse. Figure 4.5 (a) shows the intensity of the peaks $(C_4^+, C_5^+, C_6^+$ and $C_7^+)$ as a function of the arrival time for high pulsing voltages of $3kV$, $4kV$, $5kV$ and $6kV$, respectively. As the high pulsing voltage increases, the final drift velocity of ions increases while the arriving time of all the ions inside the HFP region is reduced. The effect is more noticeable for the lower mobility ions as they are subject to the high field for a longer period of time. Figure 4.5(b) shows the calculated resolution of all four monomers at different high pulsing voltages. The resolution increases with the voltage initially as is expected but seems to start flattening. The lower resolution of the C_7^+ peak maybe due to two possibilities, the first related to the effect of the initial portion increasing field in the HFP region, which becomes larger with increasing pulsing voltage, and affects the low

mobility ions, and the second related to the low intensity and asymmetry of the peak. In all, it seems like the optimal high pulsing voltage found here is around $6kV$ with resolutions for all of the monomers over 170 and reaching close to 200. However, given that the distance between peaks is reduced as the voltage is increased, it is possible that the chromatographic resolving power has a different optimal voltage that is more suited for peak capacity. The chromatographic resolving power may be defined as:

$$R_p = \frac{t_{peak2} - t_{peak1}}{0.5(\Delta t_1 + \Delta t_2)} - 1 \tag{4.5}$$

And it is shown in figure 4.5(a) for peaks 1 and 2. While the resolving power is quite good for all cases, it seems that $5kV$ is the best compromise between resolution and resolving power.

To test how the distributions vary due to the initial voltage applied on the pulsing electrode (157mm), Figure 4.6 shows the intensity of distribution as a function of arrival time for different initial voltages with a fixed pulsing voltage of $5kV$ at $t_{HVP} = 55ms$. In Figure 4.6 (a)-(e), the intensities of the peaks (C_4^+, C_5^+, C_6^+ and C_7^+) are shown for an initial voltage of $2kV$, $1.7kV$, $1.3kV$, $1kV$ and $0.7kV$, respectively. Note that the field after the pulse remains unchanged so the difference in results can be attributed to the speed, position, and width of the initial distribution before the pulse. For example, the case at $2kV$ does not have a large increase in the field initially (drop from $2.2kV$ to $2kV$) and ions move with the highest initial drift velocity, but it is also the one with the initial largest initial separation. This separation causes the lower ion mobility ions to be in the ramping portion of the field after the pulse causing further separation as well as slightly lower resolution. The $1.7kV$ case is somewhat similar. The lower voltage cases, $0.7kV - 1.3kV$, cause a spike in the electric field a lower electric field before the pulse (after 157mm), which in turn makes the initial speed of the ions slower but due to the strong final autocorrection makes the peaks narrower. Figure 4.6 (f) shows the resolution of the monomers at different initial voltages as well as the resolving power. At $0.7kV$, the resolution of the peaks ranges from 200 to 240. However, the best resolving power occurs for the $2kV$ case which still has resolutions of 160 (not considering the C_7^+ peak due to its variability).

The resolution and intensity of the signal are also affected by the pulsing time t_{HVP}, as shown in Figure 4.7. Here, the pulsing high and low voltage are fixed at $5kV$ and $0.7kV$, respectively, and the pulsing start time is decreased from 75ms to 51ms. Figure 4.7 (a) shows the signal intensity as a function of the arriving time with pulsing start time at 75ms, 68ms, 59ms, 51ms (in Figures 4.5 and 4.6) and 51ms respectively. The initial pulsing time affects how long the ions remain under the high field as well as what is the lowest and highest mobility ion that can be studied. For example, for a pulse starting at $t_{HVP} = 75ms$, which is very close to the arrival time of the C_4^+ monomer without any pulsing. This affects the overall resolution of the C_4^+ monomer but keeps the resolution of the other monomers over 220. Since the pulse occurs late, it also allows dimers to penetrate the pulsing region and may be observed. As the pulse starting time is decreased, the dimers start to disappear, and the total arrival time is reduced due to the high field. At a starting pulse time of 51ms, the C_7^+ monomer position is around the pulsing electrode (157mm) and suffers from a non-constant increasing field which broadens the distribution and lowers its resolution. One can see that the pulse starting time does not heavily affect the resolution as long as the ions are contained within the constant field section when the pulse occurs. This is because the effect of the pulsing time is only meant to improve the temporal resolution by increasing the final drift velocity. The higher electric field does increase the resolution but only at the cost of losing the constriction of the ions in the axial direction. The overall resolving power also stays rather constant but decreases as the pulsing starting time increases. The large drop for 76ms is only attributed to the broadening of the first peak.

To show the importance of the HVP on the resolution, one can attempt to pulse after the first monomer has arrived at the detector. Figure 4.8 shows a case with a pulsing start time of 83ms with high & low pulsing voltage of $5kv$ and $0.7kv$. The higher low pulsing voltage (versus $0.7kV$ in Figure 4.7) allows the ions to arrive earlier to the detector and hence 70ms is sufficient for the C_4^+ monomer to fully reach the detector. One can easily see the effect that the HVP has on the temporal resolution of the system. This can also be used to confirm the theory of varying linear field autocorrection.
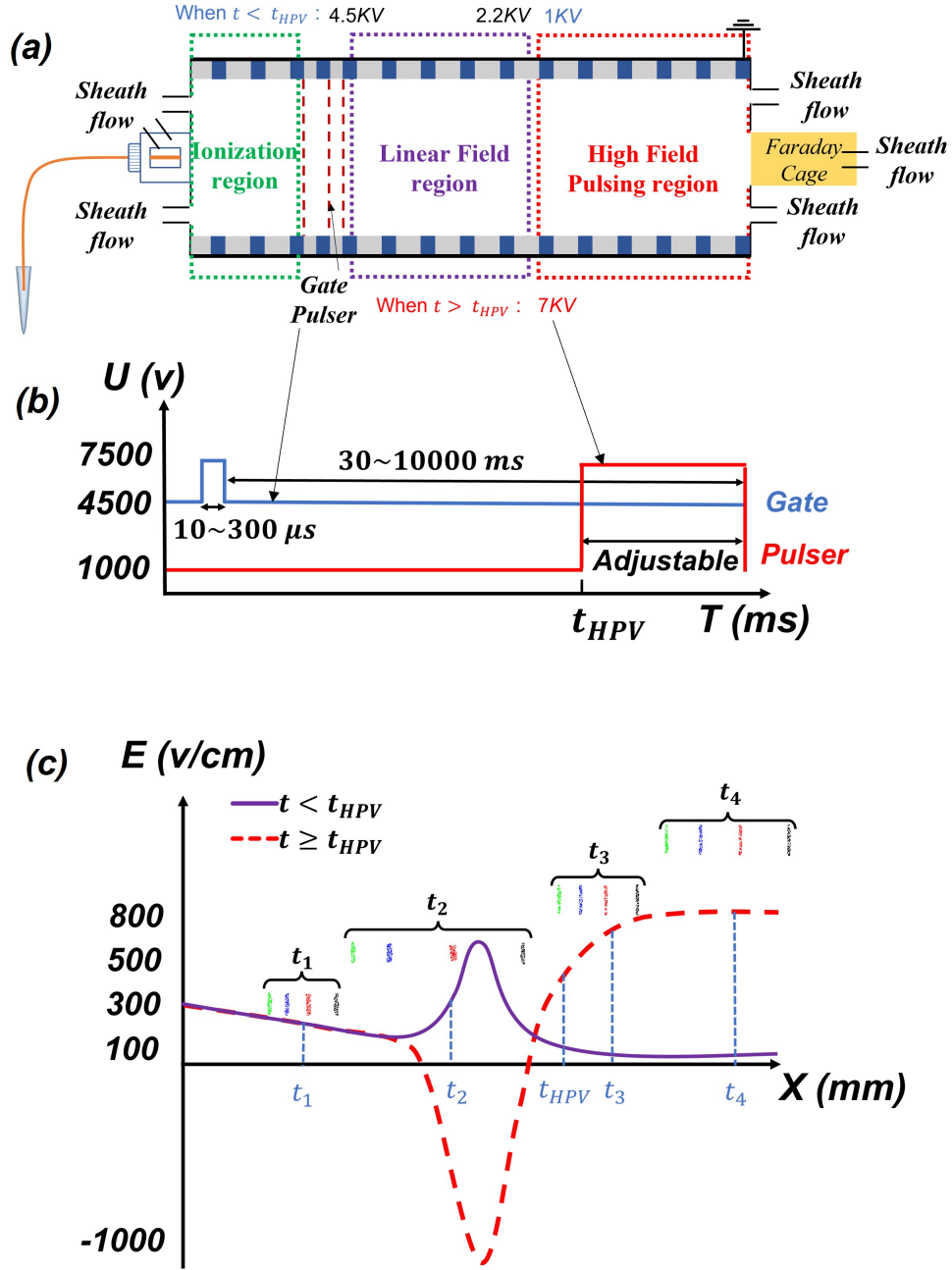
Figure 4.1. (a)Experimental sketch of the HVP-VFDT with electrospray ionization source. (b) The pulser time and voltage on the gate and the high field pulsing region, the pulser time t_0 is synchronized with the gate and is adjustable to pulse when the interested ions pass through into this region. (c) Electric field inside the drift tube at different time range.
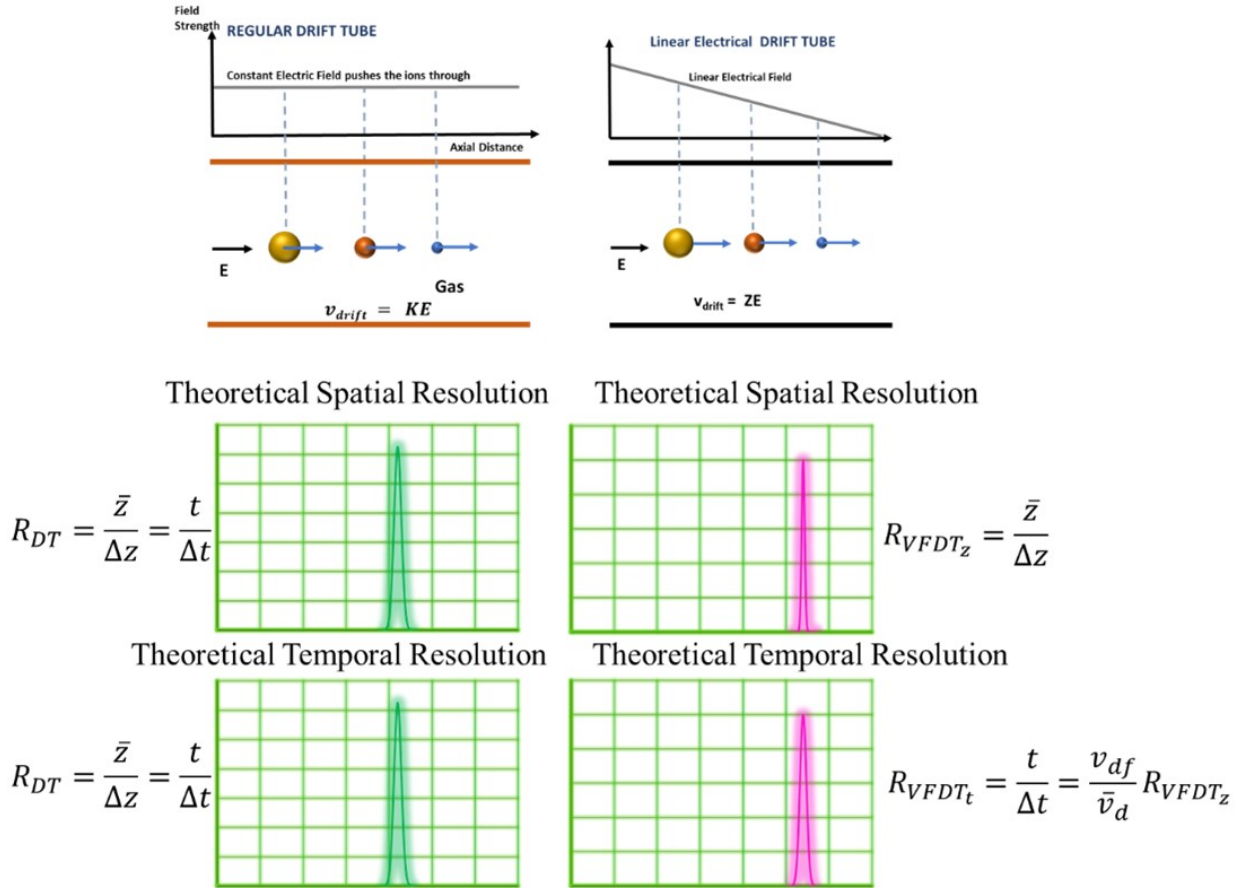
Figure 4.2. Comparison between spatial and temporal resolutions for the constant field and varying field cases
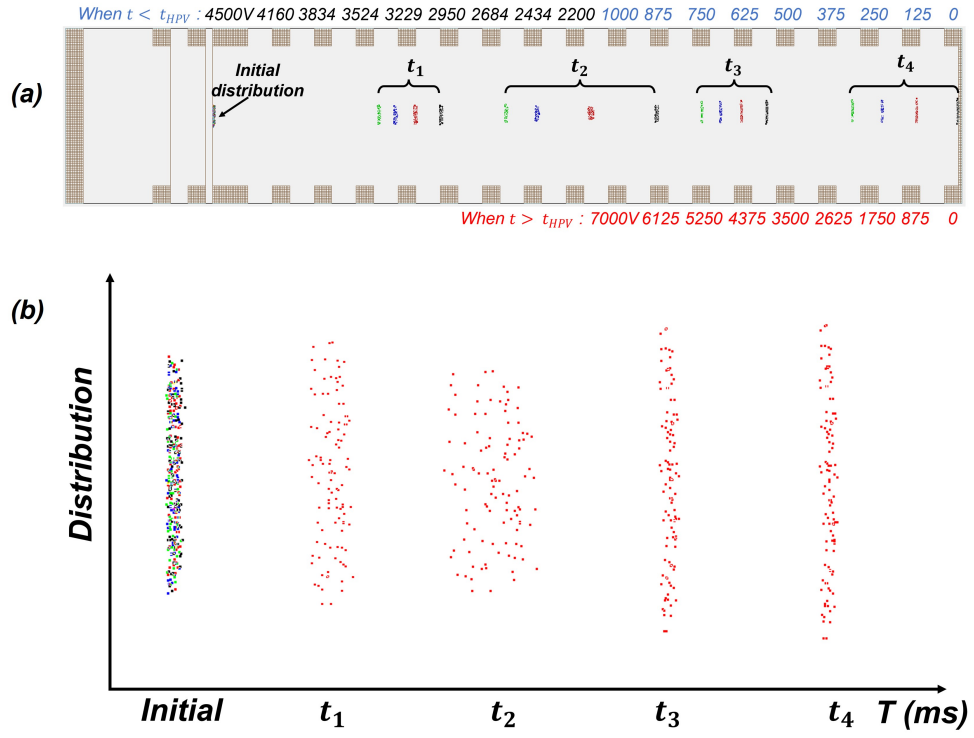
Figure 4.3. (a) Simulation results of ion distribution at initial position and different time. (b) zoomed in distribution of C_5^+ at the corresponding time.
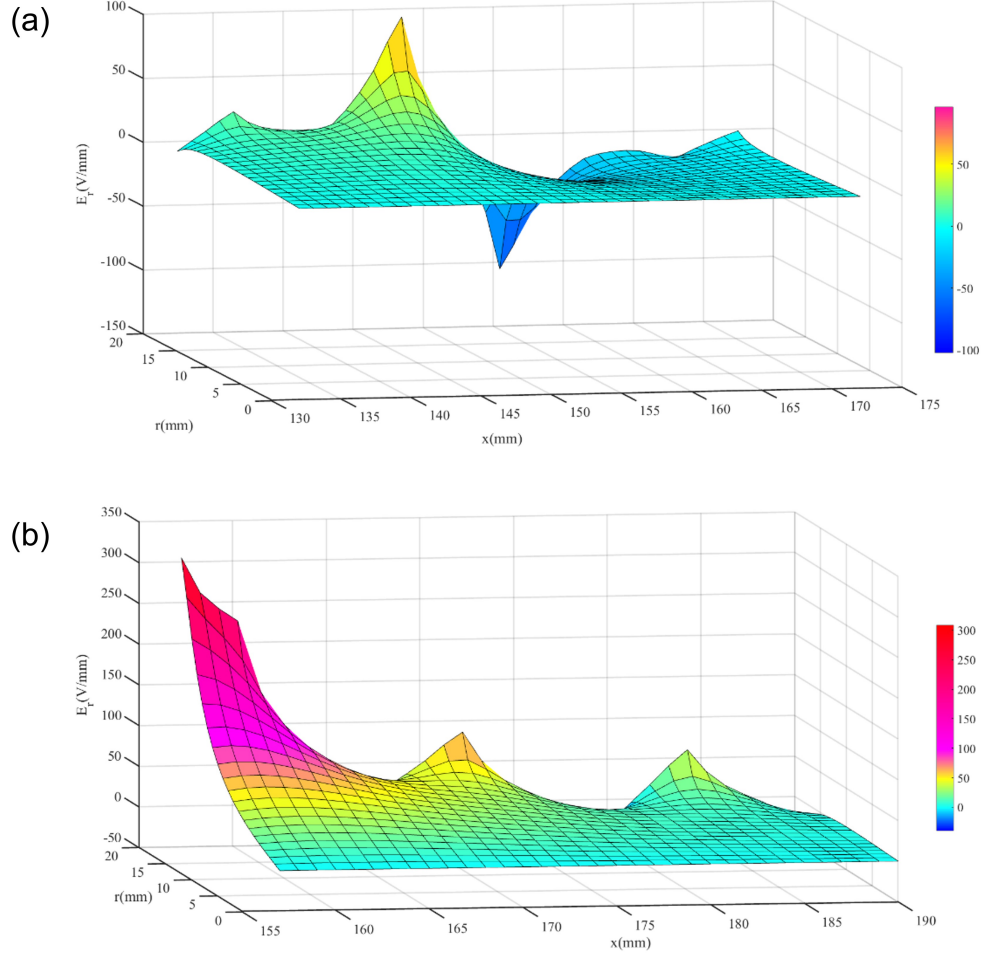
Figure 4.4. Electric field in the radial direction of the conjunction area inside the drift tube. X axis is in the axial direction of the drift tube while y axis is in the radial direction. Since the construction of the DT is symmetric, we built half of it and rotated the y axis to get the whole construction and the coordinate in this direction is from $-20mm$ to $20mm$. (a) electric field when $t < t_{HVP}$, (b) electric field when $t > t_{HVP}$.
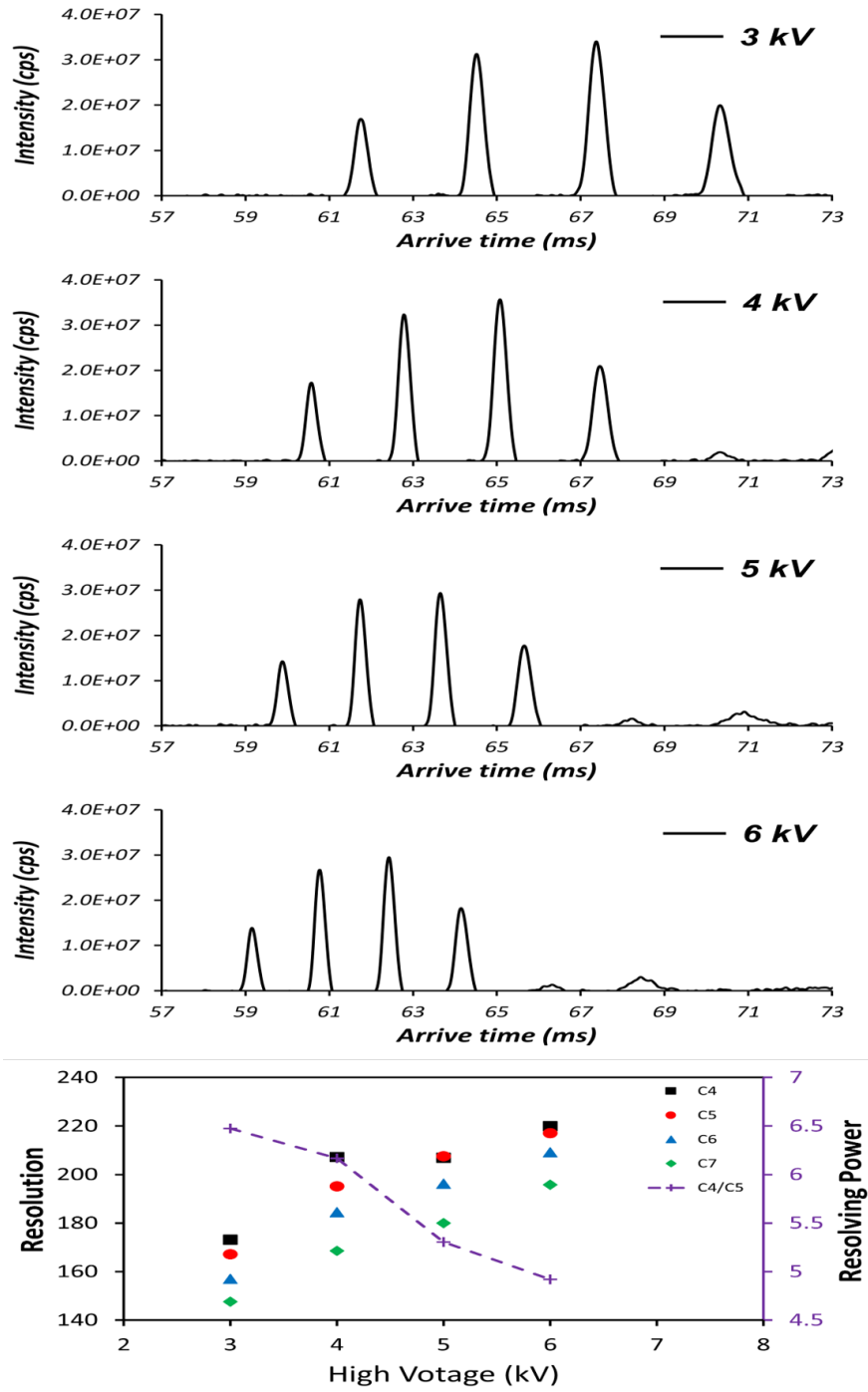
Figure 4.5. Fixing the low pulsing voltage to $0.7kV$ and pulsing start time to 55ms, adjusting the high pulsing voltage from $3kV$ to $6kV$. (a). The peaks' intensity as a function of arrive time with high pulsing voltage at $3kV$, $4kV$, $5kV$ and $6kV$, respectively. (b). Resolution of the monomers (C_4^+, C_5^+, C_6^+ and C_7^+) as a function of high pulsing voltage. The right y-axis shows the resolution as a function of the voltage (purple dashed line).
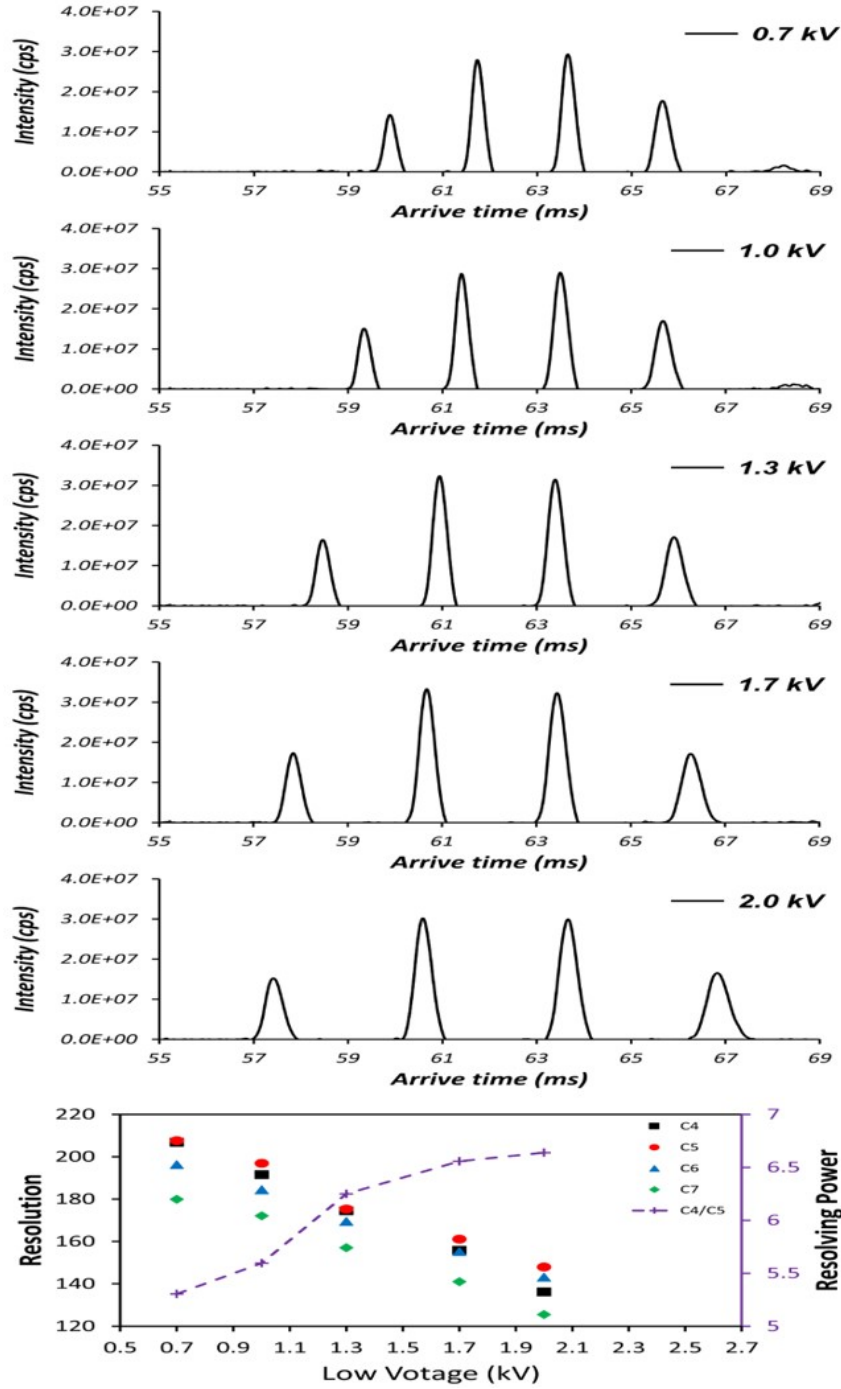
Figure 4.6. Fixing the high pulsing voltage to $5kV$ and pulsing start time to 55ms, adjusting the low pulsing voltage from $0.7kV$ to $2.0kV$. (a)-(e) showed the peaks' intensity as a function of arriving time with low pulsing voltage at $2kV$, $1.7kV$, $1.3kV$, $1kV$ and $0.7kV$, respectively. (f) Resolution of the monomers (C_4^+, C_5^+, C_6^+ and C_7^+) as a function of low pulsing voltage. The right y-axis shows the resolution as a function of the voltage (purple dashed line).
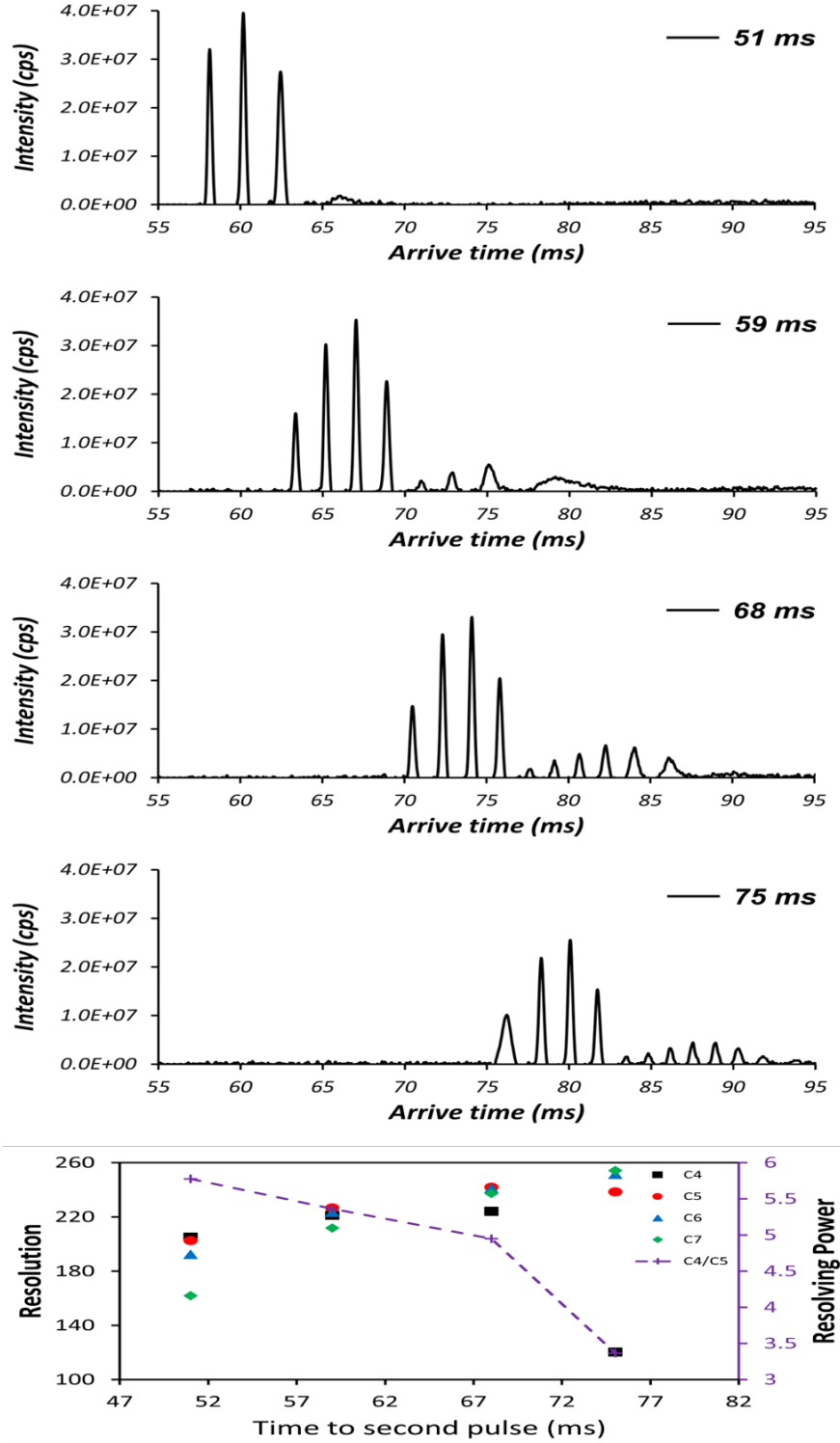
Figure 4.7. Fixing the high voltage $5kV$ and low voltage $0.7kV$, adjust the pulsing time from 75ms to 51ms. (a) The signal intensity as a function of arrive time. (b) Resolutions of the monomers (C_4^+, C_5^+, C_6^+ and C_7^+) at these pulse times. The right y-axis shows the resolution as a function of the voltage (purple dashed line).
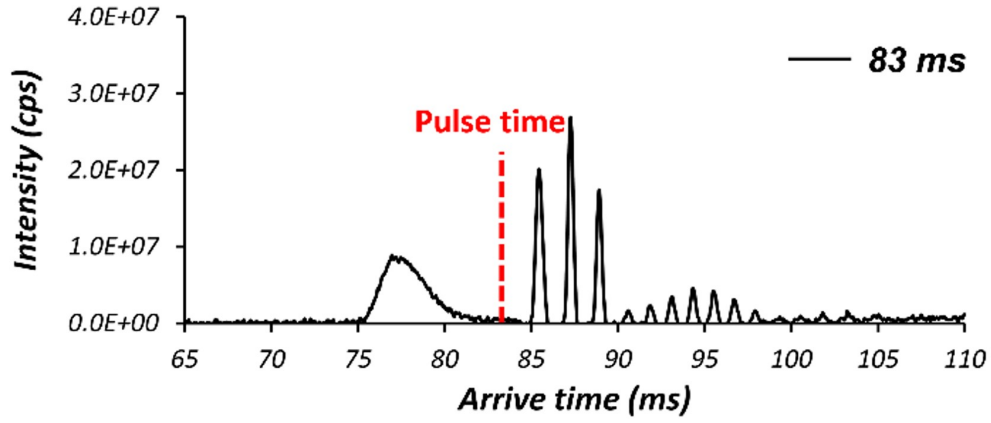
Figure 4.8. With a low pulsing voltage of $0.7kV$ and a pulsing start time of 83ms, the signal of C_4^+ reached to the detector before the pulsing start time. The temporal distribution is therefore much broader consequently decreasing resolution significantly. This is the resolution that was observed prior to the HVP technique

5. DETERMINATION OF GAS-PHASE ION STRUCTURE OF LOCALLY POLAR HOMOPOLYMERS THROUGH HIGH-RESOLUTION ION MOBILITY SPECTROMETRY-MASS SPECTROMETRY

This section is from a published manuscript of the author of this dissertation from ref. [123]. Author Xi Chen and co-author Shannon Raab have contributed equally to this manuscript. Xi Chen has contributed to the sample preparation, designing and working the experiment as well as to the review of the manuscript. Shannon Raab has contributed to the experimental setup and running the experiments. Author Timothy Poe and Dr. David Clemmer have contributed to the review of the manuscript. Author Dr. Carlos Larriba-Andaluz (the corresponding author) has contributed to the data analysis, validation, writing the original draft, and to the review and edition of the manuscript.

5.1 Overview

Synthetic and natural polymers play an essential role in modern day life across all different disciplines and industries (e.g., biological, chemical, pharmaceutical, additive manufacturing, industrial, etc.) [124]–[128]. Their interest resides in their large variety in composition, structure, molecular weight, and their distinct and unique physical properties [129], [130]. Indeed, global production of synthetic polymers has reached 300 million tons and is expected to double in the next 10 to 15 years [131]. In the biological context, all organic macromolecules such as nucleic acids, proteins, and polysaccharides are polymers with fundamental functional roles where structure is a key component [132], [133]. As more advanced manufacturing techniques surface and better understanding of biological processes arise [133], polymers are bound to become the building blocks of synthetic and natural molecular motors [134], will have important roles in information processing at the nano-level and may give rise to intricate self-assembled nano-objects [135]–[138]. A deeper understanding of polymers as single physical objects is however crucial for these promising applications to materialize.

In recent years, techniques such as single-molecule spectroscopy and optical tweezers have allowed us to control biological macromolecules as single entities, where folding or misfolding may be studied and imitated with synthetic counterparts [139]–[142]. Important advances in mass spectrometry (MS) have also allowed polymers to be uniquely characterized individually [143]–[146]. When MS is coupled with orthogonal techniques such as ion mobility spectrometry (IMS), a new dimension is brought forth that also yields insight into the gas-phase structures of these ions. When used in conjunction with electrospray ionization (ESI), ESI-IMS-MS has provided valuable structural information of polymers in the gas phase [147]. Most notable are the studies of the hydrophilic homopolymer polyethylene glycol (PEG), whose very simple backbone structure and ability to hold positive charge (through its oxygen sites) has led to some of the most revealing spectra in the field of ion mobility.

Initial work by Fenn and colleagues on PEG using MS showed that even with mean molecular weights in the range of megadaltons, the highest intensity of the spectra appeared to be at around 900 Thomsons (Th), suggesting that the ions were heavily charged and that the vast majority of the ions would have to be stretched to contain such amount of charge [148]–[151]. Von Helden, Wyttenbach, and Bowers showed using different mechanisms, including IMS-MS and molecular dynamics (MD), that charges in the ion are surrounded by the polymer chain, as if it were solvated, in what was referred to (perhaps later on) as a "beads-on-string" configuration [152]–[155]. The number of monomer linkers surrounding the charge (coordination number) varied between 6 and 12 depending on the polymer used (around 8 for the sodiated PEG structures observed). They were equally successful in showing that more compact globular PEG ions must exist when the level of charging is low enough. Ude and de la Mora combined a differential mobility analyzer (DMA) together with an MS to show that "intermediate" structures were present, between fully globular and stretched, which were uniquely defined for each charge state [156]. Moreover, they hinted at the existence of non-spherical shape families that transcended a single charge state (the same shape was observed in multiple charge states). Trimpin, Clemmer, and coworkers used high-resolution IMS-MS with PEG and other polymers to show that uniquely defined intermediate shapes were present joining the spherical/globular region with the stretched one by a series of sharp kinks attributed to collapsing transitions [157], [158]. MD simulations

of longer multiply charged chains revealed extended structures confirming the "beads-on-string" configuration for ions with a degree of polymerization (DP) of 126 and 9 charges [157], [158]. Within our group, a differential mobility analyzer mass spectrometer (DMA-MS) was used to characterize the full extent of these transitions for the first 8 charge states with multiple incomplete transitions for higher charge states [159]. Careful study of the mobilities revealed that the transition structures may be precisely determined and that the configurations created are heavily dependent on the number of charges and the length of the chain. MD simulations, as well as analytical and numerical collision cross section (CCS) predictions showed that the existing structures were formed by a multiply charged globule with a "beads-on-string" appendix sticking out and where the equilibrium is established by the competition between cohesive forces (Van der Waals) and repulsion between charges [24], [160]. Our group also confirmed the existence of these self-similar shapes predicted by Ude et al., established their structure, and extended their presence to all visible structures and charge states in the spectra up to 8 kDa [159].

The fact that the observed mobility peaks were so sharply defined in both mobility and mass, in contrast to what occurs for example for large proteins where mobility peaks are in general broader than the limit of resolution of the instrument, led to the belief that the ions are at least partially produced by the ion evaporation model (IEM) from the ESI droplet instead of through the more common charge residue model (CRM) for large ions [161]–[163]. This has been corroborated independently by Konermann et al. and Consta et al. through MD simulations and whereby a macromolecule is extruded from a charged droplet attached to the ejected charges in a sequential fashion. Konermann first showed that this effect is applicable to proteins in what has been termed as the chain ejection model (CEM) [164], [165]. Recently, he has shown that the CEM mechanism applies partially to polypropylene glycol polymers as well [166]. Consta, on the other hand, provided simulations of the release mechanisms of PEG and an analytical model for the extrusion of a chain from a droplet [167], [168]. For simplification purposes, we will refer to the release, ejection or extrusion of a chain as chain extrusion, leaving the intricacies of the differences between the methods to more detailed literature [169], [170]. Our group partially confirmed the reality of the chain extrusion process through gas-phase ion activation of two entangled polymer molecules in

the gas phase in an IMS-IMS cell [171]. When sufficient energy was applied, the chains were disentangled in the gas phase and each individual chain instantly rearranged itself onto different configurations depending on the number of charges and the number of monomers in each chain. What is more important, these configurations agreed with the configurations arising from the solution droplet. The ability of the polymer to ion evaporate from a polymer melt in the gas phase and reconfigure itself into a configuration resembling that extruding from a droplet is, in our opinion, clear evidence that charge extrusion and restructuring in the gas phase is a natural behavior for polymer ionization.

More recently, de Pauw's group has been working on a thorough study of polymer topology using IMS-MS where they use the concept of apparent densities to establish relations between mass and CCS [172]–[174]. Many of the implications of the topological study of homopolymers in the gas phase can and should be used to explain some of the behaviors observed in more complex heteropolymers, e.g., nucleic acids and proteins. It has become clear that CCS of proteins in the gas phase are not limited to the biologically more relevant functional form or native state, but rather depend on many other external parameters. Many times, the major contributor to protein deformation in the gas phase is the level of charge, particularly under denaturing conditions where the protein appears extended. However, compaction in the gas phase when the level of charge is relatively low has also been observed for proteins like cytochrome C, immunoglobulins, or even viruses [175]–[184]. This complexity is enhanced by the details of how the ions are handled prior to mobility measurements, including the conditions in the solvent, the ionization process, or the pressure changes in the interface. All these effects yield different configurations, especially under denaturing conditions, that must be interpreted in order to correctly answer the most pressing issue; which, if any, of the gas-phase configurations corresponds to the native structure of the protein?

To further explore and understand the gas-phase structures of homopolymers and heteropolymers, this manuscript explores the concept of local monomer polarity in homopolymers to extend the structural configurations already observed in PEG to other polymers such as polycaprolactone (PCL) and polydimethylsiloxane (PDMS). The idea herein is that the oxygen (electronegative) sites present in the PCL and PDMS monomers, as shown in
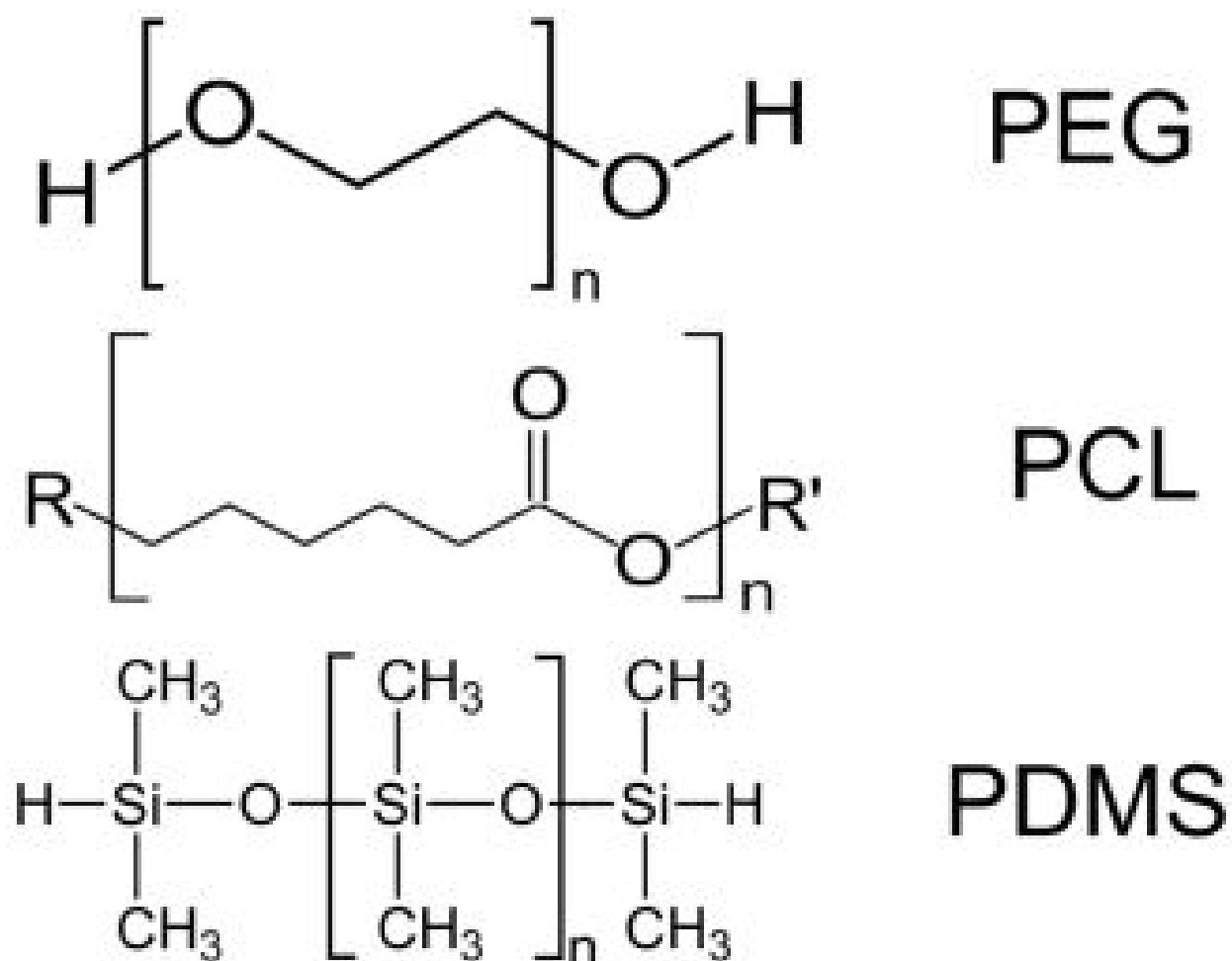
Figure 5.1. Sketches of polymers.

Figure 5.1, is sufficient to bind the polymers to the charging agent (in this case ammonium) despite the overall molecule being somewhat non-polar (non-miscible in water). A feature of the structures must therefore be the flexibility of the polymer to wrap around the charge together with the enhanced attraction produced by the existing polar bond. PCL and PDMS were also chosen because both present discernable differences with respect to PEG. PCL is intrinsically very similar to PEG with a very simple backbone chain and a single oxygen as a pendant group, but where the monomer is almost three times the mass of the PEG monomer, increasing the mass over charge gap between consecutive ions. The carbon to oxygen ratio has also been increased from 2 to 1 for PEG from 5 to 2 for PCL which has implications in

the monomer coordination number. On the other hand, PDMS has an organosilicon based backbone with a monomer molecular mass between that of PEG and PCL. PDMS, however, has two methyl pendant groups that shield the heavily polarized backbone. These pendant groups also reduce the flexibility of the chain and contribute to the transitions occurring at larger masses and lower mobilities.

The studies of these three polymers are made using two very different IMS-MS systems and conditions albeit with the similarity that the mobilities calculated in both systems are directly related to the raw variables used. The first system is an ultra-high resolution ($R \sim 150 - 400$) 4 m drift tube that operates at low pressure and He gas coupled to an in-house MS system. The second system is a high resolution ($R \sim 50 - 60$) DMA system that operates at atmospheric pressure in N_2 coupled to a commercial triple-quadrupole time of flight system (ToF). Both systems use similar ESI sources to ionize the same analyte solutions in order to lower the amount of external variables that might affect the gas-phase configurations. It is shown that the gas-phase structures are independent of the buffer gas and pressure used (at least in the range studied) and that the different transitional changes in each of the polymers seem to appear at the same mass over charge for either experimental system. The high resolution achieved with the drift tube allows many of the transitions to be completely resolved clearly for the first time where charge states "interweave". These transitions seem to extend to very high charge states and masses (up to the resolving power of the instrument and up to hundreds of kDa) without any observable difference in the family self-similar shapes. As such, the globule plus appendix structures present in PEG are confirmed for the other two polymers. Moreover, the transitions for PCL appear to be analogous to those of PEG while PDMS follows similar trends but with less sharp transitions. This is to be expected due to the increased steric hindrance caused by the methyl pendant groups.

5.2 Experimental Setups and Methods

Two experimental systems were used to obtain the results presented in this manuscript. The first one is an atmospheric pressure Differential Mobility Analyzer (SEADM, P4, Boecillo

Spain, $R \sim 50 - 60$) coupled to a triple–quadruple time of-flight (ToF) mass spectrometer (QSTAR XL, $R \sim 10,000$) [34]. The second system corresponds to a homemade 4-m low-pressure drift tube ($R \sim 150 - 400$) coupled to a ToF system (DT-MS). Both systems, each with their own electrospray emitter, are described below.

5.2.1 Differential Mobility Analyzer Mass Spectrometer (DMA-MS)

The operation of the DMA has been shown previously, and only a brief explanation will be provided here [185]. The DMA is, as its name suggests, a filter that transmits a single ion mobility (within the instrument's resolution) under a specified condition. For the parallel plate DMA used in this work, see Figure 5.2A, mobility classification may be achieved by applying a voltage difference between two parallel plates while a sheathed gas (nitrogen) flows between these plates at a constant velocity. Ions entering a slit on the top electrode will be pushed downstream by the sheathed gas while drifting towards the bottom electrode due to the electric field. This combination of voltage and gas flow spreads the ions spatially depending on their mobility. An outlet slit placed on the bottom electrode 4 cm downstream of the inlet slit allows ions of a particular mobility to drift into the QSTAR MS which operates in RF mode only. Varying the voltage will modify the ion mobility that is transmitted into the MS. The desired mobility is easily obtained from the voltage through the linear equation:

$$K_{DMA} = k/V_{DMA} \tag{5.1}$$

where K_{DMA} is the ion mobility, VDMA is the DMA voltage applied, and k is a value proportional to the distance between electrodes, the distance between slits, and to the velocity of the gas flow. Due to the difficulty in accurately calculating the flow velocity, k is normally obtained through calibration. In this manuscript, THA^+ ion was used to calibrate the spectra ($K_{cal} = 0.984 cm^2/Vs$ at room temperature and pressure) [186]. An IMS-MS scan and spectra are therefore produced by ramping the voltage (at steps of a few volts every second) within a range of desired mobilities. Some of the advantages of the DMA are that it is able to work at atmospheric pressure, that its integration with any existing MS can

110

be done very easily, that it allows only a single mobility into the MS, and that its mobility is easy to relate to the raw variables employed. While the base resolution of the DMA is set at 50-60, one can obtain resolutions larger than 110 [97]. In fact, some of the resolutions observed in this manuscript for large charge states is above 175.

5.2.2   ESI Electrospray for DMA-MS

In order to electrospray the polymer ions, samples were introduced into a 1.5 mL polypropylene vial, which was pressurized above atmosphere to push the solution through a silica capillary (Polymicro Technologies, ID $41\mu m$, OD $360\mu m$). The silica was tapered at the tip to ease the anchoring of the meniscus. An HV floating power supply (EMCO HV Co., Sutter Creek, CA) is then used to apply a voltage between the liquid reservoir and the top electrode producing a Taylor Cone and a microdroplet jet. The Taylor Cone was monitored through a camera until it was visually stable and produced a constant current of 70 - 180 nA measured with a multimeter. The capillary was then centered and placed 0 - 2 mm away from the DMA slit so that ions were not lost in the spread. A small counter-flow (0 - 0.4 lpm) of nitrogen (similar to a curtain gas) was employed to ensure any neutrals from entering the system while enhancing the solvent evaporation.

5.2.3   Drift Tube Mass Spectrometer IMS-MS (DT-MS)

A home-built 4-m drift tube coupled to a ToF mass spectrometer was used for DT-MS analysis. A description of drift tube theory of similar instrumentation has been given in detail previously [28], [54], and only a brief description is provided here together with the sketch shown in Figure 5.2B. Ions produced by ESI enter the IMS-MS instrument through a narrow capillary and are stored in an hourglass-shaped ion funnel. A $100 - \mu s-$wide electrostatic gate is used to pulse the ions into the drift tube at specified intervals. The ion packet then traverses the drift region under the influence of a uniform electric field ($11.5 V cm^{-1}$) and is free to collide with a neutral buffer gas (~ 3.0 Torr He). After every meter of separation, the diffuse ion packet is radially focused by ion funnels with applied RF potentials (F$\sharp$ in the figure). When the ions exit the drift tube through a differentially pumped region, they are

pulsed into a two-stage reflection-geometry ToF-MS and separated by their mass-to-charge ratios (m/z). The corresponding drift times and flight times are detected by a microchannel plate and are recorded in a nested fashion [187]. The conversion from drift time to mobility, K_{DT}, is hence given by:

$$K_{DT} = k^{'}/t_{drift} \tag{5.2}$$

Here, $k^{'}$ is a constant (length divided by electric field) that establishes the relation between mobility and drift time. In a similar fashion to the DMA, $k^{'}$ is not directly calculated and a calibrant is used to obtain the mobility. In this work, the doubly charged Bradykinin ion (m/z $\sim$ 530 Th, CCS $\sim$ 246 A^2) is used to calibrate the spectra.

5.2.4   ESI Emitter Fabrication for DT-MS

Uncoated borosilicate glass (ID 1.2 mm, OD 1.5 mm) was purchased from Sutter Instrument Co. (Novato, CA). The 10 cm long capillaries were pulled with a Sutter P-97 micropipette puller to produce electrospray capillaries with $10\mu m$ tip sizes and taper lengths of $\sim$ 4 mm. These tips have been well characterized previously by scanning electron microscopy to ensure reproducibility. The polymer solution was inserted into the back of a pulled emitter, and a 0.25-mm platinum wire was inserted into the solution. The emitter was positioned onto a stage for alignment to the IMS-MS instrument. An ESI potential between 1 and 2 kV (Bertan, Spellman High Voltage, Hauppauge, NY, USA) was connected to the platinum wire to generate ions for analysis.

5.2.5   Analytes

Solutions of micromolar concentrations of polymer in different solvents with varying levels of ammonium acetate (AmAc, Sigma-Aldrich, St Louis, MO) were used. Polyethylene glycol 12 kDa (Sigma-Aldrich), at concentrations of $300\mu M$, was dissolved in a 50/50 water-methanol (UPLCgrade, Sigma-Aldrich) mixture with the addition of 10 - 30 mM AmAc. Due to the non-solubility of PCL and PDMS in water, toluene (Sigma-Aldrich) was used

for the other polymers. One hundred to $300\mu M$ poly-caprolactone 14 kDa (Sigma-Aldrich) was dissolved in a 50/50 toluenemethanol with concentrations of 10 - 70 mM AmAc salt. Concentrations of 100 - 300 μM of PDMS 25 kDa (1150 cSt, Sigma-Aldrich) in a 50/50 solution of toluene and methanol with 30 mM of AmAc. The densities used for the polymers are $1115 kg/m^3$ for PEG [188], $1145 kg/m^3$ for PCL [189], and $965 kg/m^3$ for PDMS [190].

5.2.6 Calculations of CCS

In order to relate the mobility of the ions to their CCS in the gas phase, one can make use of the well-known Mason-Schamp equation for small ions in the free molecular regime [53]:

$$K = \frac{3}{16}\frac{ze}{N}(\frac{1}{m} + \frac{1}{M})^{\frac{1}{2}}\sqrt{\frac{2\pi}{k_b T}}\frac{1}{\Omega_{gas}} \tag{5.3}$$

Here, z is the integer charge number, e is the elementary charge, k_b is the Boltzmann constant, T is the temperature, N is the gas density, m and M are the molecular mass of the gas and the ion (respectively), and Ω_{gas} is the CCS of the ion which depends on the buffer gas used. The raw variable DMA-MS voltage may be transformed into mobility by use of the calibrant ion data. This mobility, in turn, is transformed into CCS through Eq. (5.3). If mobilities are preferred, the CCS obtained with the calibrant data from the DT-MS could in turn be transformed into mobility.

5.3 Results and Discussion

To explore the reasons why homopolymers seem to arrange themselves in well-defined structures in the gas phase, polymers with very distinct monomer units were used in conjunction with different IMS-MS systems working at different conditions of pressures in different gases.

The homopolymers, PEG, PCL, and PDMS, were carefully chosen for this study for their unique similarities and differences, with their backbone chains sketched in Figure 5.1. A shared characteristic of these polymers is that the monomer unit possesses some local

electronegativity so that the positive charging agent employed can easily attach to the site and allow the polymer to hold a vast amount of charge. While completely non-polar polymers, e.g., polypropylene, will never hold sufficient charge to become stretched in the gas phase, it is also not necessary for the polymer to be globally polar or hydrophilic. As such, even though PEG is soluble in water, the other two polymers are not despite having polar covalent bonds. In the case of PDMS, the non-polar methyl groups shield the backbone of the structure yielding it non-soluble in water. PCL is known for its hydrophobicity and as such can only be dissolved in non-polar solvents such as toluene. Despite this, PCL has a local polar region (see sketch) which is not shielded and where positive charge can easily attach.

The monomer unit masses of 44 Da for PEG, 74 Da for PDMS, and 114 Da for PCL will give a reasonable range of monomer molecular masses to compare. The mean molecular weights of the polymers are 12 kDa, 25 kDa, and 14 kDa, and the distributions are very broad, so it is expected that masses ranging from a few hundred to tens of thousands of Daltons may be observable in the mobility-mass spectra.

The addition of AmAc salt increases the conductivity of the sample while allowing ammonium ions to attach themselves to the polymer chains. Even though other charging agents may work as well, AmAc is specifically chosen in this case for its ability to attach to the polymer sites strongly. While not shown here, AmAc produces the least number of evaporation events (loss of charge in the IMS or MS regions) when compared to other charging agents. It seems that the hydrogen in the ammonia ion enhances the ability of the charge to stick to the polymers' oxygen sites, in comparison to for example Na^+, especially in the air to vacuum interface and in particular when declustering potentials are used [171]. If the charging agent was to be negative, then very few charges should attach to the chain. As expected, electrospraying PEG in negative mode only yields globular ions [191].

5.3.1 IMS-MS Studies under N_2 and He Gases

To study the effect of different gases on the structural configuration of the polymers, two distinct systems have been used. A DMA-MS which works in N_2 at atmospheric pressure and

a DT-MS which works in He at low pressure ($\sim$ 3 Torr). The systems are different enough that the similarities between the two results might give insight into the generalization of the gas phase configurations produced. Both systems are also alike in the sense that mobility is inversely proportional to the raw data variable in the abscissa axis, be it drift time or DMA voltage, making the interpretation and comparison easier. All three polymers were run under both systems and the results are shown in Figure 5.3. Figure 5.3 contains six color scheme contour plots where the ordinate axis corresponds to mass over charge in Thomsons and the abscissa axis corresponds to the raw variable pertaining to the particular system (drift time or DMA voltage). The false color scheme determines the intensity which is only representative of the signal that arrives at the detector but is not guaranteed to relate to the real mass distribution of the polymer ions. Figure 5.3a, b shows PEG 12 kDa under He (a) and N_2 (b) environments, Figure 5.3c, d shows PCL 14 kDa under He and N_2, respectively, and finally, Figure 5.3e, f shows PDMS 25 kDa for the same two gases.
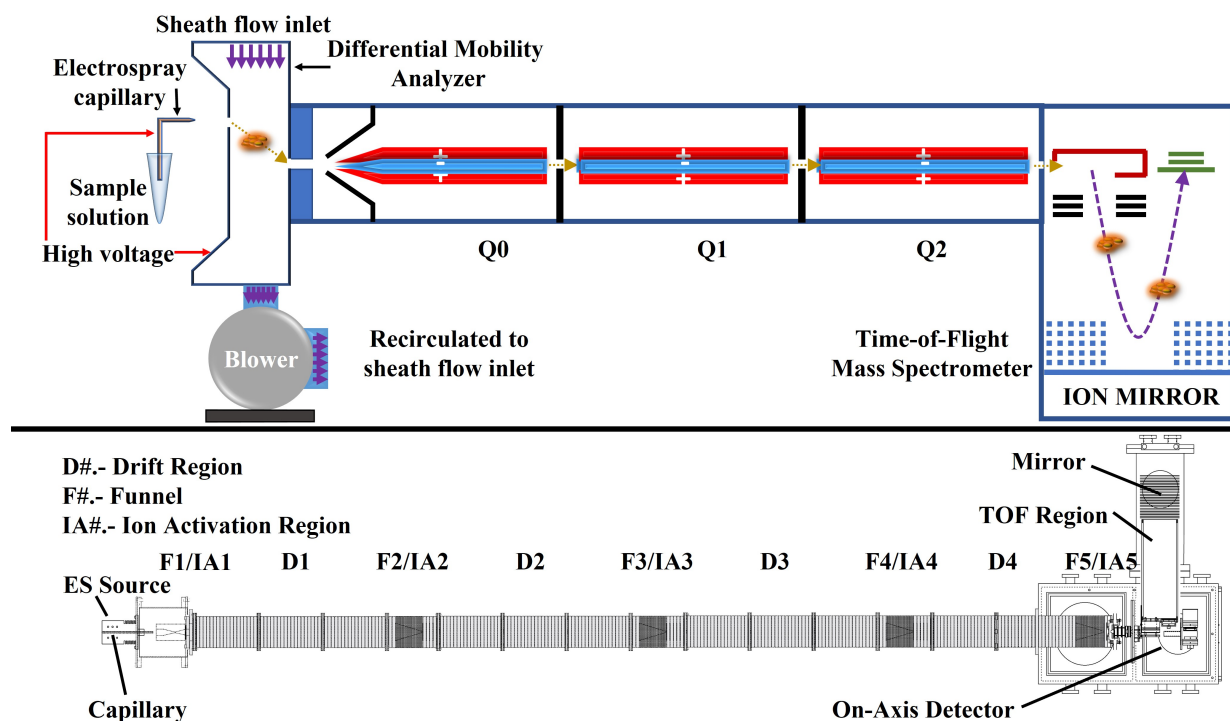
Figure 5.2. Experimental sketches of (a) DMA-MS and (b) DT-MS.

5.3.2 Particularities of Contour Plots

The ionic spectra produced are quite similar regardless of the polymer or gas used and certain parallelisms can be made for all plots. Some of the features have already been described previously for PEG, and only a brief explanation of those is provided here [159], [160], [171]. Since the homopolymer mass distributions are quite broad, the plots are populated by a myriad of ions which correspond to different chain lengths (different DP) centered, in general, on the mean molecular weight of the polymer. These chains may also have varying amounts of charge for the same length which ultimately leads to the wide spectra observed. The fact that the jump between two ions differing one monomer link is constant in mass over charge, m/z, leads to distinct tracks in the plots which are easily discernable and correspond to constant charge states labeled +z. Depending on the degree of polymerization, the chains arrange themselves in different structures within the tracks. For each track, three regions are readily observable: (1) the heavily charged fully stretched region at low m/z and high mobilities, (2) the low-charge globular (spherical) region at small mobilities and medium to high m/z (see Figure 5.3b showing the globular region for charge state 4), and (3) a set of transition regions with multiple kinks joining the globular region to the stretched region.

Before describing each individual polymer plot in detail, the highly resolved plots provided by the DT will easily provide a more in-depth explanation of the tracks and transitions. PEG spectra in He may be used for this purpose as shown in Figure 5.4. Figure 5.4a provides a guide to tracks + 5 through + 8 as they intertwine through the various kinks from globular to stretched as m/z is lowered. While tracks + 1 through + 7 are complete, tracks + 8 through + 13 can be followed for some or most of the track (up to the highest m/z observable by the MS). Higher charge states are also visible, but the tracks are incomplete and only appear partially in regions corresponding to the mean molecular weight of the polymer.

To understand how the polymer ions arrange themselves into different structural configurations in the transition regions, Figure 5.4b describes the process for track + 4. To describe this process, ions are assumed to have entropically driven configurations in the solvent before it is electrosprayed into a plume of droplets. Inside the droplets, or perhaps at the surface, the polymer wraps around the ammonia charges with a coordination number between 8 and

12. As the solvent evaporates, the beads are ion-evaporated from the droplet one at a time (chain extrusion) and conform their structure mid-flight in the gas phase. This sequence of ion evaporation events has been gaining more acceptance and has been described extensively through molecular dynamic simulations [165]–[167], [169], [170], [192]. It also seems to agree with the data presented here for reasons described herein. One of such reasons is the remarkable resolution of the peaks in both mobility and m/z. In general, in Dole's charge residue mechanism [162], impurities remaining in the droplet with the ion are known to appear in the IMS-MS spectra which lower resolution in mass and mobility, something not observed here.

Once in the gas phase after the ion ejection, the polymer arranges itself into a particular configuration depending on the number of charges and the length of the chain [159]. An ion with a high degree of polymerization (for PEG + 4, $DP > 182$, m/z > 2000) that desorbs with 4 charges will have enough cohesive force to withstand the existing repulsive forces and become globular. This is represented by letter A in Figure 5.4b. When an ion with 4 charges has a degree of polymerization below the first critical value but above a second critical value (for PEG + 4, $145 < DP < 182$, 1600 < m/z < 2000), the ion will no longer be able to overcome the repulsive forces completely. It will however try to find its most stable configuration-a local minimum - in the gas phase [156], [160]. This has been observed to be a globule with z-1 charges with a single bead appendix sticking out and which corresponds to letter B in Figure 5.4b [159]. In this transition region, between 1600 and 2000 m/z, there are two distinct ion mobility tendencies. The first one corresponds to an increase in CCS as the m/z is lowered, while the second one corresponds to a decrease in CCS with decreasing m/z. The only possible scenario for these two sharp tendencies to occur is that two different restructuring processes occur mostly independent of each other. In the first process, termed from here on inverse evolution (from m/z of 2000 to 1700-1750 Th for PEG + 4), chains with subsequently lower DP will reconfigure themselves so that the appendix becomes longer at the expense of losing monomers in the globule. The continuous extension of this appendix greatly increases the CCS and significantly lowers the mobility as the DP is lowered through the track. Somewhere in the 1700-1750 Th, the appendix reaches sufficient length so that the repulsion is small enough and the appendix stops growing.

117

At this point, the second process starts-termed forward evolution-and covers in PEG + 4 a reduction in the DP from 1750 to 1600 Th. The reduction of DP seems to only affect the size of the globule with the remaining charges (z = 3) keeping the appendix length constant and thus the trend is reversed (CCS lowers with mass). This reduction of the globule continues until the repulsion in the globule is strong enough that the ion cannot group all three charges together and a second appendix is produced, which is normally an extension of the first (100 < DP < 145). As such, a second transition occurs from 1600 to 1100 Th with the same characteristics as the first. In here, from around 1600 to 1400 Th, the second appendix protrudes in the inverse evolution portion while from 1400 to 1100 Th (C in Figure 5.4b), the globule with the remaining 2 charges is reduced in the forward evolution (to letter D in Figure 5.4b). When the ion's DP is small enough (DP < 100), there are not sufficient monomers to group two charges in a single globule and the ion remains fully stretched with perhaps a slightly larger singly charged globule (E in Figure 5.4b).

These sets of transitions, each with a forward and inverse evolution, occur in the same fashion for all existing tracks (and all the polymers studied here) as shown in Figure 5.4a, which finally lead to the interweaved patterns observed in the plots. Each track has no more than z-1 transitions from globular to fully stretched. The transitions are labeled by TX, where X is an integer number from 1 to z-1 and where T1 refers to the transition closer to the stretched region (as observed in Figure 5.3). In higher charge states (+ 5 or greater), some of the last transitions (into the globular region) are skipped probably due to the fact that the repulsive-cohesive equilibrium length for the last remaining portion of the appendix does not seem to be reached before a new charge must leave the globule.

5.3.3 Particularities of the PEG Spectra

While the PEG ion has been explored extensively before as shown in the introduction, it has not been done with the detail of resolution provided here. The high resolution of the DT-MS in He allows the first four (starting from the stretched side) transitions to be fully discernable for a multitude of charge state tracks as they interweave each other during the inverse evolutions. This will allow a more thorough comparison of the CCS for each track and

transition. Each of these transitions have been labeled in Figure 5.3a as T1 through T4, with T5 also slightly visible. The TX label is also followed by an arrow that points at the inverse evolution portion. Some general rules seem to be present for different tracks within the same transition; for example, inverse and forward evolutions seem to follow similar patterns as if mimicking each other. One inverse evolution that stands out is that of T1 which seems to be weaker than that of other transitions to the point that the CCS remains almost constant (instead of increasing) when lowering the mass over charge.

The N_2 plot, Figure 5.3b, repeats the same spectra as the He plot albeit with lower mobility resolution. The MS used however has a higher m/z resolution and reaches much higher m/z. For this reason, higher globular charge states as well as higher transitions are observable. As shown previously, these larger m/z correspond to more than one polymer chain entangled together [171]. It also seems that the multiple blobs appearing at m/z = 1200 Th and VDMA > 2500, not observed in He, seem to be the first transition, T1, of subsequent entangled chains (labeled "T1 for multiple chains" in the figure). This is supported by the fact that these blobs of multiple linked chains do not continue into the stretched regions as subsequently lower cohesive forces and stronger repulsive ones would most likely disentangle the chains (there is no m/z below 1000 for any of these blobs).

One interesting feature that stands out when comparing both PEG plots is that the kinks and transitions all happen at the same m/z for both gases, N_2 and He, which seems to suggest that the structures formed in the gas phase are not strongly dependent on the gas or the pressure. This also implies that the gas-phase structures are mostly a function of potential interactions confirming previous hypotheses [159], [160]. That the ions seem to arrange themselves always in the same configuration, points out to the ions being able to restructure themselves in the gas phase once the solvent is gone. This has been indirectly proven through IMS-IMS studies of entangled chains [171]. Following the disentanglement of two chains mid-drift through ion activation between two IMS stages, the free chains restructure themselves depending on their new charge into configurations that resemble those of single chains with the same amount of charge coming out directly from the solvent. However, under the same ion activation energies, none of the single chain structures were modified. This points out that either gas configurations are extremely stable or "frozen" as described

by other groups [193], or that they have the ability to restructure themselves extremely fast in gas the phase to an equilibrium structure (or more than one, as shown in Figure 5.3c, where multiple structures seem to coexist in transition regions). For a more comprehensive study of collision induced behavior and fragmentation one can refer to recent work by the Pauw's group [194].

5.3.4 Particularities of the PCL Spectra

The contour plot of the PCL ions is strikingly similar to that of PEG with the added difference that the larger monomer mass of the PCL (114 vs 44 Da for PEG) makes ions individually discernible specially for the lower charge states. The high resolution of the DT contour plot, Figure 5.3c, also allows much higher charge states to be observable. One can easily discern individual ions up to track $+\,17$ and charge states up to $>+\,20$. The portion of tracks in the inverse evolution regions are more spaced out from one another than in PEG to the point where tracks are now fully separated in the first two transitions, T1 and T2. Once again, the inverse evolution of T1 is weaker and becomes barely distinguishable from the actual forward evolution for the larger charge states. The other three visible inverse evolutions work in a similar fashion to PEG which seem to give the contour plot a certain 3D depth. Since more charge states are visible, one can certainly see in this figure that the locus curve joining the maximum mobility for the inverse evolutions of each transition tends towards an asymptotic value that seems to be same for all the transitions. One last interesting detail observable in Figure 5.3c is that there seems to be more than one structural configuration in some of the inverse evolution regions as captured in the inset for tracks $+\,3$ and $+\,4$. Given the small variation in mobilities, the structures should be quite similar to each other and could be the result of spurious charging agents contained in the solvents.

The contour plot for PCL in N_2 appearing in Figure 5.3d follows very similar patterns to that of He. Higher charge states are also present here, although the lower mobility resolution precludes separation for charge states higher than 8, although up to charge state 14 is discernable in some portions as shown in the inset. Similar to the case of PEG, the kinks and transitions seem to happen again at the exact m/z for both He and N_2, something

easily verifiable for charge states $+2$ through $+5$. What is even more thought-provoking is the fact that the kinks and transitions happen at very similar m/z and mobilities as those of PEG, albeit smaller m/z. This is regardless of the fact that the monomer unit mass of PCL is almost 3 times that of PEG. This suggests that the PCL monomer is flexible enough so that it can wrap around the charge in a similar fashion to how 2 to 3 monomers would do in the case of PEG. The beads on a string configuration suggests then that for PCL, the coordination number for every charge would be 3 to 5 instead of 8 to 12 for PEG. This would correspond to 6 to 10 oxygen sites per charge for PCL (with 15 to 25 carbons) and 8 to 12 oxygen sites for PEG (with 16 to 24 carbons).

5.3.5 Particularities of the PDMS Spectra

The PDMS contour plots follow once again similar patterns to PEG and PCL but have unique features due to the difference in monomer size. While the molecular weight of 74 Da of the monomer is between that of PEG and PCL, the pendant methyl groups bonded to the Si atom increase the girth of the polymer chain causing a steric hindrance for the polymer to wrap around the charges. This results in the transitions and kinks occurring at much longer drift times (larger CCS) for the same electric field than for previous polymers as seen in Figure 5.3e for He. The transitions and kinks also occur at larger m/z than previous polymers, and careful conversion shows that the DP necessary to become globular is larger than that for PEG and certainly much larger than that for PCL. This suggests that the cohesive forces per monomer are lower in the case of PDMS. The girth also contributes to more gentle evolutions-inverse and forward-where the mobility varies very smoothly for a given track for a large range of m/z. This is particularly visible in the N_2 plot of Figure 5.3f where mobility is almost constant for tracks 4+ through 10+ from 2000 to 3000 Th (shown in the inset). This has important implications in the study of unfolded proteins as chains of polypeptides would most likely follow gentler evolutions than those produced by PEG or PCL. While there seems to be 3 transitions for track $+4$ and 2 for track $+3$, they are difficult to discern. As such, Figure 5.3f shows a curve joining the center line of the tracks with the transitions labeled as T1-T3.

Another outstanding feature of the PDMS contour plots is the existence of cyclic polymers which give rise to a new set of tracks (see Figure 5.3e, f) labeled PDMS-O (also visible in PCL and labeled PCL-O). The fact that they are cyclic can be verified easily through the mass deficiency of the ending groups when compared to their linear counterparts. These tracks differ considerably in mobility from the linear polymer ones (labeled Y-PDMS-X) in the stretched (the chain should be about half the length and double the molecule girth) and transition regions [160], [195]. However, linear and cyclic tracks should eventually merge into one as the ion becomes globular. This can be observed in the PDMS figures from track + 1 to track + 4. Despite this merging, the two tracks may be discernable when sufficient resolution is present in mass and/or mobility. This is visible in Figure 5.3f for charge state + 1.

5.3.6 Self-Similar Family Shapes in He and N_2 for Polar Polymers

It has been shown previously that the transition configurations for the PEG polymer in N_2 follow well-defined sets of self-similar family shapes that transcend different charge state tracks [156], [159], [160], [172]. It will be shown here that these self-similar shapes are not only exclusive to PEG in N_2 but that they also occur for other polymers with a local polar component. Moreover, they are not exclusive to a particular solvent and happen under different pressures and or gases. From these studies, it can be extrapolated that the self-similar shapes must therefore be only as a result of the potential interaction between charge repulsion and VdW cohesive forces within the gas phase and not as a result of the effect of solvents, buffer gases and or pressures. In order to show that this is indeed the case, the mobility and m/z of individual tracks for different charge states was obtained from the contour-plots by isolating each charge state individually. The crossing/interweaving of the different charge states obstructs this process, as the intensity of a single charge state is falsely enhanced at these intersections (due to the additional intensity of other charge states). Therefore, for each individual track, mobility and mass can be well defined for each charge state, meanwhile intensity information is more complicated and will be removed for this process.

Useful structural information can be obtained from using the alternative variables $PA_{s,m}$ (projected area) and the CCS, Ω_{gas}, as shown in Figure 5.5 for PCL and PEG in He and N_2. Ω_{gas} can be inferred from Eq. (5.3) while the $PA_{s,m}$ variable can be obtained from the mass assuming that the ion is to be considered globular and calculating the corresponding projected area as if it were a sphere:

$$PA_{s,m} = \pi((\frac{3m}{4\pi\rho_{pol}})^{\frac{1}{3}} + r_g)^2 \tag{5.4}$$

where ρ_{pol} is density of the polymer and r_g is the radius of the gas (considered here to be as an approximation 1. 55 $\mathring{A}$ for N_2 and 1 $\mathring{A}$ for He). From theory, in the case of hard sphere elastic specular collisions for a spherical ion: $CCS = PA_{s,m}$. Meanwhile, in the case of soft sphere diffuse inelastic collisions, $CCS = \xi PA_{s,m}$, where ξ is the accommodation coefficient with values ranging from 1.36 to 1.41 when the ion-induced dipole is considered [25].

Figure 5.5a, b shows PEG in He and N_2, respectively, while Fig. 5.5c, d do the same for PCL. In all the figures lines corresponding to $\xi = 1$, 1.25, 1.36, and 1.4 are used for guidance. In general, globular ions should fall between lines with $\xi = 1$-1.4 in this plot [196]. In particular, for N_2, it has been shown that due to diffuse inelastic re-emission, this range can be narrowed to $\xi = 1.33$-1.41 for large molecules which is shown to be the case for both polymers [197]. In He, on the other hand, small ions have been shown to have $\xi \sim 1$ [198]–[202]. However, as the size of the ion increases, scattering effects increase the value of ξ. This seems to be the case for the polymers presented here where ξ seems to increase with radii from around 1.25 to values slightly below 1.36.

It is expected that ions which are not spherical will fall out of the globular region as clearly shown in Figure 5.5. It is equally expected that as the ions open up, the effective CCS will be larger than that of a globular ion, $\Omega_{gas} > PA_{s,m}$, of the same mass. By choosing one of the tracks, one can follow the evolution from spherical to stretched. As the mass of the ion (proportional to $PA_{s,m}$) is reduced from the largest globular ion, the ion remains spherical until it eventually reaches a critical mass which leads to the first inverse evolution. This inverse evolution is then followed by a forward evolution which in Figure 5.5 shows up as a region with a similar slope to the globular ions. This process -inverse and forward- is

repeated a maximum of z-1 times for each charged state as the different transitions (emerging appendices) evolve towards the stretched configuration, leading to the brick-wall system seen in Figure 5.5. Remarkably, the forward evolutions observed for each charge state seem to be continued on other charge states in a similar fashion to what occurs in the globular region. These sets can then be grouped into self-similar families, as observed in Figure 5.5 by joining the different tracks with a constant line.

Each of these families have been termed z-x where x corresponds to the number of charges in the appendix. The fact that self-similar shapes have slopes similar to the globular ions (with mobility resolutions > 150 in the case of He) leads to the reasoning that these ions behave very similar to globules but have an additional drag corresponding to the appendix. Within a self-similar family, the variation of CCS seems to suggest that the length of the appendix remains a quasi-constant addition to the CCS (constant jump in CCS with respect to the spherical ion). This constancy remains true within a given track until either the number of monomers in the globule is too small and a new appendix length with a charge protrudes (when traveling through the track towards lower masses) or the number of monomers in the globule is sufficient to absorb one of the charges in the appendix (when traveling towards higher masses). The absorption or ejection of the charge happens during the inverse evolution portion of the tracks which is visualized in Figure 5.5 as a strong deviation of the CCS with respect to self-similar families. Finally, although the maximum charge state shown is 13 in the figure, it is clear from the raw data in He of PCL that the families can be extended to charge states higher than 20.

The fact that the same highly resolved evolutions happen within self-similar shapes for all the discernable tracks, for both polymers, for different gases and pressures, and with different solvents used (water vs. toluene) leaves very little doubt to the accuracy of the structural configurations and assumptions here presented. The only plausible doubt that may remain is whether chain extrusion from the droplet does indeed occur under most scenarios presented here. However, that chain extrusion occurs has also been indirectly proven previously through the calculation of the apparent interfacial tension of a globular polymer as the first charge and appendix leaves the globule. The critical mass, m^*, at which this happens for every track has been shown to be indirectly proportional to z^2 [156],

[159], [160]. This process is reminiscent of the Rayleigh limit of a droplet which relates the maximum charge that a droplet can hold to its surface tension [203]. However, for the known inter-facial tension of the polymer, the experimental values disagree with the Rayleigh limit by around 50%. This indicates that perhaps the process of protruding a charge (akin to the Rayleigh limit) occurs at a different critical mass from that of absorbing a charge (for the same number of charges and mass), as in a hysteretical process, suggesting that the critical mass observed in the contour plots corresponds to that of absorbing a charge, and hence the disagreement. Certainly, the absorption process in the gas phase would only happen if the polymer was indeed ejected from the solvent droplet at least partially unfolded and hence the support of chain extrusion at least partially.

Figure 5.6 shows the evolution of PDMS in N_2 in the same variables as Figure 5.5. While the trends should be similar in He, the plot is omitted as only two tracks are complete. Figure 5.6 is similar in essence to Figure 5.5 but with notable differences that yield important conclusions. Given that PDMS has methyl pendant groups sticking out of the backbone chain, the self-similar shapes are more difficult to pinpoint, in particular those closer to the spherical region. However, the wavy patterns are still discernible for some of the transitions, especially for higher charge states, and the existence of families is further confirmed through the use of auxiliary dashed lines. The softer variations observed for this polymer may have some important implications regarding the study of gas-phase structures of complex homopolymers and heteropolymers. It is expected that for more complex homopolymers, the transition structures will continue to follow similar trends to the ones predicted here albeit not as clearly defined as with simpler polymers. Single structures for a given mass and charge state seem to be predominant for homopolymers as charges can easily slide from one monomer unit to another. However, this does not seem to be the case for highly charged heteropolymers, e.g., denatured proteins, where multiple structures for the same charge state and mass have been observed [204]–[208]. The results proposed here can be extrapolated to suggest that these multiple structures will greatly depend on how the hydrophobic and hydrophilic portions of the protein interact with the charges. However, care must be taken when doing these extrapolations as charge locations may be somewhat pre-established in the solvent and may depend on the level of denaturization and strength of the hydrogen

125

bonding. It is clear, anyhow, that with sufficient information, one should be able to provide an accurate description of the tertiary structure in the gas phase and whether or not this structure is related to the native structure present in the solvent.
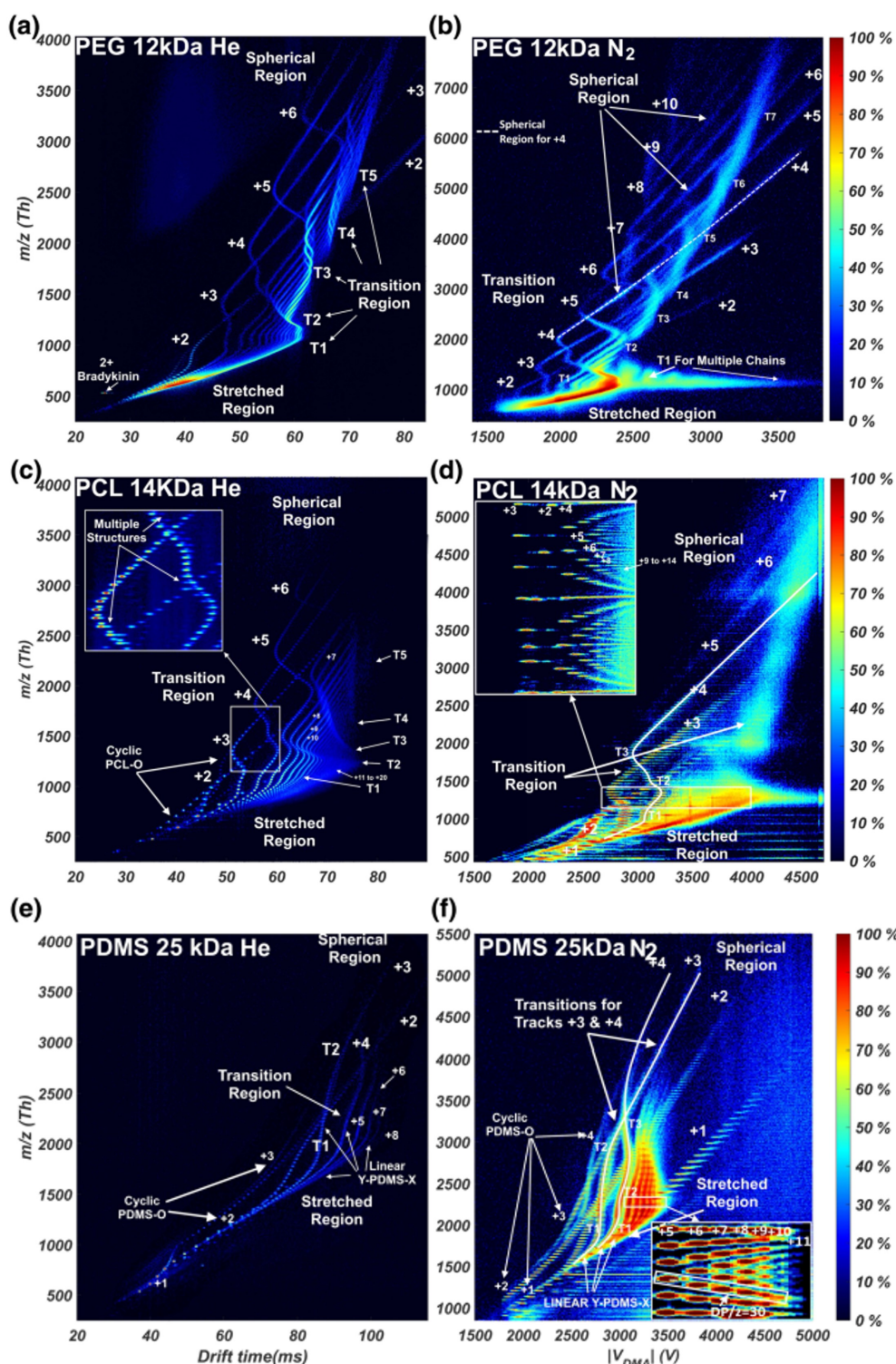
Figure 5.3. Contour plots of polymer spectra in He and N_2 conditions. (a) PEG 12 kDa He, (b) PEG 12 kDa N_2, (c) PCL 14 kDa He, (d) PCL 14 kDa N_2, (e) PDMS 25 kDa He, (f) PDMS 25 kDa N_2.
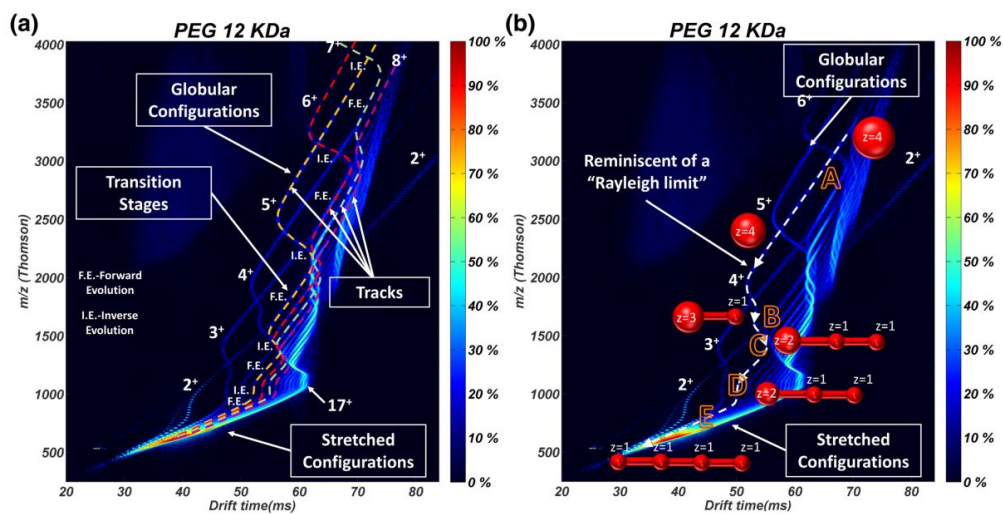
Figure 5.4. (a) PEG contour plot highlighting different charge state tracks as well as inverse and forward evolutions. (b) PEG contour plot showing the evolution of the structures for track +4 from globular to stretched. Letters correspond to the different structures sketched.
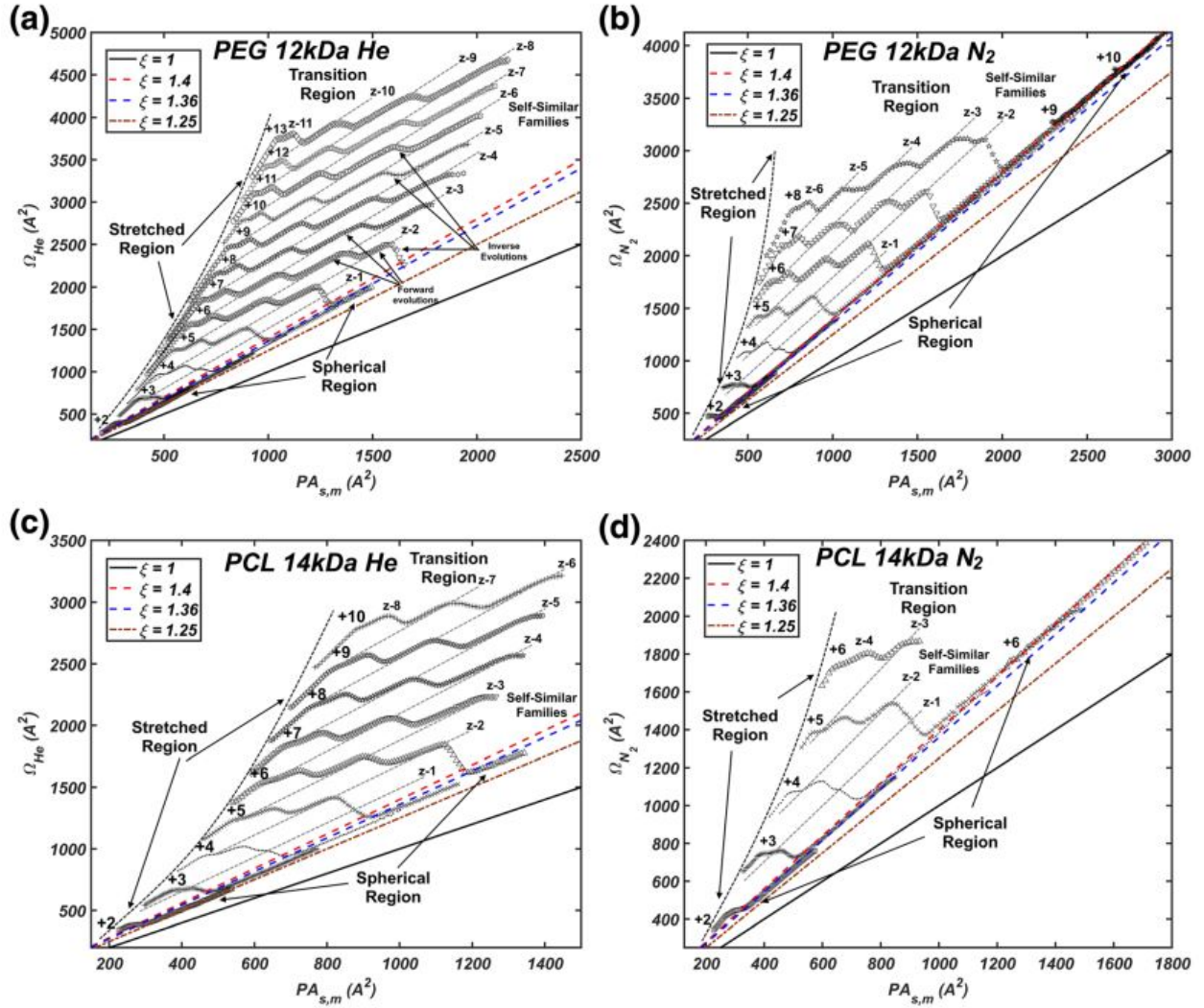
Figure 5.5. CCS vs. $PA_{s,m}$ for different polymers and gases. (a) PEG in He, (b) PEG in N_2, (c) PCL in He, and (d) PCL in N_2. Legend shows the lines corresponding to different accommodation coefficient ξ for a spherical ion of the same density as the polymers.
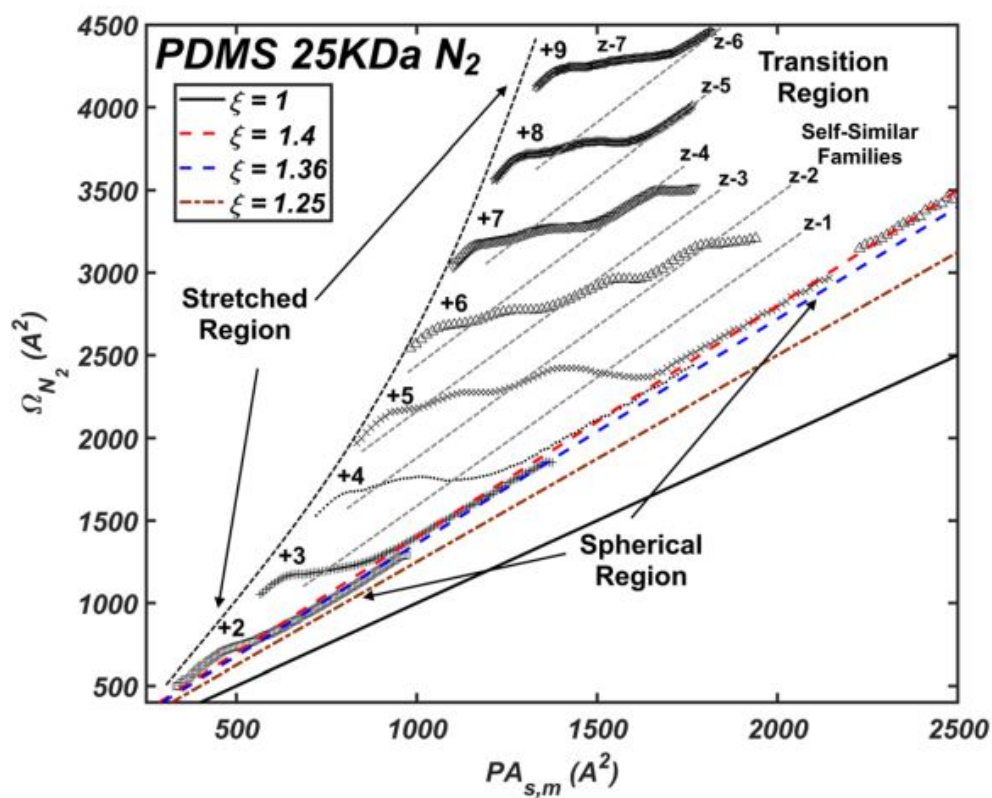
Figure 5.6. CCS vs. $PA_{s,m}$ for PDMS in N_2. Legend shows the lines corresponding to different accommodation coefficient ξ for a spherical ion of the same density as the polymers

6. SUMMARY

The interest of Ion Mobility Spectrometry is increasing rapidly in recent decades, and the corresponding instruments offer a wide range of applications and possibilities in separation and analysis. Not only used as stand-alone instruments, IMS is applied as a pre-separation technique in combination with an MS instrument, which offers one more dimension of information that may be used to separate and identify the components in complex mixtures. To meet with different requirement from various different research areas, plenty of IMS instruments have been developed, e.g., DTIMS, TWIMS, DMA, FAIMS and SLIM. Each of these instruments has their own advantages and shortcomings. One of the main disadvantage is that almost all the IMS instruments suffer from diffusion broadening, a "random" movement of ions in the gas phase that lowers the transmission, reducing the sensitivity of the instrument, and is detriment to the capability for separation. Even though RF technique has been applied at low pressure system to confine the diffusion in the radial direction, which helps to improve the sensitivity of the instrument, the diffusion in the axial direction has not been effectively addressed. A varying electric field has been proven to be useful to constrain the ions in the axial direction and results in what we have named: diffusion auto-correction. In this work, a series of instruments were developed to improve on the separation sensitivity and size range, based on the varying electric field in a drift tube, with a focus on trying to narrow the distribution of ions and increase the resolution of the instrument.

Chapter 2 introduced the Inverted Drift Tube (IDT) system, where two opposite forces - linearly increasing electrical force and a driven force from a gas flow - were employed in the system. Previous work has explained that a linear electric field has diffusion auto-correction that results in a compact ion distribution and high resolution. Here, the 2D Nernst-Planck equation was solved for the first time to study the dynamics of ion distributions. The axisymmetric analytical solution shows that axial diffusion confinement exits and even a broad initial packets of ions can be narrowed further than its starting distribution, which is impossible for other instruments. This "correction" ability depends on the slope of the electric field A. Given the solenoidal aspect of the field, the axial auto-correction comes at the expense of diffusion broadening in the radial direction, that hampers transmission

efficiency and sensitivity, but it is negligible if the ions are centered and could be solved with the application of RF technology in a low pressure system. Numerical and analytical studies were employed to investigate the ion distribution. The results proved that the distribution can reach a asymptotic condition as time passes. Finally, the results are compared to a similar principle in the TIMS system that uses low pressure. We show that, due to the radial broadening of the packet, the stability of the ions in the radial direction when RF is employed has limitation and small ions are prone to be lost. The non-constant velocity profile at every cross section of the IDT is a unfavorable factor for the separation. As revealed in this chapter, the gas flow evolves into a parabolic profile which is not constant inside the tube, and incurs in the ions different axial velocities at different radial positions, in particular for high mobility ions. When separating multiple mobilities, the tails that appear due to the gas flow overlap other peaks in the experimental results, reducing the separation ability of the instrument. Despite this disadvantage, the IDT system has excellent theoretical separation capabilities with resolutions that rival the best gas phase separation systems as long as the gas flow is controlled. A big advantage of the IDT is that larger mobility ions arrive at the detector first, making it possible to be used for very large sizes.

Chapter 3 introduced Varying Field Drift Tube (VFDT) system to overcome the problem of non-constant velocity profile appeared in IDT system. Opposite of the linearly increasing electric field, VFDT applied a linearly decreasing electric field in the first half of the drift region and a constant electric field for the rest of the drift length. A gas flow is only used in the end of the tube to push the ions into the detector. The Nernst-Planck equation was solved theoretically at the beginning of this chapter to reveal that the resolution of the VFDT system is much higher than that of the regular DT. The diffusion auto-correction theory was confirmed experimentally for the first time through testing a mixture of tetraalkylammonium salts. The results show that the resolution achieved within the system is comparable to that of a regular DT and only marginally better. It also shows that the radial broadening effect is not important as long as the ions are centered so that the transmission is mostly unaffected. The resolution, which is dependent on the applied voltage, reached a reasonable average value of 90 in the experiments, where 130 could be obtained under very short initial pulses with very low intensities. The transformation from ion arrival time distribution to the

collision cross section or mobility diameter is calculated to be linear, making the method easy to calculated mobilities for complex analytes. The reason for why the resolution was only marginally higher was discussed in Chapter 4.

Chapter 4 described a High Voltage Pulse (HVP) technology applied on the VFDT system. This chapter first discussed the difference between the spatial distribution and the temporal distribution of the ions in the VFDT system, which is caused by the non-constant drift velocity (in a regular DT, the drift velocity is constant, so the two distributions are equivalent). What was calculated theoretically in Chapter 3 was the spatial resolution while what is obtained experimentally is the time resolution, hence the existing difference. To take advantage of the high spatial distribution of the VFDT, a high voltage pulse is incorporated in the second half of the drift tube and applied at the time of interest. This causes the ions to accelerate and reach the detector at a much higher drift velocity that with the VFDT, considerably increasing the resolutoin of the system. A drift tube simulation was used to study the diffusion auto-correction effect and shows that the ion distribution can be narrowed in the axial direction when a linearly decreasing field is applied, while it can be constricted in the radial direction when an linearly increasing field is employed. An adjustable pulse time permits an narrower distribution than the initial source and much higher temporal resolution. A set of experiments were designed to test the influence of different high voltages and pulse times t_{HVP} on the resolution and resolving power. Consistent resolution between 100 and 250 were obtained with resolving powers between 5 to 10. The resolution is unprecedented for atmospheric pressure IMS systems with 21 cm of length and corresponds to an increase of 3-5 fold. Finally, if RF were to be applied at low pressures, were the radial broadening would not have a strong effect, it is expected that long drift tubes could result in resolutions in the thousands.

Chapter 5 is an application of a drift tube system at low pressures. At He gas environment, we coupled a 4 meter DT to a MS instrument to corroborate the gas-phase structures of homopolymer PEG and reveal their similarities with PCL and PDMS. The results were compared with an atmospheric pressure DMA-MS instrument in N_2 gas environments. The comparison shows that the high resolution achieved with the drift tube allows many of the gas phase transitions to be completely resolved clearly for the first time where charge states

"interweave." These transitions seem to extend to very high charge states and masses (up to the resolving power of the instrument and up to hundreds of kDa) without any observable difference in the self-similar family shapes. These results, in turn, revealed the importance of the resolution and resolving power to an IMS instrument. The higher the resolution and resolving power, the larger the peak capacity and the better the performance of the instrument. The resolution of the 4 meter drift tube at low pressure environment is about 150 for singly charged and up to 400 for multiply charged ions, while the 21 cm HVP-VFDT system achieved a resolution of 250 in an atmospheric pressure environment.

7. FUTURE WORK

- Modification of the ionization method

Even though the electrospray ionization method has many advantages, like the stability and transferring ions directly from solution to gas-phase with little fragmentation, it has some disadvantages, for example, it is hard to control the charges. The problem appears when separating large particles which contains multiple charges. Since the IMS systems separate the ions based on their mobility (dependent of the charge), multiple charges will result in an overlap of individual peaks, making the separation difficult. A corona discharge and radioactive ionization source will be tested in the future to produce singly charged ions and try to obtain the size range that can be achieved with these systems.

- Increase the size detection range

The measurement range of a regular drift tube is, in general, limited to a few nanometers and samples we have already tested in the experiments were tetraalkylammonium salts, that the calculated diameter is around $1 - 3$ nm. Due to the properties of fast response time and high resolution, we would like to develop a drift tube that can be applied in the analysis of aerosol field at atmospheric pressure where the particle size is $0.001 - 10 \mu m$. We have tested large particles (10 nm) with ESI method, the individual peaks were superimposed on each other and cannot be distinguished. When the ionization method is modified, the different varying field instruments will be tested to separate 10 nm, 50 nm and 100 nm particles.

- Optimize the construction of Drift tube

The current instrument is based on a regular drift tube from Kanomax company, which is used to separate small particles sizes (under 10 nm). To separate large particles, high electric fields are required in the drift region. However, the thickness of the electrodes has not been optimized and the electric field in the system is not as uniform as we would like. Therefore, future work will consist in narrowing the thickness of the electrode rings so that more electrodes can be placed or the voltage increased by increasing the insulation portion without the fear of voltage breakdown. Moreover, the inner diameter of the electrode, the

length of the drift region and the flow condition should be taken into account and optimized through CFD and electric field simulation to reduce the diffusion in the radial direction and the effect of the flow field.

- Increase the signal intensity and reduce the noise

The ion current is too small to be depicted on the screen, so it was transformed into voltage signal and got amplified $1E10$ times through an Keithley electrometer (Model 428-PROG, FL, USA) with a $300\mu s$ filter to reduce the noise. To increase the sensitivity of the instrument, a new electrometer is needed with amplification of $1E(11)$ or $1E(12)$. Usually, a increased amplification is accompanied with high intensity of the noise, the RC-CR circuit loop has been empirically proven to be useful to deal with the signal saturation problem and average the noise. And the detector including the BNG cables connected to the amplifier should be totally shielded to protect the signal from the interference of external environment.

- Coupling to a Mass Spectrometer

The coupling of Ion Mobility to Mass Spectrometry is widely used for analysis, as it gives one more dimension of information of the ions, making it possible to separate complex mixtures, especially for ions ions of similar mobilities and/or isotopomers. For example, in Chapter 5, a 4 meters high resolution drift tube was used to coupled with a mass spectrometer to determine the structure information of the polymers. The HVP-VFDT system will be coupled through an API to a mass spectrometer to investigate the properties of aerosol particles as it is expected to greatly outperform the DMA-MS instrument.

- SLIM platform with autocorrection principles

At the end of this thesis, we have begun the construction of a SLIM platform. Instead of the typical T-wave system, we will make use of a modified varying field voltage that has autocorrection features. This will be the first time that the autocorrection will be taken advantage of at low pressures in RF systems. With an 8m board, we expect resolving powers that may reach 1200 in one pass.

REFERENCES

[1] M. Nahin, D. Oberreit, N. Fukushima, and C. Larriba-Andaluz, "Modeling of an inverted drift tube for improved mobility analysis of aerosol particles," *Scientific reports*, vol. 7, no. 1, pp. 1–11, 2017.

[2] C. Larriba-Andaluz, X. Chen, M. Nahin, T. Wu, and N. Fukushima, "Analysis of ion motion and diffusion confinement in inverted drift tubes and trapped ion mobility spectrometry devices," *Analytical chemistry*, vol. 91, no. 1, pp. 919–927, 2018.

[3] X. Chen, M. Latif, V. D. Gandhi, X. Chen, N. Fukushima, and C. Larriba-Andaluz, "Enhancing separation and constriction of ion mobility distributions in drift tubes at atmospheric pressure using varying fields," *Analytical Chemistry*, 2022.

[4] S. Raab, X. Chen, T. Poe, D. E. Clemmer, and C. Larriba-Andaluz, "Determination of gas-phase ion structures of locally polar homopolymers through high-resolution ion mobility spectrometry-mass spectrometry," *Journal of the American Society for Mass Spectrometry*, vol. 30, no. 6, pp. 905–918, 2019.

[5] M. J. Cohen and F. Karasek, "Plasma chromatography™—a new dimension for gas chromatography and mass spectrometry," *Journal of Chromatographic science*, vol. 8, no. 6, pp. 330–337, 1970.

[6] R. S. Louis, W. Siems, and H. Hill Jr, "Evaluation of direct axial sample introduction for ion mobility detection after capillary gas chromatography," *Journal of Chromatography A*, vol. 479, pp. 221–231, 1989.

[7] E. Rutherford, "Viii. uranium radiation and the electrical conduction produced by it," *The London, Edinburgh, and Dublin Philosophical Magazine and Journal of Science*, vol. 47, no. 284, pp. 109–163, 1899.

[8] P. Langevin, "L'ionization des gaz," *Ann. Chim. Phys*, vol. 28, pp. 289–384, 1903.

[9] E. A. Mason and H. W. Schamp Jr, "Mobility of gaseous lons in weak electric fields," *Annals of physics*, vol. 4, no. 3, pp. 233–270, 1958.

[10] E. W. McDaniel, "Collision phenomena in ionized gases," *New York: Wiley*, 1964.

[11] R. Hallen, C. Shumate, W. Siems, T. Tsuda, and H. Hill Jr, "Preliminary investigation of ion mobility spectrometry after capillary electrophoretic introduction," *Journal of Chromatography A*, vol. 480, pp. 233–245, 1989.

[12] D. W. Cooper and P. C. Reist, "Neutralizing charged aerosols with radioactive sources," *Journal of Colloid and Interface Science*, vol. 45, no. 1, pp. 17–26, 1973.

[13] M. Tabrizchi, T. Khayamian, and N. Taj, "Design and optimization of a corona discharge ionization source for ion mobility spectrometry," *Review of scientific instruments*, vol. 71, no. 6, pp. 2321–2328, 2000.

[14] D. Carroll, I. Dzidic, R. Stillwell, K. Haegele, and E. Horning, "Atmospheric pressure ionization mass spectrometry. corona discharge ion source for use in a liquid chromatograph-mass spectrometer-computer analytical system," *Analytical Chemistry*, vol. 47, no. 14, pp. 2369–2373, 1975.

[15] E. De Hoffmann and V. Stroobant, *Mass spectrometry: principles and applications*. John Wiley & Sons, 2007.

[16] G. R. Asbury, J. Klasmeier, and H. H. Hill Jr, "Analysis of explosives using electrospray ionization/ion mobility spectrometry (esi/ims)," *Talanta*, vol. 50, no. 6, pp. 1291–1298, 2000.

[17] P. Rearden and P. B. Harrington, "Rapid screening of precursor and degradation products of chemical warfare agents in soil by solid-phase microextraction ion mobility spectrometry (spme–ims)," *Analytica Chimica Acta*, vol. 545, no. 1, pp. 13–20, 2005.

[18] S. Valentine, A. Counterman, C. Hoaglund, J. Reilly, and D. Clemmer, "Gas-phase separations of protease digests," *Journal of the American Society for Mass Spectrometry*, vol. 9, no. 11, pp. 1213–1216, 1998.

[19] D. Carroll, I. Dzidic, R. Stillwell, M. Horning, and E. Horning, "Subpicogram detection system for gas phase analysis based upon atmospheric pressure ionization (api) mass spectrometry," *Analytical chemistry*, vol. 46, no. 6, pp. 706–710, 1974.

[20] B. H. Clowers, Y. M. Ibrahim, D. C. Prior, W. F. Danielson, M. E. Belov, and R. D. Smith, "Enhanced ion utilization efficiency using an electrodynamic ion funnel trap as an injection mechanism for ion mobility spectrometry," *Analytical chemistry*, vol. 80, no. 3, pp. 612–623, 2008.

[21] N. E. Bradbury and R. A. Nielsen, "Absolute values of the electron mobility in hydrogen," *Physical Review*, vol. 49, no. 5, p. 388, 1936.

[22] C. Chen, H. Chen, and H. Li, "Pushing the resolving power of tyndall–powell gate ion mobility spectrometry over 100 with no sensitivity loss for multiple ion species," *Analytical chemistry*, vol. 89, no. 24, pp. 13 398–13 404, 2017.

[23] H. H. Hill and G. Simpson, "Capabilities and limitations of ion mobility spectrometry for field screening applications," *Field Analytical Chemistry & Technology*, vol. 1, no. 3, pp. 119–134, 1997.

[24] C. Larriba and C. J. Hogan Jr, "Ion mobilities in diatomic gases: Measurement versus prediction with non-specular scattering models," *The Journal of Physical Chemistry A*, vol. 117, no. 19, pp. 3887–3901, 2013.

[25] C. Larriba and C. J. Hogan Jr, "Free molecular collision cross section calculation methods for nanoparticles and complex ions with energy accommodation," *Journal of Computational Physics*, vol. 251, pp. 344–363, 2013.

[26] G. A. Harris, S. Graf, R. Knochenmuss, and F. M. Fernández, "Coupling laser ablation/desorption electrospray ionization to atmospheric pressure drift tube ion mobility spectrometry for the screening of antimalarial drug quality," *Analyst*, vol. 137, no. 13, pp. 3039–3044, 2012.

[27] H. H. Hill Jr, W. F. Siems, and R. H. St. Louis, "Ion mobility spectrometry," *Analytical Chemistry*, vol. 62, no. 23, 1201A–1209A, 1990.

[28] S. I. Merenbloom, S. L. Koeniger, S. J. Valentine, M. D. Plasencia, and D. E. Clemmer, "Ims- ims and ims- ims- ims/ms for separating peptide and protein fragment ions," *Analytical Chemistry*, vol. 78, no. 8, pp. 2802–2809, 2006.

[29] S. I. Merenbloom, R. S. Glaskin, Z. B. Henson, and D. E. Clemmer, "High-resolution ion cyclotron mobility spectrometry," *Analytical chemistry*, vol. 81, no. 4, pp. 1482–1487, 2009.

[30] K. Giles, S. D. Pringle, K. R. Worthington, D. Little, J. L. Wildgoose, and R. H. Bateman, "Applications of a travelling wave-based radio-frequency-only stacked ring ion guide," *Rapid Communications in Mass Spectrometry*, vol. 18, no. 20, pp. 2401–2414, 2004.

[31] A. A. Shvartsburg and R. D. Smith, "Fundamentals of traveling wave ion mobility spectrometry," *Analytical chemistry*, vol. 80, no. 24, pp. 9689–9699, 2008.

[32] K. Giles, J. L. Wildgoose, D. J. Langridge, and I. Campuzano, "A method for direct measurement of ion mobilities using a travelling wave ion guide," *International Journal of Mass Spectrometry*, vol. 298, no. 1-3, pp. 10–16, 2010.

[33] P. Intra and N. Tippayawong, "An overview of differential mobility analyzers for size classification of nanometer-sized aerosol particles.," *Songklanakarin Journal of Science & Technology*, vol. 30, no. 2, 2008.

[34] J. Rus, D. Moro, J. A. Sillero, J. Royuela, A. Casado, F. Estevez-Molinero, and J. F. de la Mora, "Ims–ms studies based on coupling a differential mobility analyzer (dma) to commercial api–ms systems," *International Journal of Mass Spectrometry*, vol. 298, no. 1-3, pp. 30–40, 2010.

[35] V. Pomareda, S. Lopez-Vidal, D. Calvo, A. Pardo, and S. Marco, "A novel differential mobility analyzer as a voc detector and multivariate techniques for identification and quantification," *Analyst*, vol. 138, no. 12, pp. 3512–3521, 2013.

[36] H. Borsdorf and G. A. Eiceman, "Ion mobility spectrometry: Principles and applications," *Applied Spectroscopy Reviews*, vol. 41, no. 4, pp. 323–375, 2006.

[37] I. Buryakov, E. Krylov, E. Nazarov, and U. K. Rasulev, "A new method of separation of multi-atomic ions by mobility at atmospheric pressure using a high-frequency amplitude-asymmetric strong electric field," *International Journal of Mass Spectrometry and Ion Processes*, vol. 128, no. 3, pp. 143–148, 1993.

[38] G. A. Eiceman and Z. Karpas, *Ion mobility spectrometry*. CRC press, 2005.

[39] A. A. Shvartsburg, *Differential ion mobility spectrometry: nonlinear ion transport and fundamentals of FAIMS*. CRC Press, 2008.

[40] L. Deng, Y. M. Ibrahim, A. M. Hamid, S. V. Garimella, I. K. Webb, X. Zheng, S. A. Prost, J. A. Sandoval, R. V. Norheim, G. A. Anderson, *et al.*, "Ultra-high resolution ion mobility separations utilizing traveling waves in a 13 m serpentine path length structures for lossless ion manipulations module," *Analytical chemistry*, vol. 88, no. 18, pp. 8957–8964, 2016.

[41] L. Deng, Y. M. Ibrahim, E. S. Baker, N. A. Aly, A. M. Hamid, X. Zhang, X. Zheng, S. V. Garimella, I. K. Webb, S. A. Prost, *et al.*, "Ion mobility separations of isomers based upon long path length structures for lossless ion manipulations combined with mass spectrometry," *ChemistrySelect*, vol. 1, no. 10, pp. 2396–2399, 2016.

[42] C. P. Harrilal, V. D. Gandhi, G. Nagy, X. Chen, M. G. Buchanan, R. Wojcik, C. R. Conant, M. T. Donor, Y. M. Ibrahim, S. V. Garimella, *et al.*, "Measurement and theory of gas-phase ion mobility shifts resulting from isotopomer mass distribution changes," *Analytical Chemistry*, vol. 93, no. 45, pp. 14 966–14 975, 2021.

[43] S. J. Allen and M. F. Bush, "Radio-frequency (rf) confinement in ion mobility spectrometry: Apparent mobilities and effective temperatures," *Journal of The American Society for Mass Spectrometry*, vol. 27, no. 12, pp. 2054–2063, 2016.

[44] H. Darcy, *Les fontaines publiques de la ville de Dijon: exposition et application...* Victor Dalmont, 1856.

[45] J. F. de la Mora, L. De Juan, T. Eichler, and J. Rosell, "Differential mobility analysis of molecular ions and nanometer particles," *TrAC Trends in Analytical Chemistry*, vol. 17, no. 6, pp. 328–339, 1998.

[46] E. Knutson and K. Whitby, "Aerosol classification by electric mobility: Apparatus, theory, and applications," *Journal of Aerosol Science*, vol. 6, no. 6, pp. 443–451, 1975.

[47] P. H. McMurry, "The history of condensation nucleus counters," *Aerosol Science & Technology*, vol. 33, no. 4, pp. 297–322, 2000.

[48] S. C. Wang and R. C. Flagan, "Scanning electrical mobility spectrometer," *Aerosol Science and Technology*, vol. 13, no. 2, pp. 230–240, 1990.

[49] S. C. Wang and R. C. Flagan, "Scanning electrical mobility spectrometer," *Journal of Aerosol Science*, vol. 20, no. 8, pp. 1485–1488, 1989.

[50] M. R. Stolzenburg and P. H. McMurry, "Equations governing single and tandem dma configurations and a new lognormal approximation to the transfer function," *Aerosol Science and Technology*, vol. 42, no. 6, pp. 421–432, 2008.

[51] C. Hagwood, Y. Sivathanu, and G. Mulholland, "The dma transfer function with brownian motion a trajectory/monte-carlo approach 4," *Aerosol Science and Technology*, vol. 30, no. 1, p. 1, 1999.

[52] H. Revercomb and E. A. Mason, "Theory of plasma chromatography/gaseous electrophoresis. review," *Analytical chemistry*, vol. 47, no. 7, pp. 970–983, 1975.

[53] E. A. Mason and E. W. McDaniel, *Transport properties of ions in gases*. Wiley Online Library, 1988, vol. 26.

[54] S. L. Koeniger, S. I. Merenbloom, S. J. Valentine, M. F. Jarrold, H. R. Udseth, R. D. Smith, and D. E. Clemmer, "An ims- ims analogue of ms- ms," *Analytical chemistry*, vol. 78, no. 12, pp. 4161–4174, 2006.

[55] A. T. Kirk, M. Allers, P. Cochems, J. Langejuergen, and S. Zimmermann, "A compact high resolution ion mobility spectrometer for fast trace gas analysis," *Analyst*, vol. 138, no. 18, pp. 5200–5207, 2013.

[56] W. Mui, D. A. Thomas, A. J. Downard, J. L. Beauchamp, J. H. Seinfeld, and R. C. Flagan, "Ion mobility-mass spectrometry with a radial opposed migration ion and aerosol classifier (romiac)," *Analytical chemistry*, vol. 85, no. 13, pp. 6319–6326, 2013.

[57] D. R. Oberreit, P. H. McMurry, and C. J. Hogan Jr, "Mobility analysis of 2 nm to 11 nm aerosol particles with an aspirating drift tube ion mobility spectrometer," *Aerosol Science and Technology*, vol. 48, no. 1, pp. 108–118, 2014.

[58] D. R. Oberreit, P. H. McMurry, and C. J. Hogan, "Analysis of heterogeneous uptake by nanoparticles via differential mobility analysis–drift tube ion mobility spectrometry," *Physical Chemistry Chemical Physics*, vol. 16, no. 15, pp. 6968–6979, 2014.

[59] P. Kulkarni and J. Wang, "New fast integrated mobility spectrometer for real-time measurement of aerosol size distribution: Ii. design, calibration, and performance characterization," *Journal of aerosol science*, vol. 37, no. 10, pp. 1326–1339, 2006.

[60] P. Kulkarni and J. Wang, "New fast integrated mobility spectrometer for real-time measurement of aerosol size distribution—i: Concept and theory," *Journal of aerosol science*, vol. 37, no. 10, pp. 1303–1325, 2006.

[61] F. Fernandez-Lima, D. Kaplan, and M. Park, "Note: Integration of trapped ion mobility spectrometry with mass spectrometry," *Review of Scientific Instruments*, vol. 82, no. 12, p. 126 106, 2011.

[62] D. R. Hernandez, J. D. DeBord, M. E. Ridgeway, D. A. Kaplan, M. A. Park, and F. Fernandez-Lima, "Ion dynamics in a trapped ion mobility spectrometer," *Analyst*, vol. 139, no. 8, pp. 1913–1921, 2014.

[63] J. Zeleny, "Vi. on the ratio of the velocities of the two ions produced in gases by röntgen radiation; and on some related phenomena," *The London, Edinburgh, and Dublin Philosophical Magazine and Journal of Science*, vol. 46, no. 278, pp. 120–154, 1898.

[64] K. Michelmann, J. A. Silveira, M. E. Ridgeway, and M. A. Park, "Fundamentals of trapped ion mobility spectrometry," *Journal of the American Society for Mass Spectrometry*, vol. 26, no. 1, pp. 14–24, 2014.

[65] R. C. Flagan, "On differential mobility analyzer resolution," *Aerosol Science & Technology*, vol. 30, no. 6, pp. 556–570, 1999.

[66] J. Santos, E. Hontanon, E. Ramiro, and M. Alonso, "Performance evaluation of a high-resolution parallel-plate differential mobility analyzer," *Atmospheric Chemistry and Physics*, vol. 9, no. 7, pp. 2419–2429, 2009.

[67] S. J. Valentine, R. T. Kurulugama, B. C. Bohrer, S. I. Merenbloom, R. A. Sowell, Y. Mechref, and D. E. Clemmer, "Developing ims–ims–ms for rapid characterization of abundant proteins in human plasma," *International Journal of Mass Spectrometry*, vol. 283, no. 1-3, pp. 149–160, 2009.

[68] R. T. Kurulugama, F. M. Nachtigall, S. Lee, S. J. Valentine, and D. E. Clemmer, "Overtone mobility spectrometry: Part 1. experimental observations," *Journal of the American Society for Mass Spectrometry*, vol. 20, no. 5, pp. 729–737, 2009.

[69] S. J. Valentine, S. T. Stokes, R. T. Kurulugama, F. M. Nachtigall, and D. E. Clemmer, "Overtone mobility spectrometry: Part 2. theoretical considerations of resolving power," *Journal of the American Society for Mass Spectrometry*, vol. 20, no. 5, pp. 738–750, 2011.

[70] P. Benigni and F. Fernandez-Lima, "Oversampling selective accumulation trapped ion mobility spectrometry coupled to ft-icr ms: Fundamentals and applications," *Analytical chemistry*, vol. 88, no. 14, pp. 7404–7412, 2016.

[71] H. Ounis, G. Ahmadi, and J. B. McLaughlin, "Brownian diffusion of submicrometer particles in the viscous sublayer," *Journal of Colloid and Interface Science*, vol. 143, no. 1, pp. 266–277, 1991.

[72] C. Davies, "Definitive equations for the fluid resistance of spheres," *Proceedings of the Physical Society*, vol. 57, no. 4, p. 259, 1945.

[73] D. L. Albritton, T. Miller, D. Martin, and E. McDaniel, "Mobilities of mass-identified h 3+ and h+ ions in hydrogen," *Physical Review*, vol. 171, no. 1, p. 94, 1968.

[74] D. P. Smith, T. W. Knapman, I. Campuzano, R. W. Malham, J. T. Berryman, S. E. Radford, and A. E. Ashcroft, "Deciphering drift time measurements from travelling wave ion mobility spectrometry-mass spectrometry studies," *European journal of mass spectrometry*, vol. 15, no. 2, pp. 113–130, 2009.

[75] B. M. Kolakowski and Z. Mester, "Review of applications of high-field asymmetric waveform ion mobility spectrometry (faims) and differential mobility spectrometry (dms)," *Analyst*, vol. 132, no. 9, pp. 842–864, 2007.

[76] E. Krylov, E. Nazarov, and R. Miller, "Differential mobility spectrometer: Model of operation," *International Journal of Mass Spectrometry*, vol. 266, no. 1-3, pp. 76–85, 2007.

[77] R. C. Flagan, "Opposed migration aerosol classifier (omac)," *Aerosol Science and Technology*, vol. 38, no. 9, pp. 890–899, 2004.

[78] I. K. Webb, S. V. Garimella, A. V. Tolmachev, T.-C. Chen, X. Zhang, J. T. Cox, R. V. Norheim, S. A. Prost, B. LaMarche, G. A. Anderson, *et al.*, "Mobility-resolved ion selection in uniform drift field ion mobility spectrometry/mass spectrometry: Dynamic switching in structures for lossless ion manipulations," *Analytical chemistry*, vol. 86, no. 19, pp. 9632–9637, 2014.

[79] A. Arffman, P. Juuti, J. Harra, and J. Keskinen, "Differential diffusion analyzer," *Aerosol Science and Technology*, vol. 51, no. 12, pp. 1429–1437, 2017.

[80] F. Fernandez-Lima, D. A. Kaplan, J. Suetering, and M. A. Park, "Gas-phase separation using a trapped ion mobility spectrometer," *International Journal for Ion Mobility Spectrometry*, vol. 14, no. 2, pp. 93–98, 2011.

[81] M. E. Ridgeway, M. Lubeck, J. Jordens, M. Mann, and M. A. Park, "Trapped ion mobility spectrometry: A short review," *International Journal of Mass Spectrometry*, vol. 425, pp. 22–35, 2018.

[82] W. Sutherland, "Lxxv. a dynamical theory of diffusion for non-electrolytes and the molecular mass of albumin," *The London, Edinburgh, and Dublin Philosophical Magazine and Journal of Science*, vol. 9, no. 54, pp. 781–785, 1905.

[83] L. Deng, I. K. Webb, S. V. Garimella, A. M. Hamid, X. Zheng, R. V. Norheim, S. A. Prost, G. A. Anderson, J. A. Sandoval, E. S. Baker, *et al.*, "Serpentine ultralong path with extended routing (super) high resolution traveling wave ion mobility-ms using structures for lossless ion manipulations," *Analytical chemistry*, vol. 89, no. 8, pp. 4628–4634, 2017.

[84] Z. Huang and C. F. Ivory, "Digitally controlled electrophoretic focusing," *Analytical chemistry*, vol. 71, no. 8, pp. 1628–1632, 1999.

[85] J. A. Silveira, K. Michelmann, M. E. Ridgeway, and M. A. Park, "Fundamentals of trapped ion mobility spectrometry part ii: Fluid dynamics," *Journal of the American Society for Mass Spectrometry*, vol. 27, no. 4, pp. 585–595, 2016.

[86] L. V. Tose, P. Benigni, D. Leyva, A. Sundberg, C. E. Ramírez, M. E. Ridgeway, M. A. Park, W. Romão, R. Jaffé, and F. Fernandez-Lima, "Coupling trapped ion mobility spectrometry to mass spectrometry: Trapped ion mobility spectrometry–time-of-flight mass spectrometry versus trapped ion mobility spectrometry–fourier transform ion cyclotron resonance mass spectrometry," *Rapid Communications in Mass Spectrometry*, vol. 32, no. 15, pp. 1287–1295, 2018.

[87] P. Benigni, J. Porter, M. E. Ridgeway, M. A. Park, and F. Fernandez-Lima, "Increasing analytical separation and duty cycle with nonlinear analytical mobility scan functions in tims-ft-icr ms," *Analytical chemistry*, vol. 90, no. 4, pp. 2446–2450, 2018.

[88] C. Bleiholder, "Towards measuring ion mobilities in non-stationary gases and non-uniform and dynamic electric fields (i). transport equation," *International Journal of Mass Spectrometry*, vol. 399, pp. 1–9, 2016.

[89] W. Paul, "Electromagnetic traps for charged and neutral particles," *Reviews of modern physics*, vol. 62, no. 3, p. 531, 1990.

[90] P. E. Miller and M. B. Denton, "The quadrupole mass filter: Basic operating concepts," *Journal of chemical education*, vol. 63, no. 7, p. 617, 1986.

[91] M. Nasse and C. Foot, "Influence of background pressure on the stability region of a paul trap," *European Journal of Physics*, vol. 22, no. 6, p. 563, 2001.

[92] L. A. Viehland and D. E. Goeringer, "Kinetic theory of radio frequency quadrupole ion traps. i. trapping of atomic ions in a pure atomic gas," *The Journal of chemical physics*, vol. 120, no. 19, pp. 9090–9103, 2004.

[93] K. J. Adams, D. Montero, D. Aga, and F. Fernandez-Lima, "Isomer separation of poly-brominated diphenyl ether metabolites using nanoesi-tims-ms," *International journal for ion mobility spectrometry*, vol. 19, no. 2, pp. 69–76, 2016.

[94] X. Chen, V. Gandhi, J. Coots, Y. Fan, L. Xu, N. Fukushima, and C. Larriba-Andaluz, "High resolution varying field drift tube ion mobility spectrometer with diffusion autocorrection," *Journal of Aerosol Science*, vol. 140, p. 105 485, 2020.

[95] R. Cumeras, E. Figueras, C. E. Davis, J. I. Baumbach, and I. Gracia, "Review on ion mobility spectrometry. part 1: Current instrumentation," *Analyst*, vol. 140, no. 5, pp. 1376–1390, 2015.

[96] P. H. McMurry, "A review of atmospheric aerosol measurements," *Atmospheric Environment*, vol. 34, no. 12-14, pp. 1959–1999, 2000.

[97] M. Amo-González and S. Pérez, "Planar differential mobility analyzer with a resolving power of 110," *Analytical chemistry*, vol. 90, no. 11, pp. 6735–6741, 2018.

[98] A. J. Downard, J. F. Dama, and R. C. Flagan, "An asymptotic analysis of differential electrical mobility classifiers," *Aerosol Science and Technology*, vol. 45, no. 6, pp. 727–739, 2011.

[99] A. Franchin, A. Downard, J. Kangasluoma, T. Nieminen, K. Lehtipalo, G. Steiner, H. E. Manninen, T. Petäjä, R. C. Flagan, and M. Kulmala, "A new high-transmission inlet for the caltech nano-rdma for size distribution measurements of sub-3 nm ions at ambient concentrations," *Atmospheric Measurement Techniques*, vol. 9, no. 6, pp. 2709–2720, 2016.

[100] B. H. Clowers, W. F. Siems, H. H. Hill, and S. M. Massick, "Hadamard transform ion mobility spectrometry," *Analytical chemistry*, vol. 78, no. 1, pp. 44–51, 2006.

[101] A. W. Szumlas, S. J. Ray, and G. M. Hieftje, "Hadamard transform ion mobility spectrometry," *Analytical Chemistry*, vol. 78, no. 13, pp. 4474–4481, 2006.

[102] G. Eiceman, Z. Karpas, and H. Hill, "Detection of explosives by ims," *Ion mobility spectrometry, 3rd edn. CRC Press, Boca Raton*, pp. 269–285, 2014.

[103] G. Eiceman and J. Stone, *Peer reviewed: Ion mobility spectrometers in national defense*, 2004.

[104] W. F. Siems, C. Wu, E. E. Tarver, H. H. J. Hill, P. R. Larsen, and D. G. McMinn, "Measuring the resolving power of ion mobility spectrometers," *Analytical Chemistry*, vol. 66, no. 23, pp. 4195–4201, 1994.

[105] C. Wu, W. E. Steiner, P. S. Tornatore, L. M. Matz, W. F. Siems, D. A. Atkinson, and H. H. Hill Jr, "Construction and characterization of a high-flow, high-resolution ion mobility spectrometer for detection of explosives after personnel portal sampling," *Talanta*, vol. 57, no. 1, pp. 123–134, 2002.

[106] A. Hollerbach, Z. Baird, and R. G. Cooks, "Ion separation in air using a three-dimensional printed ion mobility spectrometer," *Analytical chemistry*, vol. 89, no. 9, pp. 5058–5065, 2017.

[107] A. Hollerbach, P. W. Fedick, and R. G. Cooks, "Ion mobility–mass spectrometry using a dual-gated 3d printed ion mobility spectrometer," *Analytical chemistry*, vol. 90, no. 22, pp. 13 265–13 272, 2018.

[108] S. V. Garimella, Y. M. Ibrahim, I. K. Webb, A. B. Ipsen, T.-C. Chen, A. V. Tolmachev, E. S. Baker, G. A. Anderson, and R. D. Smith, "Ion manipulations in structures for lossless ion manipulations (slim): Computational evaluation of a 90 turn and a switch," *Analyst*, vol. 140, no. 20, pp. 6845–6852, 2015.

[109] R. Wojcik, G. Nagy, I. K. Attah, I. K. Webb, S. V. Garimella, K. K. Weitz, A. Hollerbach, M. E. Monroe, M. R. Ligare, F. F. Nielson, *et al.*, "Slim ultrahigh resolution ion mobility spectrometry separations of isotopologues and isotopomers reveal mobility shifts due to mass distribution changes," *Analytical chemistry*, vol. 91, no. 18, pp. 11 952–11 962, 2019.

[110] I. G. Loscertales, "Drift differential mobility analyzer," *Journal of aerosol science*, vol. 29, no. 9, pp. 1117–1139, 1998.

[111] Y. Du, W. Wang, and H. Li, "Resolution enhancement of ion mobility spectrometry by improving the three-zone properties of the bradbury-nielsen gate," *Analytical chemistry*, vol. 84, no. 3, pp. 1725–1731, 2012.

[112] C. Chen, H. Chen, D. Jiang, M. Li, W. Huang, and H. Li, "Enhancing the sensitivity of ion mobility spectrometry using the ion enrichment effect of non-uniform electrostatic field," *Sensors and Actuators B: Chemical*, vol. 295, pp. 179–185, 2019.

[113] B. C. Bohrer, S. I. Merenbloom, S. L. Koeniger, A. E. Hilderbrand, and D. E. Clemmer, "Biomolecule analysis by ion mobility spectrometry," *Annu. Rev. Anal. Chem.*, vol. 1, pp. 293–327, 2008.

[114] A. B. Kanu, P. Dwivedi, M. Tam, L. Matz, and H. H. Hill Jr, "Ion mobility–mass spectrometry," *Journal of mass spectrometry*, vol. 43, no. 1, pp. 1–22, 2008.

[115] S. C. Henderson, S. J. Valentine, A. E. Counterman, and D. E. Clemmer, "Esi/ion trap/ion mobility/time-of-flight mass spectrometry for rapid and sensitive analysis of biomolecular mixtures," *Analytical chemistry*, vol. 71, no. 2, pp. 291–301, 1999.

[116] K. Kaplan, S. Graf, C. Tanner, M. Gonin, K. Fuhrer, R. Knochenmuss, P. Dwivedi, and H. H. Hill Jr, "Resistive glass im-tofms," *Analytical chemistry*, vol. 82, no. 22, pp. 9336–9343, 2010.

[117] M. Kwasnik, K. Fuhrer, M. Gonin, K. Barbeau, and F. M. Fernandez, "Performance, resolving power, and radial ion distributions of a prototype nanoelectrospray ionization resistive glass atmospheric pressure ion mobility spectrometer," *Analytical chemistry*, vol. 79, no. 20, pp. 7782–7791, 2007.

[118] M. Kwasnik and F. M. Fernández, "Theoretical and experimental study of the achievable separation power in resistive-glass atmospheric pressure ion mobility spectrometry," *Rapid Communications in Mass Spectrometry*, vol. 24, no. 13, pp. 1911–1918, 2010.

[119] B. L. Smith, C. Boisdon, I. S. Young, T. Praneenararat, T. Vilaivan, and S. Maher, "Flexible drift tube for high resolution ion mobility spectrometry (flex-dt-ims)," *Analytical chemistry*, vol. 92, no. 13, pp. 9104–9112, 2020.

[120] M. Khalesi, M. Sheikh-Zeinoddin, and M. Tabrizchi, "Determination of ochratoxin a in licorice root using inverse ion mobility spectrometry," *Talanta*, vol. 83, no. 3, pp. 988–993, 2011.

[121] M. Latif, D. Zhang, and G. Gamez, "Flowing atmospheric-pressure afterglow drift tube ion mobility spectrometry," *Analytica Chimica Acta*, vol. 1163, p. 338507, 2021.

[122] R. S. Glaskin, S. J. Valentine, and D. E. Clemmer, "A scanning frequency mode for ion cyclotron mobility spectrometry," *Analytical chemistry*, vol. 82, no. 19, pp. 8266–8271, 2010.

[123] X. Chen, S. A. Raab, T. Poe, D. E. Clemmer, and C. Larriba-Andaluz, "Determination of gas-phase ion structures of locally polar homopolymers through high-resolution ion mobility spectrometry–mass spectrometry," *Journal of The American Society for Mass Spectrometry*, vol. 30, no. 6, pp. 905–918, 2019.

[124] C. K. Ober, "Shape persistence of synthetic polymers," *Science*, vol. 288, no. 5465, pp. 448–449, 2000.

[125] J. M. Frechet, "Functional polymers and dendrimers: Reactivity, molecular architecture, and interfacial energy," *Science*, vol. 263, no. 5154, pp. 1710–1715, 1994.

[126] S. R. Forrest, "The path to ubiquitous and low-cost organic electronic appliances on plastic," *nature*, vol. 428, no. 6986, pp. 911–918, 2004.

[127] J. Wang, L. Tian, A. Argenti, and K. E. Uhrich, "Nanoscale amphiphilic star-like macro-molecules with carboxy-, methoxy and amine-terminated chain ends," *Journal of bioactive and compatible polymers*, vol. 21, no. 4, pp. 297–313, 2006.

[128] K. E. Uhrich, S. M. Cannizzaro, R. S. Langer, and K. M. Shakesheff, "Polymeric systems for controlled drug release," *Chemical Reviews-Columbus*, vol. 99, no. 11, pp. 3181–3198, 1999.

[129] T. Aida, E. Meijer, and S. Stupp, "Functional supramolecular polymers," *Science*, vol. 335, no. 6070, pp. 813–817, 2012.

[130] S. I. Stupp, V. LeBonheur, K. Walker, L.-S. Li, K. E. Huggins, M. Keser, and A. Amstutz, "Supramolecular materials: Self-organized nanostructures," *Science*, vol. 276, no. 5311, pp. 384–389, 1997.

[131] B. H. Robinson, "E-waste: An assessment of global production and environmental impacts," *Science of the total environment*, vol. 408, no. 2, pp. 183–191, 2009.

[132] J. N. Onuchic, Z. Luthey-Schulten, and P. G. Wolynes, "Theory of protein folding: The energy landscape perspective," *Annual review of physical chemistry*, vol. 48, no. 1, pp. 545–600, 1997.

[133] C. J. Hawker and K. L. Wooley, "The convergence of synthetic organic and polymer chemistries," *Science*, vol. 309, no. 5738, pp. 1200–1205, 2005.

[134] E. R. Kay, D. A. Leigh, and F. Zerbetto, "Synthetic molecular motors and mechanical machines," *Angewandte Chemie International Edition*, vol. 46, no. 1-2, pp. 72–191, 2007.

[135] P. Samorì, "Scanning probe microscopies beyond imaging," *Journal of Materials Chemistry*, vol. 14, no. 9, pp. 1353–1366, 2004.

[136] S. Mann, "Self-assembly and transformation of hybrid nano-objects and nanostructures under equilibrium and non-equilibrium conditions," *Nature materials*, vol. 8, no. 10, pp. 781–792, 2009.

[137] D. H. Howe, J. L. Hart, R. M. McDaniel, M. L. Taheri, and A. J. Magenau, "Functionalization-induced self-assembly of block copolymers for nanoparticle synthesis," *ACS Macro Letters*, vol. 7, no. 12, pp. 1503–1508, 2018.

[138] J. Rodriguez-Hernandez, F. Chécot, Y. Gnanou, and S. Lecommandoux, "Toward 'smart'nano-objects by self-assembly of block copolymers in solution," *Progress in polymer science*, vol. 30, no. 7, pp. 691–724, 2005.

[139] H. Hofmann, A. Soranno, A. Borgia, K. Gast, D. Nettels, and B. Schuler, "Polymer scaling laws of unfolded and intrinsically disordered proteins quantified with single-molecule spectroscopy," *Proceedings of the National Academy of Sciences*, vol. 109, no. 40, pp. 16 155–16 160, 2012.

[140] A. Janshoff, M. Neitzert, Y. Oberdörfer, and H. Fuchs, "Force spectroscopy of molecular systems—single molecule spectroscopy of polymers and biomolecules," *Angewandte Chemie International Edition*, vol. 39, no. 18, pp. 3212–3237, 2000.

[141] S. R. Quake, H. Babcock, and S. Chu, "The dynamics of partially extended single molecules of dna," *Nature*, vol. 388, no. 6638, pp. 151–154, 1997.

[142] M. D. Wang, H. Yin, R. Landick, J. Gelles, and S. M. Block, "Stretching dna with optical tweezers," *Biophysical journal*, vol. 72, no. 3, pp. 1335–1346, 1997.

[143] J. B. Fenn, M. Mann, C. K. Meng, S. F. Wong, and C. M. Whitehouse, "Electrospray ionization for mass spectrometry of large biomolecules," *Science*, vol. 246, no. 4926, pp. 64–71, 1989.

[144] K. Tanaka, H. Waki, Y. Ido, S. Akita, Y. Yoshida, T. Yoshida, and T. Matsuo, "Protein and polymer analyses up to m/z 100 000 by laser ionization time-of-flight mass spectrometry," *Rapid communications in mass spectrometry*, vol. 2, no. 8, pp. 151–153, 1988.

[145] C. E. Costello, "Time, life… and mass spectrometry new techniques to address biological questions," *Biophysical chemistry*, vol. 68, no. 1-3, pp. 173–188, 1997.

[146] D. E. Clemmer and M. F. Jarrold, "Ion mobility measurements and their applications to clusters and biomolecules," *Journal of mass spectrometry*, vol. 32, no. 6, pp. 577–592, 1997.

[147] S. Armenta, M. Alcala, and M. Blanco, "A review of recent, unconventional applications of ion mobility spectrometry (ims)," *Analytica chimica acta*, vol. 703, no. 2, pp. 114–123, 2011.

[148] T. Nohmi and J. B. Fenn, "Electrospray mass spectrometry of poly (ethylene glycols) with molecular weights up to five million," *Journal of the American Chemical Society*, vol. 114, no. 9, pp. 3241–3246, 1992.

[149] J. B. Fenn, "Electrospray wings for molecular elephants (nobel lecture)," *Angewandte Chemie International Edition*, vol. 42, no. 33, pp. 3871–3894, 2003.

[150] J. B. Fenn, J. Rosell, and C. K. Meng, "In electrospray ionization, how much pull does an ion need to escape its droplet prison?" *Journal of the American Society for Mass Spectrometry*, vol. 8, no. 11, pp. 1147–1157, 1997.

[151] S. Wong, C. Meng, and J. Fenn, "Multiple charging in electrospray ionization of poly (ethylene glycols)," *The Journal of Physical Chemistry*, vol. 92, no. 2, pp. 546–550, 1988.

[152] G. Von Helden, T. Wyttenbach, and M. T. Bowers, "Conformation of macromolecules in the gas phase: Use of matrix-assisted laser desorption methods in ion chromatography," *Science*, vol. 267, no. 5203, pp. 1483–1485, 1995.

[153] T. Wyttenbach, G. von Helden, and M. T. Bowers, "Conformations of alkali ion cationized polyethers in the gas phase: Polyethylene glycol and bis [(benzo-15-crown-5)-15-ylmethyl] pimelate," *International journal of mass spectrometry and ion processes*, vol. 165, pp. 377–390, 1997.

[154] G. von Helden, T. Wyttenbach, and M. T. Bowers, "Inclusion of a maldi ion source in the ion chromatography technique: Conformational information on polymer and biomolecular ions," *International journal of mass spectrometry and ion processes*, vol. 146, pp. 349–364, 1995.

[155] J. Gidden, T. Wyttenbach, A. T. Jackson, J. H. Scrivens, and M. T. Bowers, "Gas-phase conformations of synthetic polymers: Poly (ethylene glycol), poly (propylene glycol), and poly (tetramethylene glycol)," *Journal of the American Chemical Society*, vol. 122, no. 19, pp. 4692–4699, 2000.

[156] S. Ude, J. Fernández De La Mora, and B. Thomson, "Charge-induced unfolding of multiply charged polyethylene glycol ions," *Journal of the American Chemical Society*, vol. 126, no. 38, pp. 12 184–12 190, 2004.

[157] S. Trimpin and D. E. Clemmer, "Ion mobility spectrometry/mass spectrometry snapshots for assessing the molecular compositions of complex polymeric systems," *Analytical chemistry*, vol. 80, no. 23, pp. 9073–9083, 2008.

[158] S. Trimpin, M. Plasencia, D. Isailovic, and D. E. Clemmer, "Resolving oligomers from fully grown polymers with ims- ms," *Analytical chemistry*, vol. 79, no. 21, pp. 7965–7974, 2007.

[159] C. Larriba and J. Fernandez de la Mora, "The gas phase structure of coulombically stretched polyethylene glycol ions," *The Journal of Physical Chemistry B*, vol. 116, no. 1, pp. 593–598, 2012.

[160] C. Larriba, "Production of ions and particles via simple and compound electrosprays in vacuum, gases or liquids (polar and non-polar)," Ph.D. dissertation, Ph. D. Dissertation, Yale University, New Haven, CT, 2010. Google Scholar …, 2010.

[161] J. Iribarne and B. Thomson, "On the evaporation of small ions from charged droplets," *The Journal of chemical physics*, vol. 64, no. 6, pp. 2287–2294, 1976.

[162] M. Dole, L. L. Mack, R. L. Hines, R. C. Mobley, L. D. Ferguson, and M. B. Alice, "Molecular beams of macroions," *The Journal of chemical physics*, vol. 49, no. 5, pp. 2240–2249, 1968.

[163] C. J. Hogan Jr and J. F. De La Mora, "Tandem ion mobility-mass spectrometry (ims-ms) study of ion evaporation from ionic liquid-acetonitrile nanodrops," *Physical Chemistry Chemical Physics*, vol. 11, no. 36, pp. 8079–8090, 2009.

[164] E. Ahadi and L. Konermann, "Modeling the behavior of coarse-grained polymer chains in charged water droplets: Implications for the mechanism of electrospray ionization," *The Journal of Physical Chemistry B*, vol. 116, no. 1, pp. 104–112, 2012.

[165] L. Konermann, E. Ahadi, A. D. Rodriguez, and S. Vahidi, *Unraveling the mechanism of electrospray ionization*, 2013.

[166] Q. Duez, H. Metwally, and L. Konermann, "Electrospray ionization of polypropylene glycol: Rayleigh-charged droplets, competing pathways, and charge state-dependent conformations," *Analytical chemistry*, vol. 90, no. 16, pp. 9912–9920, 2018.

[167] J. K. Chung and S. Consta, "Release mechanisms of poly (ethylene glycol) macroions from aqueous charged nanodroplets," *The Journal of Physical Chemistry B*, vol. 116, no. 19, pp. 5777–5785, 2012.

[168] S. Consta and J. K. Chung, "Charge-induced conformational changes of peg-(na+) n in a vacuum and aqueous nanodroplets," *The Journal of Physical Chemistry B*, vol. 115, no. 35, pp. 10 447–10 455, 2011.

[169] S. Consta and A. Malevanets, "Manifestations of charge induced instability in droplets effected by charged macromolecules," *Physical Review Letters*, vol. 109, no. 14, p. 148 301, 2012.

[170] S. Consta and A. Malevanets, "Classification of the ejection mechanisms of charged macromolecules from liquid droplets," *The Journal of Chemical Physics*, vol. 138, no. 4, p. 044 314, 2013.

[171] C. Larriba, J. F. De La Mora, and D. E. Clemmer, "Electrospray ionization mechanisms for large polyethylene glycol chains studied through tandem ion mobility spectrometry," *Journal of the American Society for Mass Spectrometry*, vol. 25, no. 8, pp. 1332–1345, 2014.

[172] J. R. Haler, D. Morsa, P. Lecomte, C. Jérôme, J. Far, and E. De Pauw, "Predicting ion mobility-mass spectrometry trends of polymers using the concept of apparent densities," *Methods*, vol. 144, pp. 125–133, 2018.

[173] J. R. Haler, P. Massonnet, F. Chirot, C. Kune, C. Comby-Zerbino, J. Jordens, M. Honing, Y. Mengerink, J. Far, P. Dugourd, *et al.*, "Comparison of different ion mobility setups using poly (ethylene oxide) peo polymers: Drift tube, tims, and t-wave," *Journal of The American Society for Mass Spectrometry*, vol. 29, no. 1, pp. 114–120, 2017.

[174] J. R. Haler, J. Far, A. Aqil, J. Claereboudt, N. Tomczyk, K. Giles, C. Jérôme, and E. De Pauw, "Multiple gas-phase conformations of a synthetic linear poly (acrylamide) polymer observed using ion mobility-mass spectrometry," *Journal of the American Society for Mass Spectrometry*, vol. 28, no. 11, pp. 2492–2499, 2017.

[175] J. F. de la Mora, "Why do groel ions exhibit two gas phase conformers?" *Journal of the American Society for Mass Spectrometry*, vol. 23, no. 12, pp. 2115–2121, 2012.

[176] P. W. Devine, H. C. Fisher, A. N. Calabrese, F. Whelan, D. R. Higazi, J. R. Potts, D. C. Lowe, S. E. Radford, and A. E. Ashcroft, "Investigating the structural compaction of biomolecules upon transition to the gas-phase using esi-twims-ms," *Journal of the American Society for Mass Spectrometry*, vol. 28, no. 9, pp. 1855–1862, 2017.

[177] E. R. Dickinson, E. Jurneczko, K. J. Pacholarz, D. J. Clarke, M. Reeves, K. L. Ball, T. Hupp, D. Campopiano, P. V. Nikolova, and P. E. Barran, "Insights into the conformations of three structurally diverse proteins: Cytochrome c, p53, and mdm2, provided by variable-temperature ion mobility mass spectrometry," *Analytical chemistry*, vol. 87, no. 6, pp. 3231–3238, 2015.

[178] Z. Hall, A. Politis, M. F. Bush, L. J. Smith, and C. V. Robinson, "Charge-state dependent compaction and dissociation of protein complexes: Insights from ion mobility and molecular dynamics," *Journal of the American Chemical Society*, vol. 134, no. 7, pp. 3429–3438, 2012.

[179] J. R. Jhingree, B. Bellina, K. J. Pacholarz, and P. E. Barran, "Charge mediated compaction and rearrangement of gas-phase proteins: A case study considering two proteins at opposing ends of the structure-disorder continuum," *Journal of The American Society for Mass Spectrometry*, vol. 28, no. 7, pp. 1450–1461, 2017.

[180] I. Michaelevski, M. Eisenstein, and M. Sharon, "Gas-phase compaction and unfolding of protein structures," *Analytical chemistry*, vol. 82, no. 22, pp. 9484–9491, 2010.

[181] M. Porrini, F. Rosu, C. Rabin, L. Darré, H. Gómez, M. Orozco, and V. Gabelica, "Compaction of duplex nucleic acids upon native electrospray mass spectrometry," *ACS central science*, vol. 3, no. 5, pp. 454–461, 2017.

[182] T. G. Flick, S. I. Merenbloom, and E. R. Williams, "Effects of metal ion adduction on the gas-phase conformations of protein ions," *Journal of the American Society for Mass Spectrometry*, vol. 24, no. 11, pp. 1654–1662, 2013.

[183] K. J. Pacholarz, S. J. Peters, R. A. Garlish, A. J. Henry, R. J. Taylor, D. P. Humphreys, and P. E. Barran, "Molecular insights into the thermal stability of mabs with variable-temperature ion-mobility mass spectrometry," *ChemBioChem*, vol. 17, no. 1, pp. 46–51, 2016.

[184] K. J. Pacholarz, M. Porrini, R. A. Garlish, R. J. Burnley, R. J. Taylor, A. J. Henry, and P. E. Barran, "Dynamics of intact immunoglobulin g explored by drift-tube ion-mobility mass spectrometry and molecular modeling," *Angewandte Chemie International Edition*, vol. 53, no. 30, pp. 7765–7769, 2014.

[185] C. Larriba, C. J. Hogan Jr, M. Attoui, R. Borrajo, J. F. Garcia, and J. F. De La Mora, "The mobility–volume relationship below 3.0 nm examined by tandem mobility–mass measurement," *Aerosol Science and Technology*, vol. 45, no. 4, pp. 453–467, 2011.

[186] S. Ude and J. F. De La Mora, "Molecular monodisperse mobility and mass standards from electrosprays of tetra-alkyl ammonium halides," *Journal of Aerosol Science*, vol. 36, no. 10, pp. 1224–1237, 2005.

[187] C. S. Hoaglund, S. J. Valentine, C. R. Sporleder, J. P. Reilly, and D. E. Clemmer, "Three-dimensional ion mobility/tofms analysis of electrosprayed biomolecules," *Analytical chemistry*, vol. 70, no. 11, pp. 2236–2242, 1998.

[188] J. E. Mark, *Polymer data handbook*. Oxford university press, 2009.

[189] D. W. Hutmacher, T. Schantz, I. Zein, K. W. Ng, S. H. Teoh, and K. C. Tan, "Mechanical properties and cell cultural response of polycaprolactone scaffolds designed and fabricated via fused deposition modeling," *Journal of Biomedical Materials Research: An Official Journal of The Society for Biomaterials, The Japanese Society for Biomaterials, and The Australian Society for Biomaterials and the Korean Society for Biomaterials*, vol. 55, no. 2, pp. 203–216, 2001.

[190] O. K. Bates, "Thermal conductivity of liquid silicones," *Industrial & Engineering Chemistry*, vol. 41, no. 9, pp. 1966–1968, 1949.

[191] E. Criado-Hidalgo, J. Fernández-García, and J. Fernández de la Mora, "Mass and charge distribution analysis in negative electrosprays of large polyethylene glycol chains by ion mobility mass spectrometry," *Analytical chemistry*, vol. 85, no. 5, pp. 2710–2716, 2013.

[192] S. Consta, M. I. Oh, and A. Malevanets, "New mechanisms of macroion-induced disintegration of charged droplets," *Chemical Physics Letters*, vol. 663, pp. 1–12, 2016.

[193] Q. Duez, T. Josse, V. Lemaur, F. Chirot, C. M. Choi, P. Dubois, P. Dugourd, J. Cornil, P. Gerbaux, and J. De Winter, "Correlation between the shape of the ion mobility signals and the stepwise folding process of polylactide ions," *Journal of Mass Spectrometry*, vol. 52, no. 3, pp. 133–138, 2017.

[194] J. R. Haler, P. Massonnet, J. Far, V. R. de la Rosa, P. Lecomte, R. Hoogenboom, C. Jérôme, and E. De Pauw, "Gas-phase dynamics of collision induced unfolding, collision induced dissociation, and electron transfer dissociation-activated polymer ions," *Journal of The American Society for Mass Spectrometry*, vol. 30, no. 4, pp. 563–572, 2018.

[195] J. N. Hoskins, S. Trimpin, and S. M. Grayson, "Architectural differentiation of linear and cyclic polymeric isomers by ion mobility spectrometry-mass spectrometry," *Macromolecules*, vol. 44, no. 17, pp. 6915–6918, 2011.

[196] P. S. Epstein, "On the resistance experienced by spheres in their motion through gases," *Physical Review*, vol. 23, no. 6, p. 710, 1924.

[197] R. A. Millikan, "The general law of fall of a small spherical body through a gas, and its bearing upon the nature of molecular reflection from surfaces," *Physical Review*, vol. 22, no. 1, p. 1, 1923.

[198] I. D. Campuzano, C. Larriba, D. Bagal, and P. D. Schnier, "Ion mobility and mass spectrometry measurements of the humanized iggk nist monoclonal antibody," in *State-of-the-Art and Emerging Technologies for Therapeutic Monoclonal Antibody Characterization Volume 3. Defining the Next Generation of Analytical and Biophysical Techniques*, ACS Publications, 2015, pp. 75–112.

[199] V. Shrivastav, M. Nahin, C. J. Hogan, and C. Larriba-Andaluz, "Benchmark comparison for a multi-processing ion mobility calculator in the free molecular regime," *Journal of the American Society for Mass Spectrometry*, vol. 28, no. 8, pp. 1540–1551, 2017.

[200] T. Wyttenbach, G. von Helden, J. J. Batka Jr, D. Carlat, and M. T. Bowers, "Effect of the long-range potential on ion mobility measurements," *Journal of the American society for mass spectrometry*, vol. 8, no. 3, pp. 275–282, 1997.

[201] A. A. Shvartsburg and M. F. Jarrold, "An exact hard-spheres scattering model for the mobilities of polyatomic ions," *Chemical physics letters*, vol. 261, no. 1-2, pp. 86–91, 1996.

[202] M. Mesleh, J. Hunter, A. Shvartsburg, G. C. Schatz, and M. Jarrold, "Structural information from ion mobility measurements: Effects of the long-range potential," *The Journal of Physical Chemistry*, vol. 100, no. 40, pp. 16 082–16 086, 1996.

[203] J. W. S. B. Rayleigh, *The theory of sound*. Macmillan, 1896, vol. 2.

[204] M. F. Bush, Z. Hall, K. Giles, J. Hoyes, C. V. Robinson, and B. T. Ruotolo, "Collision cross sections of proteins and their complexes: A calibration framework and database for gas-phase structural biology," *Analytical chemistry*, vol. 82, no. 22, pp. 9557–9565, 2010.

[205] E. Jurneczko and P. E. Barran, "How useful is ion mobility mass spectrometry for structural biology? the relationship between protein crystal structures and their collision cross sections in the gas phase," *Analyst*, vol. 136, no. 1, pp. 20–28, 2011.

[206] B. T. Ruotolo, J. L. Benesch, A. M. Sandercock, S.-J. Hyung, and C. V. Robinson, "Ion mobility–mass spectrometry analysis of large protein complexes," *Nature protocols*, vol. 3, no. 7, pp. 1139–1152, 2008.

[207] K. Breuker and F. W. McLafferty, "Stepwise evolution of protein native structure with electrospray into the gas phase, 10- 12 to 102 s," *Proceedings of the National Academy of Sciences*, vol. 105, no. 47, pp. 18 145–18 152, 2008.

[208] M. Z. Steinberg, R. Elber, F. W. McLafferty, R. B. Gerber, and K. Breuker, "Early structural evolution of native cytochrome c after solvent removal," *ChemBioChem*, vol. 9, no. 15, pp. 2417–2423, 2008.

VITA

Xi Chen

Education

- Doctor of Philosophy, May 2022

  Purdue University

  Department of Mechanical Engineering

- Master of Science, June 2014

  Zhejiang Normal University

  Department of Physics

- Bachelor of Science, June 2011

  Changshu Institute of Technology

  Department of Physics

Publications

1. **Chen X**, Larriba-Andaluz C, et al. Enhancing Separation and Constriction of Ion Mobility Distributions in Drift Tubes at Atmospheric Pressure Using Varying Fields[J]. Analytical Chemistry, 2022,10.1021/acs.analchem.2c00467

2. Su P, **Chen X**, Smith A J, et al. Multiplexing of Electrospray Ionization Sources Using Orthogonal Injection into an Electrodynamic Ion Funnel[J]. Analytical Chemistry, 2021, 93(33): 11576-11584. (co-first author)

3. Larriba-Andaluz C, **Chen X**, Nahin M, et al. Analysis of ion motion and diffusion confinement in inverted drift tubes and trapped ion mobility spectrometry devices[J]. Analytical chemistry, 2018, 91(1): 919-927.

4. **Chen X**, Gandhi V, Coots J, et al. High resolution varying field drift tube ion mobility spectrometer with diffusion autocorrection[J]. Journal of Aerosol Science, 2020, 140: 105485.

5. **Chen X**, Raab S A, Poe T, et al. Determination of gas-phase ion structures of locally polar homopolymers through high-resolution ion mobility spectrometry–mass spectrometry[J]. Journal of The American Society for Mass Spectrometry, 2019, 30(6): 905-918.(co-first author)

6. Christopher P. Harrilal, Viraj D. Gandhi, Gabe Nagy, **Chen X**, et al. Measurement and Theory of Gas-Phase Ion Mobility Shifts Resulting from Isotopomer Mass Distribution Changes[J]. Analytical Chemistry, 2021.

7. X. Zhang, J. Gomez-Paz, **Chen X**, J. M. McDonough, M. M. Islam, Y. Andreopoulos, L. Zhu, and H. Yu, Volumetric lattice boltzmann method for wall stresses of image-based pulsatile flows, Scientific Reports, vol. 12, no. 1, pp.1–15, 2022.

8. M. Latif, **Chen X** , V. D. Gandhi, C. Larriba-Andaluz, and G. Gamez, Field- switching repeller flowing atmospheric-pressure afterglow drift tube ion mobilityspectrometry, Journal of the American Society for Mass Spectrometry, 2022.

9. Yu H, **Chen X**, Wang Z, et al. Mass-conserved volumetric lattice Boltzmann method for complex flows with willfully moving boundaries[J]. Physical Review E, 2014, 89(6): 063304.

10. Wu T, Derrick J, Nahin M, **Chen X**, et al. Optimization of long range potential interaction parameters in ion mobility spectrometry[J]. The Journal of chemical physics, 2018, 148(7): 074102.

11. Coots J, Gandhi V, Onakoya T, **Chen X**, et al. A parallelized tool to calculate the electrical mobility of charged aerosol nanoparticles and ions in the gas phase[J]. Journal of Aerosol Science, 2020, 147: 105570.

12. Yu H W, **Chen X**, Xu Y, et al. Scaling of-asymmetries in viscous flow with-symmetric inflow and outflow[J]. Journal of Physics A: Mathematical and Theoretical, 2014, 48(3): 035501.